The Pennsylvania State University

The Graduate School

EVALUATING THE PERFORMANCE CHARACTERISTICS OF VIRUS FILTRATION MEMBRANES

A Dissertation in

Chemical Engineering

by

Fatemeh Fallahianbijan

Submitted in Partial Fulfillment
of the Requirements
for the Degree of

Doctor of Philosophy

August 2019

The dissertation of Fatemeh Fallahianbijan was reviewed and approved* by the following:

Andrew L. Zydney
Distinguished Professor of Chemical Engineering
Dissertation Advisor
Chair of Committee

Darrell Velegol
Distinguished Professor of Chemical Engineering

Michael Hickner
Professor of Materials Science and Engineering

Manish Kumar
Associate Professor of Chemical Engineering

Phillip Savage
Walter L. Robb Chair and Professor of Chemical Engineering
Head of the Department of Chemical Engineering

*Signatures are on file in the Graduate School

ABSTRACT

Providing high levels of viral clearance is essential in the manufacturing of protein-based biotherapeutics derived from either mammalian cell lines or blood plasma. Virus filtration has become an important component of the downstream purification process, particularly in the production of monoclonal antibodies used for treatment of cancer and immune disorders. Virus filtration is a well-established and robust technique that can achieve size-based removal of viruses using membranes with complex multilayer structures. Several studies have shown that the effectiveness of virus filtration can be significantly influenced by the underlying pore size and structure of the membrane as well as the extent of protein fouling. The objective of this thesis is to determine the role of membrane structural properties on the overall performance characteristics of different virus filtration membranes, including both virus capture and protein fouling.

As part of this work, several new methodologies were developed to specifically evaluate the internal pore size / structure of virus filtration membranes using advanced microscopic techniques. Experimental studies were performed using several virus filters, including the highly asymmetric flat sheet Viresolve® Pro and Viresolve® NFP membranes, the flat sheet Ultipor® DV20 membrane which as a relatively homogeneous structure, and the hollow-fiber Planova™ 20N and Planova™ BioEX membranes. These membranes are cast from different polymers (cellulose, polyethersulfone, and polyvinylidene fluoride) and have very different internal pore morphology. Confocal laser scanning microscopy was used to study the capture of fluorescently-labeled nanoparticles of different size (approximately 20, 40, and 100 nm) and with different fluorescent labels

within the pore structure of these commercial virus filters, providing a clear picture of the average pore size gradient within the filters based on the location of the colored bands. More detailed information was obtained by direct visualization of individual captured gold nanoparticles across the entire depth of the filter using scanning electron microscopy. The SEM images showed the capture of 20 nm gold nanoparticles in a very thin band near the exit (skin layer) of the Viresolve® Pro and NFP membranes, with the location consistent with independent estimate of the local pore size. In addition, SEM studies showed that protein fouling shifted the location of the 20 nm nanoparticles in the Viresolve® Pro membrane to further upstream in the filter; this effect was not seen with the Viresolve® NFP membrane.

A novel approach was developed to measure the magnitude of the pore interconnectivity in different virus filters based on the capture profile of nanoparticles within a membrane used with partial blockage of the exit flow surface. Quantitative estimates of the pore interconnectivity were then obtained by comparison of the observed capture profiles with numerical solution of the flow streamlines and simulated particle capture behavior. The Viresolve® Pro filter showed a very high degree of pore interconnectivity, while the Viresolve® NFP and Ultipor® DV20 membranes showed almost no internal lateral flow. These are the first measurements of the pore interconnectivity of either virus filtration membranes or asymmetric membrane structures.

Quantitative data were obtained for the flux decline and virus filter capacity using Immunoglobulin G (IgG) and Bovine Serum Albumin (BSA) as model proteins. The rapid decline in filtrate flux observed with some proteins was due to the presence of large protein

aggregates that block / constrict the membrane pores; this fouling was almost completely eliminated when using “monomeric” protein produced by fractionation of the IgG using size exclusion chromatography. Interestingly, the extent of fouling was reduced when operating at high transmembrane pressures in the Viresolve® Pro (but not the Viresolve® NFP) membrane, which is likely due to the difference in internal pore structure for these membranes. These results provide important insights into the key factors controlling the performance of these widely-used virus filtration membranes for bioprocessing applications.

TABLE OF CONTENTS

LIST OF FIGURES

LIST OF TABLES

ACKNOWLEDGEMENTS

First and foremost, I would like to express my sincere appreciation to my advisor, Dr. Andrew Zydney for not only the endless support on this thesis, but also for teaching me a rigorous approach to scientific research. I truly appreciated his patience, kindness, and enthusiasm at all stages of my doctoral study. I would like to thank my doctoral committee members, Dr. Darrell Velegol, Dr. Michael Hickner, and Dr. Manish Kumar for their advice and feedback to improve this work. I would like to extend my gratitude to Dr. Ali Borhan for all his invaluable support and guidance throughout my graduate study.

My PhD project was financially and intellectually supported by MilliporeSigma, and I have had the great opportunity to work with our amazing collaborators, Dr. Sal Giglia and Dr. Christina Carbrello, that I have always benefited from their insightful questioning and discussion. Also, I would like to thank MilliporeSigma for the donation of Viresolve® Pro and Viresolve® NFP membranes that have been used widely in this work.

Furthermore, I would like to thank my fellow lab mates in Zydney research group for their friendship and helpful discussion including Dr. Youngbin Baek, Mahsa Hadidi, Ying Li, Ivan Manzano, Parinaz Emami, Zhao Li, Mario Jabra, and Chris Yehl. Particularly, I would like to thank Dr. Hadi Nazem Bokaee, who was a post-doc in our lab, and we worked closely on different projects.

Finally, I would like to express my deepest gratitude to my lovely parents, Azar and Rajab Ali, for all their encouragements, sacrifices, and endless love along my way. I would also like to thank my dearest brothers, Hossein and Reza for always being there for me and believing in me at every single stage of my life, your love is priceless! I owe special

thanks to my best friend and life partner, Farzad Mohajerani, whose support and selfless love made this journey easy and possible far away from home and family. I am always proud of all your success and accomplishments.

Chapter 1
Introduction

1.1 Viral Contamination

Many biotherapeutics are commonly expressed in mammalian cell lines or are derived from human plasma. For example, Chinese hamster ovary (CHO) cells are generally used to produce recombinant monoclonal antibodies since these mammalian cells can provide the environment needed for proper folding and post-translational modifications [1–3]. These systems have an inherent risk of viral contamination that could cause serious clinical and economic consequences [4].

Viral contamination of protein-based therapeutics can arise from the use of infected cell lines (endogenous viruses) or from the introduction of contaminated media / water / air / equipment during production (adventitious viruses). Endogenous viruses can be introduced into the master cell line bank through several ways such as: (a) derivation of cell lines from infected animals; (b) use of virus to establish the cell line; (c) use of contaminated biological reagents such as animal serum components; and / or d) contamination during cell handling [5,6]. Many mammalian cell lines produce endogenous retrovirus-like particles which may be constitutively expressed and transmitted to the cell progeny [1,7,8]. Although extensive testing indicates that these particles are almost always noninfectious and they have not been linked to disease in humans, their presence is a safety concern due to risk of activation by superinfection [9].

Adventitious viruses can enter the process through contaminated raw materials, buffers, equipment, and/ or the environment [10,11]. For instance, contamination of raw materials from murine minute virus (MMV) has been reported in a large-scale biologics manufacturing process that was attributed to adventitious viruses [12,13]. Therefore, screening of cell culture parameters and reagents is important for the early detection of potential adventitious viral contamination.

There have been a few isolated incidents over the past decades where virus contamination was detected in bioreactors; there is no evidence that any biotechnology products containing viruses have infected humans (beyond contaminated plasma proteins). For example, in 2008 and 2009, Vesivirus 2117 were found to infect the CHO cell lines used at Genzyme to produce Fabrazyme and Cerezyme, drugs used for the treatment of two rare genetic disorders [14,15]. This lead to the complete plant shutdown and extensive decontamination of the facility, not only impacting the patients who depended on these two vital drugs, but also resulting in significant economic losses that have been estimated at multiple millions of dollars [16].

Human plasma provides a source of therapeutic products such as albumin, gamma globulin, and coagulation factors, all of which pose a risk of transmission of blood-born pathogens. Several outbreaks of hepatitis A and hepatitis C have been reported from the use of contaminated blood-derived products [17–20]. Therefore, providing high levels of viral clearance is an essential part of the downstream purification process in the manufacture of both protein-based biopharmaceuticals and plasma-derived blood products [6].

1.2 Viral Clearance

To ensure the safety of biopharmaceuticals, regulatory agencies such as the Food and Drug Administration (FDA), the European Medicine Evaluation Agency (EMEA), and the Japan Pharmaceutical Manufacturing Association (JPMA) provide guidelines that outline the safety standards for final products. In addition, manufacturers are required to validate the overall viral clearance for their process by quantifying the level of virus reduction obtained during specific steps within the manufacturing processes [21,22]. The safety of biotherapeutics is insured by: a) monitoring the cell line and raw materials for contamination; b) evaluating the capacity of the downstream process for viral clearance; and C) testing for potential viral infection of the product stream at specific points in the manufacturing process.

In order to meet the federal and international guidelines, biopharmaceutical manufacturers are required to employ multiple orthogonal viral clearance steps that rely on independent mechanisms to inactivate and/or physically remove viruses [21,23]. Although the extent of viral clearance depends on the nature of the feed stock, the quality and prescribed dosage of the final product, and the process productivity, the typical target is to insure that there is less than one infectious virus particle per million doses of the final drug product. Based on the product and possible contaminants, most processes require a demonstration of greater than 12–15 log of clearance for endogenous retroviruses and at least 6 logs of clearance for adventitious viruses [22,24]. This can be achieved by designing robust and effective purification processes that provide adequate virus inactivation / removal under a variety of operating conditions.

The viral clearance strategy typically employs a combination of inactivation and physical removal techniques. Inactivation methods include chemical treatments such as using low pH or combinations of appropriate solvents and detergents [7,17], as well as physical treatments like employing heat or radiation [3]. The inactivation technique is chosen based on product stability and the properties of the target virus. Physical removal is generally accomplished by chromatography and / or membrane filtration. Affinity, ion-exchange and hydrophobic interaction chromatography are frequently used for protein purification; the efficiency and robustness of viral clearance for these chromatographic methods depends on the process conditions (e.g., contaminant concentration, flow rate, buffer and washing volumes), the resin binding capacity, and the characteristics of the virus [25,26]. In contrast, membrane filtration removes viruses primarily based on a size-exclusion mechanism, providing robust clearance of both enveloped and non-enveloped viruses irrespective of their surface properties [27].

Due to the high costs associated with virus validation, scale-down process models are employed using appropriate virus surrogates for spiking studies. Regulatory agencies mandate that validation studies consider the actual process specifications, including process operating conditions, buffer formulations, protein concentrations, and virus loading [6,9]. The model viruses selected for spiking tests should be chosen to be representative of the range of potential viral contaminants. This needs to include any suspected virus contaminants. For example, enveloped murine leukemia virus (MuLV) is often used as a model for noninfectious endogenous retroviruses associated with rodent cell lines [26,27].

1.3 Membrane Formation Technologies

Separation technologies using membranes are gaining interests for diverse application in biomolecules purification, liquid or gas separation, desalination, and food processing. Each application imposes specific requirements on the membrane material and membrane structure. The key parameters such as porosity, pore size distribution, selectivity, and permeability determine the efficiency of filtration/ separation. Membranes are manufactured from wide variety of organic (e.g. polymers) and inorganic (e.g. carbon, alumina and zeolites) materials [29]. However, the majority of commercial membranes are made of polymers that can provide high mechanical strength, thermal stability, chemical resistance as well as stable long-term separation properties. Table1.1 indicates a list of most commonly used polymers for membrane fabrication. It is essential to evaluate the membrane performance by measuring the flux, selectivity, membrane fouling, capacity, and mechanical/ thermal tolerance that are directly related to membrane material selection and preparation techniques [30,31].

Table 1.1 The most common polymers used for production of commercial membranes

Membrane Material	Application
Cellulose regenerated	D, UF, MF
Cellulose nitrate	MF
Cellulose acetate	GS, RO, D, UF, MF
Polyamide	RO, NF, D, UF, MF
Polysulfone	GS, UF, MF
Poly(ether sulfone)	UF, MF
Polycarbonate	GS, D, UF, MF
Poly(ether imide)	UF, MF
Poly(2,6-dimethyl-1,4-phenylene oxide)	GS
Polyimide	GS
Poly(vinylidene fluoride)	MF, UF
Polytetrafluoroethylene	MF
Polypropylene	MF
Polyacrylonitrile	D, UF, MF
Poly(methyl methacrylate)	D, UF
Poly(vinyl alcohol)	PV
Polydimethylsiloxane	PV, GS

MF = microfiltration; UF = ultrafiltration; NF = nanofiltration; D = dialysis; PV = pervaporation; GS = gas separation.

Generally, membranes can be classified according to their geometry, internal structure, fabrication methods, and application. Membranes can be produced in laminar, hollow tubes or fibers, wafers geometry and packaged in a variety of different module configurations, including plate and frame, spiral wound, and hollow fiber with different surface area to bulk volume ratio. Although spiral wound and plate and frame modules are used considerably in large-scale separation processes and can tolerate higher operating pressure, hollow fiber design provides the highest membrane packing density per module volume [31].

Membranes are principally divided as symmetric and asymmetric membranes based on their morphology and structure. Symmetric porous membranes have cylindrical,

sponge/web/slit-like structure with uniform pore size throughout the membrane cross-section which allows the entire membrane to act as a selective layer. These membranes have relatively same porosity and retention characteristics throughout the membrane depth and are widely used in dialysis, microfiltration, and ultrafiltration applications. Filtration using symmetric membranes tends to become progressively less efficient as membrane pores become blocked/ constricted due to fouling. In contrast, asymmetric membranes consist of a 0.1-5 μm-thick skin layer on a highly porous substructure with 50-200 μm thickness that provides mechanical support. The skin and supporting layers can be fabricated from either same or different materials, which is known as integrally-skinned asymmetric membrane or a composite membrane, respectively. In addition, the separation characteristics of an asymmetric membrane are regulated by nature of the material and pore size distribution of skin (selective) layer, while the membrane throughput is primarily determined by the thickness of the skin layer [32,33].

There are several methodologies to prepare the symmetric and asymmetric polymeric membranes, such as track etching, stretching, sintering, and phase separation processes. Typically, polymeric porous membranes are produced by phase inversion (phase separation) which is a controlled transformation of polymer solution in two phases: one with high polymer concentration and one with low polymer concentration [30,34,35]. The concentrated phase solidifies using the following techniques and forms the membrane:

1.3.1 Immersion Precipitation

Phase inversion through immersion precipitation is the most widely used technique for manufacturing of polymeric membranes with porous and asymmetric structure, particularly ultrafiltration and microfiltration membranes. In this process which is also known as non-solvent induced phase separation, there are three components: polymer, solvent, and nonsolvent. The polymer is dissolved in an appropriate solvent and the resulting solution is cast on a proper supporting layer and immersed in a coagulation bath containing a nonsolvent (generally water), where the polymer precipitation occurs due to the solvent and nonsolvent exchange [29,36]. Generally, the pore size and structure of the membranes depend on several factors such as the polymer concentration, the nonsolvent, the additives and the precipitation time and temperature. For instance, if the polymer concentration increases, the membrane pore size and porosity decrease which leads to formation of sponge-like structure and decrease in membrane flux. In addition, the choice of solvent and nonsolvent significantly impacts the morphology and properties of the membrane. If the polymer has a high solubility in the solvent, a membrane that is formed will obtain high porosity [37].

1.3.2 Thermally Induced Phase Separation (TIPS)

In this process, polymer is dissolved in a solvent at high temperature and the polymer solution is cast on the support. The temperature is reduced to induce the demixing of the homogenous polymer solution and the phase separation occurs at a set temperature.

Unique advantages of this technique are: possibility to obtain well-interconnected polymer network, process simplicity, high porosity, and the ability to create microstructure that have narrow pore size distribution. TIPS is widely adopted to prepare symmetric microfiltration membranes [29,34].

1.3.3 Vapor Induced Phase Separation (VIPS)

In this method, once a polymer solution is cast on the support, it is exposed to an environment containing a nonsolvent (usually exposed to air that contains water vapor as a nonsolvent), which is adsorbed by the polymer solution and a porous membrane forms due to the demixing [38].

1.3.4 Evaporation Induced Phase Separation (EIPS)

In this case, a homogenous polymer solution which contains two or more solvents of different dissolution capacities and a nonsolvent is cast on a support, the evaporation of the solvent occurs due to high volatility and causing the solution to have higher component of nonsolvent and polymer. This results in forming a thin porous and skinned membrane [29,34].

Overall, the final morphology of the membranes varies significantly, depending on the material properties (e.g., type of polymer, solvent and nonsolvent), process condition (e.g., bath temperature and humidity), kinetic parameters (e.g., solvent and nonsolvent exchange rate) and thermodynamic parameters (e.g., solvent and polymer interaction). The

performance of the membranes strongly depends on morphology formed during the phase separation.

1.4 Virus Filtration Membranes

Virus filtration is widely used as an essential part of the downstream purification process during the manufacture of protein-based biotherapeutics derived from mammalian cell lines or blood plasma [8,11,39]. Virus filters are designed to provide more than 95% transmission (yield) for the product of interest with 99.99% retention of the target viruses (minimum of 4-log reduction in virus titer).

Commercially available virus filters are commonly classified based on the size of the target virus. Retrovirus filters can remove viruses with sizes of 80-110 nm, while parvovirus filters can retain viruses as small as 18-26 nm. Parvovirus filtration is particularly challenging because most therapeutic proteins are 5-10 nm in size, which is only slightly smaller than viruses [27,40]. Most parvovirus filters are cast in a multi-layer format that employ two or more membranes that are physically layered in a single module to provide the high level of virus retention required in these applications [41–43]. The individual layers are commonly asymmetric or composite structures, consisting of a thin skin layer that provides the high degree of virus retention and a microporous layer that provides the required mechanical support.

Virus filtration membranes were originally designed to conduct separation in tangential flow filtration (TFF) to reduce concentration polarization effects, with the

membrane retentive layer facing the feed stream[44,45]. However, improvements in membrane performance has led to the implementation of normal flow filters operated with the membrane skin layer oriented downstream [41]. Normal flow filters are considerably less expensive than TFF systems and are simpler to operate [16,40,44].

Currently, MilliporeSigma, Pall Corporation, Asahi Kasei Medical, and Sartorius Biotech specifically design and manufacture commercial virus filtration membranes with various pore structure, morphology, and material. Virus filters are made from surface modified polyvinylidene fluoride (PVDF), polyethersulfone (PES), and regenerated cellulose (RC), with both symmetric and asymmetric structures and in the form of flat sheet or hollow fiber membranes.

MilliporeSigma has fabricated a number of skinned asymmetric virus filters including the Viresolve® 70, Viresolve® 180, Viresolve® NFP, and Viresolve® Pro. The Viresolve® 70 and 180 filters are made of PVDF with a hydrophilic surface; these membranes are designed to use in tangential flow filtration for the transmission of proteins with 70 and 180 kDa molecular weight, respectively. The Viresolve® NFP and Viresolve® Pro membranes are made of PVDF and hydrophilic PES, respectively. Both membranes are used in normal flow filtration and are designed to remove parvoviruses as small as 20 nm in size.

Pall Corporation has manufactured the Ultipor® DV20 and Pegasus™ SV4 membranes, both made of hydrophilic PDVF with a relatively homogenous pore structure. These membranes provide high viral clearance of parvovirus by using two-layers of the

membrane, one on top of the other. The Ultipor® DV50 membrane with three discrete layers is designed to remove retroviruses larger than 50 nm.

Asahi Kasei Medical has developed several parvovirus filters, including the Planova™ 15N, 20N, and BioEx membranes all in hollow fiber format. The Planova™ N series are made from a naturally hydrophilic cuprammonium regenerated cellulose, while the Planova™ BioEX hollow fibers are made from hydrophilized polyvinylidene fluoride (PVDF).

An effective virus filter must provide high capacity and high selectivity. The capacity is defined as the total volume of feed solution that can be processed before the flux declines to an unacceptably low value during constant pressure operation. The selectivity refers to the ability of the virus filter to pass the product of interest while retaining very high levels of virus. The virus retention is typically described in the terms of the log reduction value (LRV):

$$LRV = -Log_{10}\left(\frac{C_{permeate}}{C_{feed}}\right) \tag{1.1}$$

where $C_{permeate}$ and C_{feed} are the virus concentrations in the permeate and feed streams, respectively. Most virus retentive filters provide a LRV of at least 3, with typical targets of 5 or greater.

1.5 Membrane Fouling

Virus filtration has been widely used as an essential part of the downstream purification process during the manufacturing of monoclonal antibodies. These filters provide high removal of both enveloped and nonenveloped viruses while having minimal impact on the quality of the biological product [27,46]. One of the critical issues associated with the use of virus filters is membrane fouling, which can significantly alter both the filtrate flux and the membrane filtration [47,48]. Since virus filtration is generally conducted toward the end of the downstream purification process, the feed stream is highly purified, with the fouling due primarily to the protein product or product-related impurities such as aggregates [49]. Fouling occurs due to complex physical and chemical interactions between the proteins and membrane that lead to the deposition or adsorption of proteins onto the membrane surface or within the membrane pores[50,51]. Protein fouling is a function of the membrane properties such as porosity, pore size, morphology, and surface chemistries as well as the process conditions, including buffer pH and ionic strength, membrane orientation, and operating pressure [52,53]. Most asymmetric virus filters are operated with the tight pores facing downstream (away from the feed), with the any large aggregates / impurities captured within the larger pores in the membrane support structure which effectively acts as a pre-filter [52,54].

There have been many studies focused on understanding the fouling behavior of microfiltration and ultrafiltration membranes, but these results are not applicable to virus filtration due to the very similar size of the proteins and retentive pores in the virus filter. For example, most models of protein fouling assume that the membranes consist of a

parallel array of cylindrical pores with uniform size, which is clearly not valid for asymmetric virus filters where the pore size varies by more than one order of magnitude from the filter inlet to outlet [55,56].

Fouling within the membrane pore is usually described by either pore constriction, which reduces the pore radius, or pore blockage, which reduces the pore density. Protein fouling is typically identified by a decline in flux (at constant transmembrane pressure) or an increase in pressure (at constant flux), although fouling often results in significant changes in both protein transmission and virus retention [57]. Therefore, a fundamental understanding of the factors governing the fouling characteristics of virus filtration membranes is critical for the effective use of virus filtration in bioprocessing applications.

1.6 Membrane Characterization

The primary mechanism for retention of both parvoviruses and retroviruses during virus filtration is assumed to be size exclusion, although there is some evidence that longer range (e.g., electrostatic) interactions can also affect the extent of virus retention. The overall performance of virus filtration process is highly influenced by membrane structural properties such as the membrane pore size distribution and the membrane pore size gradient (the variation in pore size through the depth of the filter) [58,59].

A large number of characterization techniques have been developed to determine the pore size and structure of various membranes. This includes bubble point, gas adsorption, gas diffusion, displacement porosimetry, dextran sieving test, and electron microscopy. Each of these techniques have distinct advantages and limitations. For

instance, gas-liquid displacement porosimetry evaluates the flow rate of a gas as it displaces the liquid in the pores of a previously wetted membrane. However, this technique requires very high pressures when used for membranes with small pores, which can cause significant alteration in the underlying membrane. This issue can be minimized using liquid-liquid displacement porosimetry using immiscible liquids with very low interfacial tension, but neither of these porosimetry techniques provides any information on the asymmetry of the pore structure [60,61]. Dextran sieving tests can provide information on the retention characteristics of different membranes [62–64], but the approach also provides no information on the pore asymmetry and the rate of dextran transport can also be affected by concentration polarization, dextran elongation, and dextran interactions with the membrane [65].

Alternatively, the membrane pore size and morphology can be probed using different microscopic methods. Bakhshayeshi et al. [58] used confocal laser scanning microscopy with fluorescently labeled bacteriophage to identify the location of virus capture within flat-sheet membranes with very different pore structure. Scanning electron microscopy (SEM) has also been used to examine the pore size distribution of different membranes, but the resolution between the pores and polymer is often poor and the need to cut the membrane can generate artifacts in the pore structure [60,66]. None of the currently available imaging techniques have been able to provide accurate measurement of the detailed pore size distribution or asymmetry of commercially available virus filtration membranes.

1.7 Research Overview

The overall objective of this thesis is to determine the role of membrane structural properties on the overall performance characteristics of different virus filtration membranes, most particularly the detailed mechanisms controlling both virus capture and protein fouling. This required the development of several new methodologies specifically designed to evaluate the internal pore size / structure of virus filtration membranes.

Chapter 2 discusses the use of fluorescently labeled nanoparticles as virus surrogates, providing a novel approach to study the retention properties of virus filtration membranes by direct visualization of the location of captured nanoparticles of different size (and different fluorescence) using confocal microscopy.

Chapter 3 describes the use of scanning electron microscopy with gold nanoparticles to study the internal pore size and morphology of different virus filtration membranes, including both flat sheet and hollow fiber membranes. In contrast to confocal microscopy, which has relatively limited resolution, scanning electron microscopy provides resolution of individual nanoparticles within the depth of the virus filter.

Chapter 4 examines the affects of protein fouling on nanoparticle capture within different virus filtration membranes using both confocal and scanning electron microscopy, with the changes in the location of the nanoparticles related to the nature of the membrane fouling.

Chapter 5 presents a new technique for evaluating the pore interconnectivity in asymmetric membranes based on the location of captured nanoparticles within the pores of a membrane that is partially blocked at the flow exit. This pore blockage causes a distortion

in the flow streamlines, which is captured in the nanoparticle capture profile and can be analyzed by solving the governing flow equations within the membrane.

Chapter 6 explores the effect of transmembrane pressure on the filtrate flux and overall filter capacity during protein filtration through virus filters, with the rate of flux decline data used to obtain insights into the underlying mechanisms governing membrane fouling.

Chapter 7 summarizes the major conclusions of this dissertation and provides recommendations for future studies on improving the performance of virus filtration membranes.

1.8 Literature Cited

[1] S. Adamson, Experiences of virus, retrovirus and retrovirus-like particles in Chinese hamster ovary (CHO) and hybridoma cells used for production of protein therapeutics, Dev. Biol. Stand. 83 (1994) 31–44.

[2] H. Rabenau, V. Ohlinger, J. Anderson, B. Selb, J. Cinantl, W. Wolf, J. Frost, P. Mellor, H. Wilhelm Doerr, Contamination of genetically engineered CHO-cells by epizootic haemorrhagic disease virus (EHDV), Biologicals. 21 (1993) 207–214.

[3] P. Roberts, Virus Safety in Bio Products, J. Chem. Technol. Biotechnol. 59 (1994) 110–111.

[4] A. Berting, M.R. Farcet, T.R. Kreil, Virus susceptibility of Chinese hamster ovary (CHO) cells and detection of viral contaminations by adventitious agent testing, Biotechnol. Bioeng. 106 (2010) 598–607. doi:10.1002/bit.22723.

[5] R.E. Benveniste, G.J. Todaro, Multiple divergent copies of endogenous C-type virogenes in mammalian cells, Nature. 252 (1974) 170–173.

[6] International Conference on Harmonization (ICH) of Technical Requirements for Registration of Pharmaceuticals for Human Use, Guidance for Industry: Q5A, Viral safety evaluation of biotechnology products derived from cell lines of human or animal origin, 1999.

[7] K. Brorson, S. Krejci, K. Lee, E. Hamilton, K. Stein, Y. Xu, Bracketed generic inactivation of rodent retroviruses by low pH treatment for monoclonal antibodies and recombinant proteins, Biotechnol. Bioeng. 82 (2003) 321–329.

[8] G. Miesegaes, S. Lute, K. Brorson, Analysis of viral clearance unit operations for monoclonal antibodies, Biotechnol. Bioeng. 106 (2010) 238–246. doi:10.1002/bit.22662.

[9] N.Z. Khan, J.J. Parrella, P.W. Genest, M.S. Colman, Filter preconditioning enables representative scaled-down modelling of filter capacity and viral clearance by mitigating the impact of virus spike impurities, 301 (2009) 293–301. doi:10.1042/BA20080133.

[10] F. Hesse, R. Wagner, Developments and improvements in the manufacturing of human therapeutics with mammalian cell cultures, Trends Biotechnol. 18 (2000) 173–180.

[11] G. Sofer, J. Carter, Viral Clearance: A strategy for quality by design and the design space, in: A. Rathore, R. Mhatre (Eds.), Qual. by Des. Biopharm., John Wiley & Sons, Inc., Hoboken, NJ, USA, 2008: pp. 143–159.

doi:10.1002/9780470466315.ch8.

[12] R.L. Garnick, Experience with viral contamination in cell culture, Dev. Biol. Stand. 88 (1996) 49–56.

[13] R. Garnick, Raw materials as a source of contamination in large-scale cell culture, Dev. Biol. Stand. 93 (1998) 21–29.

[14] L. Bush, Genzyme detects virus contamination of bioreactor, halts production, BioPharm Int. (2009).

[15] V. Bethencourt, Virus stalls Genzyme plant, Nat. Biotechnol. 27 (2009) 681–681. doi:10.1038/nbt0809-681a.

[16] S. Liu, M. Carroll, R. Iverson, C. Valera, J. Vennari, K. Turco, R. Piper, R. Kiss, H. Lutz, Development and qualification of a novel virus removal filter for cell culture applications, Biotechnol. Prog. 16 (2000) 425–434. doi:10.1021/bp000027m.

[17] B. Horowitz, M. Wiebe, A. Lippin, M. Stryker, Inactivation of viruses in labile blood derivatives. I. Disruption of lipid-enveloped viruses by tri(n-butyl)phosphate detergent combinations, Transfusion. 25 (1985) 516–522.

[18] J. Blumel, D. Musso, S. Teitz, T. Miyabayashi, K. Boller, B.S. Schnierle, S.A. Baylis, Inactivation and removal of Zika virus during manufacture of plasma-derived medicinal products, Transfusion. 57 (2017) 790–796. doi:10.1111/trf.13873.

[19] V.S. Blanchette, E. Vorstman, A. Shore, E. Wang, M. Petric, B.W. Jett, H.J. Alter, Hepatitis C infection in children with hemophilia A and B, Blood. 78 (1991) 285–289. http://www.ncbi.nlm.nih.gov/pubmed/1712646.

[20] T.W. Ellgaard, L. Bindslev, S. Kamstrup, Evaluation of the virus clearance capacity and robustness of the manufacturing process for the recombinant factor VIII protein, turoctocog alfa, Protein Expr. Purif. 129 (2017) 94–100. doi:10.1016/j.pep.2016.09.002.

[21] European Medicines Agency Evaluation of Medicines (EMEA), Guideline on virus safety evaluation of biotechnological investigational medicinal products, 2006.

[22] H. Aranha, S. Forbes, Viral clearance strategies for biopharmaceutical safety Part II : A multifaceted approach to process validation, BioPharm Int. 14 (2001) 43–54.

[23] J.X. Zhou, Orthogonal virus clearance applications in monoclonal antibody production, Process Scale Purif. Antibodies. (2009) 169–186.

[24] D. Strauss, D. Chen, S. O'Donnell, J. Gao, J. Stuckey, W. Luo, A. Venkiteshwaran, M. Quertinmont, A novel approach to achieving modular retrovirus clearance for a parvovirus filter, Biotechnol. Prog. 30 (2013) 79–85. doi:10.1002/btpr.1820.

[25] S. Curtis, K. Lee, G.S. Blank, K. Brorson, Y. Xu, Generic / matrix evaluation of SV40 clearance by anion exchange chromatography in flow-through mode, Biotechnol. Bioeng. 84 (2003) 179–186.

[26] R. Cameron, K. Smith, Virus clearance methods applied in bioprocessing operations: an overview of selected inactivation and removal methods, Pharm Bioprocess. 2 (2014) 75–83. doi:10.4155/pbp.13.61.

[27] M. Krishnan, G. Kern, Virus removal by filtration: Points to consider, BioPharm Int. (2006).

[28] A.A. Shukla, M.R. Etzel, S. Gadam, eds., Process scale bioseparations for the

biopharmaceutical industry, CRC Press, 2007. doi:10.1201/9781420016024.

[29] P. Van De Witte, J.W.A. Van Den Berg, J. Feijen, Phase separation processes in polymer solutions in relation to membrane formation, 117 (1996) 1–31.

[30] L.J. Zeman, A. Zydney, Microfiltration and ultrafiltration : Principles and applications, CRC Press, 2017.

[31] I. Pinnau, B.D. Freeman, Formation and Modification of Polymeric Membranes: Overview, Am. Chem. Soc. (2000).

[32] C. Barth, M.C. Gonçalves, A.T.N. Pires, J. Roeder, B.A. Wolf, Asymmetric polysulfone and polyethersulfone membranes: effects of thermodynamic conditions during formation on their performance, Am. Chem. Soc. 169 (2000) 287–299.

[33] E. Klein, J.K. Smith, Asymmetric membrane formation solubility parameters for solvent selection, Ind. Eng. Chem. Prod. Res. Dev. 11 (1972) 207–210. doi:10.1021/i360042a017.

[34] T.H. Young, L.W. Chen, Pore formation mechanism of membranes from phase inversion process, Desalination. 103 (1995) 233–247.

[35] C.A. Smolders, A.J. Reuvers, R.M. Boom, I.M. Wienk, Microstructures in phase-inversion membranes . Part 1 . Formation of macrovoids, J. Membr. Sctence,. 73 (1992) 259–275.

[36] H. Strathmann, K. Kock, P. Amar, W.R. Baker, The formation mechanism of asymmetric membranes, Desalination. 16 (1975) 179–203.

[37] G.R. Guillen, G.Z. Ramon, H.P. Kavehpour, R.B. Kaner, E.M. V Hoek, Direct microscopic observation of membrane formation by nonsolvent induced phase

separation, J. Memb. Sci. 431 (2013) 212–220. doi:10.1016/j.memsci.2012.12.031.

[38] T. Marino, F. Russo, A. Figoli, H. May, The formation of polyvinylidene fluoride membranes with tailored properties via vapour / non-solvent induced phase separation, Membranes (Basel). (2018) 1–17. doi:10.3390/membranes8030071.

[39] T. Ireland, H. Lutz, M. Siwak, G. Bolton, Viral filtration of plasma-derived human IgG, Pharm. Technol. Eur. 18 (2006) 43–49.

[40] H. Brough, H; Antoniou, C; Carter, J; Jakubik, J; Xu, Y; Lutz, Performance of a novel Viresolve NFR virus filter, Biotechnol. Prog. 18 (2002) 782–795.

[41] A.L. Zydney, Membrane technology for purification of therapeutic proteins, Biotechnol. Bioeng. 103 (2009) 227–230. doi:10.1002/bit.22308.

[42] R. van Reis, A. Zydney, Membrane separations in biotechnology, Curr. Opin. Biotechnol. 12 (2001) 208–211.

[43] D.M. Bohonak, A.L. Zydney, Compaction and permeability effects with virus filtration membranes, J. Memb. Sci. 254 (2005) 71–79. doi:10.1016/j.memsci.2004.12.035.

[44] S.R. Wickramasinghe, Tangential-flow filtration for virus capture, in: N.N. Li, A.G. Fane, W.S.W. Ho, T. Matsuura (Eds.), Adv. Membr. Technol. Appl., John Wiley & Sons, Inc., Hoboken, NJ, USA, 2008. doi:10.1002/9780470276280.ch20.

[45] S.R. Wickramasinghe S. Ranil, E.D. Stump, D.L. Grzenia, S.M. Husson, J. Pellegrino, Understanding virus filtration membrane performance, J. Memb. Sci. 365 (2010) 160–169. doi:10.1016/j.memsci.2010.09.002.

[46] T. Burnouf, M. Radosevich, Nanofiltration of plasma-derived biopharmaceutical

products, Haemophilia. 9 (2003) 24–37.

[47] A.D. Marshall, P.A. Munro, G. Trägårdh, The effect of protein fouling in microfiltration and ultrafiltration on permeate flux, protein retention and selectivity: A literature review, Desalination. 91 (1993) 65–108. doi:10.1016/0011-9164(93)80047-Q.

[48] G. Bolton, D. Lacasse, R. Kuriyel, Combined models of membrane fouling : Development and application to microfiltration and ultrafiltration of biological fluids, J. Memb. Sci. 277 (2006) 75–84. doi:10.1016/j.memsci.2004.12.053.

[49] B.F. Marques, D.J. Roush, K.E. Goklen, Virus filtration of high-concentration monoclonal antibody solutions, Biotechnol. Prog. 25 (2009) 483–491. doi:10.1021/bp.177.

[50] G. Bolton, M. Cabatingan, M. Rubino, S. Lute, K. Brorson, M. Bailey, Normal-flow virus filtration: detection and assessment of the endpoint in bio-processing., Biotechnol. Appl. Biochem. 42 (2005) 133–142. doi:10.1042/BA20050056.

[51] P. Misra, A. Sinha, A.S. Rathore, A. Shukla, F.Q. Mir, A three plus three parameters mechanistic model for viral filtration, Biotechnol. Prog. 33 (2017) 1538–1547. doi:10.1002/btpr.2523.

[52] Z.H. Syedain, D.M. Bohonak, A.L. Zydney, Protein fouling of virus filtration membranes: Effects of membrane orientation and operating conditions, Biotechnol. Prog. 22 (2006) 1163–1169. doi:10.1021/bp050350v.

[53] M. Bakhshayeshi, A.L. Zydney, Effect of solution pH on protein transmission and membrane capacity during virus filtration, Biotechnol. Bioeng. 100 (2008) 108–117.

doi:10.1002/bit.21735.

[54] D. Nanda, K.L. Tung, Y.L. Li, N.J. Lin, C.J. Chuang, Effect of pH on membrane morphology, fouling potential, and filtration performance of nanofiltration membrane for water softening, J. Memb. Sci. 349 (2010) 411–420. doi:10.1016/j.memsci.2009.12.004.

[55] C.C. Ho, A.L. Zydney, Theoretical analysis of the effect of membrane morphology on fouling during microfiltration, Sep. Sci. Technol. 34 (1999) 2461–2483. doi:10.1081/SS-100100785.

[56] I.M. Griffiths, A. Kumar, P.S. Stewart, A combined network model for membrane fouling, J. Colloid Interface Sci. 432 (2014) 10–18. doi:10.1016/j.jcis.2014.06.021.

[57] R. Chan, V. Chen, Characterization of protein fouling on membranes: Opportunities and challenges, J. Memb. Sci. 242 (2004) 169–188. doi:10.1016/j.memsci.2004.01.029.

[58] M. Bakhshayeshi, N. Jackson, R. Kuriyel, A. Mehta, R. van Reis, A.L. Zydney, Use of confocal scanning laser microscopy to study virus retention during virus filtration, J. Memb. Sci. 379 (2011) 260–267. doi:10.1016/j.memsci.2011.05.069.

[59] D. Lacasse, P. Genest, K. Pizzelli, P. Greenhalgh, L. Mullin, A. Slocum, Impact of process interruption on virus retention of small-virus filters, Bioprocess Int. 11 (2013) 32–44.

[60] J.I. Calvo, R.I. Peinador, P. Prádanos, L. Palacio, A. Bottino, G. Capannelli, A. Hernández, Liquid-liquid displacement porometry to estimate the molecular weight cut-off of ultrafiltration membranes, Desalination. 268 (2011) 174–181.

doi:10.1016/j.desal.2010.10.016.

[61] S. Giglia, D. Bohonak, P. Greenhalgh, A. Leahy, Measurement of pore size distribution and prediction of membrane filter virus retention using liquid-liquid porometry, J. Memb. Sci. 476 (2015) 399–409. doi:10.1016/j.memsci.2014.11.053.

[62] M. Bakhshayeshi, D.M. Kanani, A. Mehta, R. van Reis, R. Kuriyel, N. Jackson, A.L. Zydney, Dextran sieving test for characterization of virus filtration membranes, J. Memb. Sci. 379 (2011) 239–248. doi:10.1016/j.memsci.2011.05.067.

[63] M. Bakhshayeshi, H. Zhou, C. Olsen, W. Yuan, A.L. Zydney, Understanding dextran retention data for hollow fiber ultrafiltration membranes, J. Memb. Sci. 385–386 (2011) 243–250. doi:10.1016/j.memsci.2011.09.047.

[64] S.R. Wickramasinghe, S.E. Bower, Z. Chen, A. Mukherjee, S.M. Husson, Relating the pore size distribution of ultrafiltration membranes to dextran rejection, J. Memb. Sci. 340 (2009) 1–8. doi:10.1016/j.memsci.2009.04.056.

[65] R.I. Peinador, J.I. Calvo, K. ToVinh, V. Thom, P. Prádanos, A. Hernández, Liquid-liquid displacement porosimetry for the characterization of virus retentive membranes, J. Memb. Sci. 372 (2011) 366–372. doi:10.1016/j.memsci.2011.02.022.

[66] F.J. Márquez-Rocha, M. Aguilar-Juárez, M.J. Acosta-Ruíz, M.I. Gradilla, Rapid characterization of ultrafiltration membranes by scanning electron microscopy, Russ. Chem. Bull. 50 (2001) 1320–1322. doi:10.1023/A:1014043815086.

Chapter 2
Use of Fluorescently-labeled Nanoparticles to Study Pore Morphology and Virus Capture in Virus Filtration Membranes

The work presented in this Chapter is based on the material published in:
Fallahianbijan, F., S. Giglia, C. Carbrello, A.L. Zydney, "Use of fluorescently-labeled nanoparticles to study pore morphology and virus capture in virus filtration membranes," J. Membrane Sci., 536: 52-58 (2017).

2.1 Introduction

Most recombinant therapeutic products, including essentially all monoclonal antibodies, are expressed in mammalian cell lines like Chinese Hamster Ovary (CHO) cells [1]. These cells often contain endogenous retroviruses, and there is also a significant risk of contamination by adventitious parvoviruses introduced into the system through various media, equipment, and / or the environment [2,3]. Providing high levels of viral clearance is an essential part of the downstream purification process in the manufacture of these protein-based biopharmaceuticals as well as in the production of plasma-derived blood products [4]. To ensure the safety of biotherapeutics, regulatory agencies require multiple viral clearance steps to inactivate and / or remove viruses. Examples include physical inactivation (e.g., UV or gamma radiation), chemical inactivation (e.g., low pH or combinations of appropriate solvents and detergents), adsorptive processes (e.g., affinity or ion exchange chromatography), and size-based separations like membrane filtration [5–9].

Virus filtration is a robust technique that removes viruses primarily on the basis of size, including both enveloped and non-enveloped virus particles. Virus filters are designed

so that the product of interest passes through the membrane pores while at least 99.99% of the viruses are retained by the filter (providing a minimum of 4-log reduction in virus titer) [10]. Virus filtration is currently performed using disposable normal flow filters due to their ease of operation and low cost [11]. Most commercial virus filters are asymmetric, with the more open side of the membrane placed facing the feed; this leads to significantly greater capacity since the open support region acts as a prefilter, removing protein aggregates and large foulants thereby protecting the virus-retentive layer [10].

Several studies have shown that there can be large differences in the overall performance characteristics of different virus filters [12–14]. For example, Lute et al. showed that a variety of parvovirus filters with high initial retention of small PP7 and ϕx174 bacteriophages (used as model viruses), showed dramatically different rates of filtrate flux decline, with only some of the filters showing a significant reduction in virus retention at high throughput [12]. Jackson et al. found no decline in filtrate flux during filtration of purified PP7 suspensions through a relatively homogeneous Ultipor® DV20 virus filter, but there was still a 2-log decline in virus retention [15], which the authors attributed to an internal concentration polarization phenomenon. There have also been large differences reported in the virus retention behavior after a process disruption, e.g., when switching between feed tanks or when using a buffer flush to recover residual product [16]. For example, Dishari et al. [17] observed a significant spike in virus transmission after a process disruption (in this case a release in the transmembrane pressure) with the DV20 and Viresolve® NFP filters, while there was no change in virus retention for the

Viresolve® Pro filter. The origin of these differences in virus retention behavior is still a subject of considerable discussion.

In order to obtain more fundamental insights into virus retention mechanisms, Bakhshayeshi et al. [18] used confocal microscopy with fluorescently-labeled bacteriophage to directly observe viruses captured in the interior of commercially-available virus filters. This work was subsequently extended by Dishari et al. [13] using a two fluorescent-dye technique to directly visualize virus capture before and after a pressure disruption. In this case, the DV20 and Viresolve® NFP filters showed migration of previously captured virus within the membrane after a process disruption, which the authors correlated with the observed increase in virus transmission immediately after the process disruption.

Although the use of fluorescently-labeled bacteriophage has provided important insights into virus capture phenomena, there are a number of challenges with this experimental approach. First, it is difficult to remove residual proteins and cell debris from the phage preparation, which could lead to membrane fouling and / or artifacts in the confocal images, e.g., adsorption of hydrophobic contaminants to the virus filter. In addition, easily cultured bacteriophage are only available in a limited range of size and surface characteristics, and it can be difficult to obtain suspensions with the high phage concentrations needed for confocal microscopy due to limitations with the cell culture and purification processes. Pontius et al. [19] examined the use of fluorescent microspheres (26 and 67 nm in size) as surrogates for studying virus filtration, but these studies were limited

to the evaluation of virus retention (log-removal) without any information on the underlying mechanisms governing virus capture.

The objective of this study was to demonstrate the use of confocal microscopy with fluorescently-labeled nanoparticles having different size (around 20, 40, and 100 nm) to study the internal pore structure and virus capture behavior of different virus filters. Experiments were performed with relatively homogenous Ultipor® DV20 membranes and highly asymmetric Viresolve® Pro membranes, both of which are designed to remove small (20 nm size) parvovirus. Results obtained with the 20 nm nanoparticles were similar to previous images obtained with similarly-sized labeled bacteriophage, providing important validation of the method. Confocal images obtained with the different size nanoparticles provide new insights into the morphology and virus capture behavior of the different virus filters.

2.2 Materials and Methods

2.1.1 Virus Filters

All experiments were performed using commercially-available virus filters: the highly asymmetric Viresolve® Pro filters were provided by MilliporeSigma (Bedford, MA) while the more homogeneous Ultipor® DV20 filters were obtained from Pall Corp. (Port Washington, NY). The membranes were used in single layer format to facilitate observation by confocal microscopy; the commercial filters both employ two layers of the

membrane to obtain the high levels of virus removal needed in this application. The Viresolve® membranes were cut into 47 mm disks from large sheet-stock.

2.2.1 Solution Preparation

Tris buffer solutions were prepared by dissolving 5 mM of NaCl (3624-01, J.T. Baker, NJ) and 5 mM of Tris(hydroxymethyl)aminomethane (EMD Chemicals Inc., NJ) in deionized distilled water obtained from a NANOpure® water purification system (Model D11911, Barnstead/Thermodyne Co., Dubuque, IA) with resistivity greater than 18 MΩ cm. The solution pH was determined using a model 420Aplus Thermo Orion pH meter (Orion Technology, Beverly, MA) and adjusted to 7.5 by adding 1 M HCl as needed. Buffer solutions were pre-filtered through 0.2 μm pore-size Supor® 200 membranes (Pall Corp., Ann Arbor, MI) to remove any particles or un-dissolved salts prior to use.

Carboxylate-modified, fluorescently-labeled polystyrene latex nanospheres (FluoSpheres®) were obtained from Molecular Probes, Inc. (Eugene, OR), with stock concentrations and excitation / emission wavelengths summarized in Table 2.1 The size and zeta potential of the different nanoparticles were determined by dynamic light scattering (DLS) and electrophoretic light scattering measurements, respectively, both using a Zetasizer Nano ZS (Malvern Instruments Ltd, Worcestershire, UK). Both yellow-green and red 20 nm nanoparticles were used along with purple 40 nm nanoparticles and red 100 nm nanoparticles. The FluoSpheres® were diluted with Tris buffer and ultrasonicated for 5 min prior to use in the virus filtration experiments.

2.2.2 Filtration of Fluorescently-labeled Nanospheres

Filtration experiments were conducted using single layer membranes placed in a 47 mm diameter stainless steel filter holder (MilliporeSigma, Bedford, MA). Most experiments were performed with the membrane oriented with the skin (or shiny) side down (away from the feed); limited data were obtained with the membrane in the reverse (skin-side up) orientation to obtain additional insights into the membrane structure. The holder was connected to a feed reservoir with plastic tubing. The feed reservoir and filter holder were initially flushed with at least 40 mL of Tris buffer to thoroughly wet the membrane and remove any air bubbles from the system. The reservoir was then emptied, refilled with a suspension of nanospheres, and re-pressurized to 210 kPa (30 psig). The pressure was maintained constant throughout the filtration using an Aschcroft pressure regulator. At the end of the filtration, the membrane was removed from the holder, cut into small pieces of about 1 cm × 1 cm, and mounted on a glass slide. The membrane was kept wet with a small drop of 10% glycerol, covered with a coverslip, and sealed to the glass slide using nail polish.

2.2.3 Confocal Laser Scanning Microscopy

The fluorescently labeled nanospheres captured within the virus filter were visualized with an Olympus Fluoview^{TM} 1000 confocal laser scanning microscope (Olympus American Inc., New Jersey). The yellow-green, red, and dark-red nanospheres were excited with 488 nm (blue), 543 nm (green), and 633 nm (red) lasers, respectively.

The emitted fluorescent light was collected through a 100x oil objective lens. A z-image through the depth of filter was constructed by stacking multiple x-y cross-sections obtained at 0.5 µm intervals using the Olympus Fluoview™ software. Since the maximum scanning depth of the oil objective lens was 80 µm, the 140 µm thick Viresolve® filters were scanned from both sides to generate a confocal image through the full depth of the filter.

Further insights into nanoparticle capture were obtained by generating confocal images through a cross-section of the Viresolve® Pro filter. A 1 cm × 0.5 cm piece of filter was cut in cross-section using a cryostat microtome (Leica model CM1950) at -20 °C. The sample was mounted on the cryosectioning holder by adding Shandon™ Cryomatrix™ embedding resin (6769006, ThermoFisher Scientific). Thin (40 µm thick) sections were cut, transferred onto a glass slide, and immersed in DI water to remove the embedding medium. The sample was covered by a glass cover slip and imaged using the Olympus Fluoview™ confocal microscope.

2.3 Results and Discussion

2.3.1 FluoSpheres® Properties

Figure 2.1 shows the particle size distribution for the 20 (red and yellow-green), 40, and 100 nm fluorescent nanospheres as determined by dynamic light scattering. All 4 spheres were monodisperse, with no evidence of any nanoparticle aggregates (after ultrasonication for 5 min). The 20 nm red and yellow-green nanoparticles showed essentially identical results in the DLS, with mean particle diameters of 28 ± 10 and 26 ±

9 nm. The 40 and 100 nm FluoSpheres® had mean particle size of 43 ± 16 and 105 ± 27 nm, respectively.

The physical properties of the different nanoparticles are summarized in Table 2.1. The concentration, excitation / emission wavelengths, and charge (in mEq/g) were provided by the manufacturer, with the size and zeta potential determined by DLS and electrophoretic light scattering, respectively. All of the nanoparticles had a significant negative charge, consistent with the carboxylate groups used to stabilize the suspensions. The measured zeta potential for the red and yellow-green 20 nm nanoparticles were statistically identical. The measured zeta potential was somewhat greater for the larger particles, which likely reflects the different electrostatic potential around the larger spheres.

Table 2.1 Properties of fluorescently-labeled nanoparticles provided by manufacturer

Product Number	**Size (nm)**	**Stock Concentration (particles/mL)**	**Excitation/ Emission (nm)**	**Charge (mEq/g)**	**Zeta Potential (mV)**
F8787	26 ± 9	2.3×10^{15}	505/515	-0.64	-34 ± 9
F8786	28 ± 10	2.3×10^{15}	580/605	-0.64	-29 ± 13
F8789	43 ± 16	10×10^{14}	660/680	-0.65	-36 ± 13
F8801	105 ± 27	3.8×10^{13}	580/605	-0.39	-41 ± 21

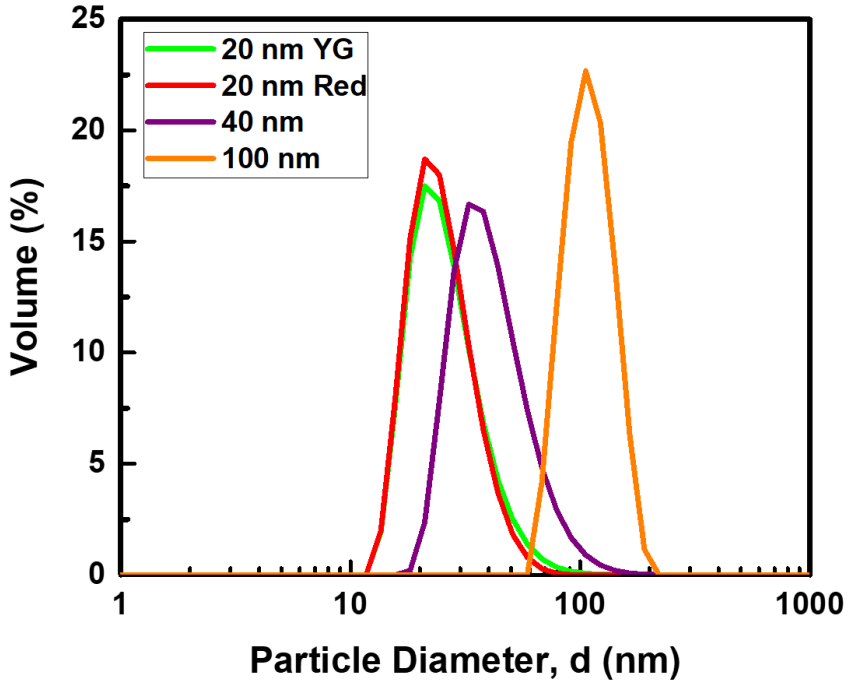

Figure 2.1 Size distribution for the fluorescent nanospheres.

2.3.2 FluoSpheres® as Model Virus

A suspension containing 10^{12} particles/mL of the yellow-green (20 nm) nanospheres was filtered through an Ultipor® DV20 filter oriented with the shiny-side down at a constant pressure of 210 kPa (30 psig), corresponding to a filtrate flux of 4.6 μm/s = 17 L/m^2/h. The flux remained constant throughout the filtration (variation of less than ±5%). There was no visible fluorescence in the collected permeate (after filtration of 9 L/m^2); this corresponds to at least 99.9% nanoparticle retention based on the detection limit of the fluorescence spectrophotometer. The left hand panel of Figure 2.2 shows a confocal image through the z-depth of the filter, obtained by stacking 80 x-y images, each approximately 0.5 μm in thickness. The 20 nm FluoSpheres® are easily visible in a diffuse

band, approximately 10 µm across, captured near the entrance to the 40 µm thick DV20 filter. The black region to the right (upstream) of the green band is primarily outside of the filter; the confocal microscope does not provide a direct way of quantitatively locating the upper surface of the filter. Some of the nanoparticles penetrated considerably deeper into the filter, reflecting the stochastic nature of particle capture. The confocal image in the right hand panel shows a separate DV20 membrane after filtration of 25 nm fluorescently-labeled PP7 bacteriophage [18]. The images look very similar, indicating that capture of the 20 nm FluoSpheres® is an appropriate model for PP7, which is commonly used as a model virus in studies of virus filtration.

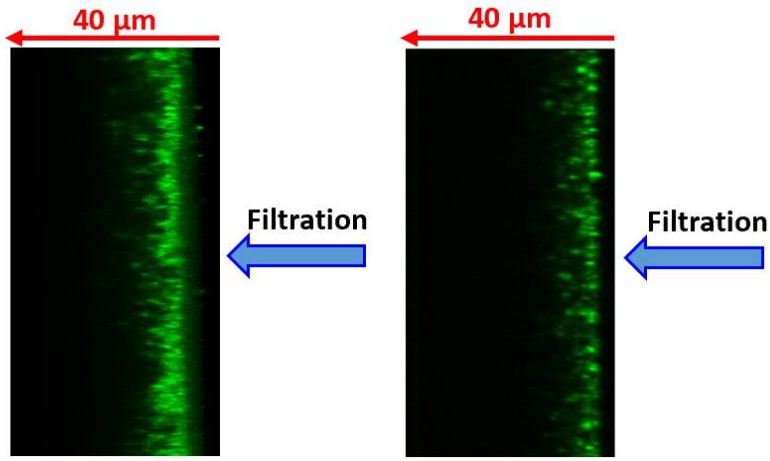

Figure 2.2 Confocal laser scanning microscopy images of Ultipor® DV20 membranes after filtration of suspensions of yellow-green 20 nm nanospheres (left panel) and fluorescently-labeled PP7 bacteriophage (right panel) at a constant pressure of 210 kPa. Right image taken from Bakhshayeshi et al. [18].

2.3.3 Ultipor® DV20 Membrane

Figure 2.3 shows confocal images of three DV20 membranes, each used to filter 9 L/m^2 of red 20 nm nanospheres (10^{12} particles/mL) followed by 9 L/m^2 of yellow-green 20 nm nanospheres (10^{12} particles/mL), with a process disruption (pressure release) for 1 min, 10 min, or 30 min between the two nanoparticle filtrations. Note that the yellow-green and red 20 nm nanospheres have nearly identical size and charge, differing only in their fluorescence. Again, the black region to the right of the fluorescence is located primarily outside of the filter. In each case, the confocal image shows two bands of captured nanoparticles, with the red nanoparticles (filtered before the pressure release) located deeper within the filter than the yellow-green nanoparticles (filtered after the pressure release). Similar results were reported by Dishari et al. [13] using bacteriophage with different fluorescent dyes. The separation between the bands increases slightly as the time for the process disruption increases, with relatively little overlap between the bands seen after the 30 min disruption. This behavior is consistent with the physical model presented by Woods and Zydney [20] in which the nanoparticles captured within the membrane during the initial filtration diffuse out of the pores during the pressure release and then migrate deeper into the pore structure when the pressure is reapplied. The increase in separation between the bands for the 30 min disruption would thus be associated with the greater diffusion time, which allows more of the originally captured nanoparticles to diffuse laterally within the filter to regions where they are able to migrate deeper into the filter during the subsequent filtration.

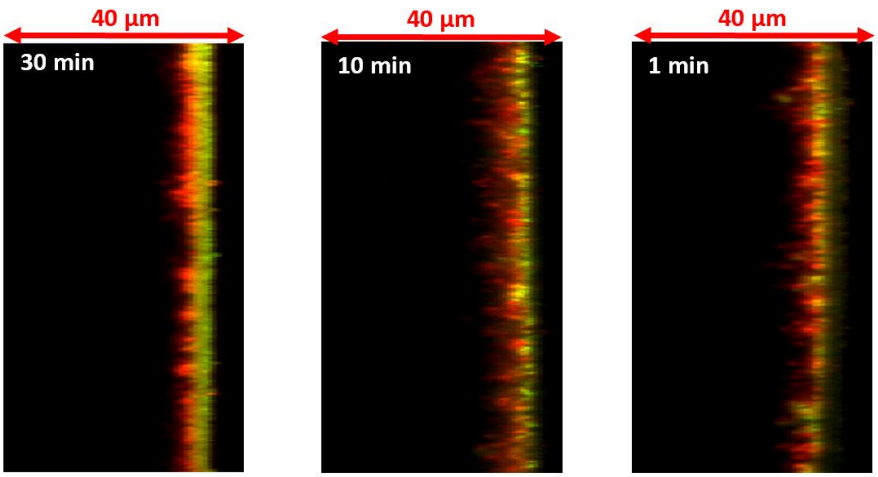

Figure 2.3 Confocal laser scanning microscopy images of three Ultipor® DV20 filters after filtering 20 nm red nanoparticles followed by 20 nm yellow-green nanoparticles at 210 kPa with a pressure release for 1 min, 10 min, or 30 min.

In order to probe the role of virus filter pore structure and morphology on virus capture in more detail, an Ultipor® DV20 membrane was challenged with a mixture containing the yellow-green 20 nm (10^{12} particles/mL), dark-red 40 nm (10^{11} particles/mL) (shown as purple in the image), and red 100 nm (10^{10} particles/mL) FluoSpheres® in a constant pressure filtration at 210 kPa (30 psig). Confocal images obtained after filtration of 27 L/m^2 of the mixture are shown in Figure 2.4. The right hand panel shows an overlay of the fluorescent scans at the different excitation and emission wavelengths, this overlay is done using the confocal software and did not involve any movement of the membrane sample or any manual alignment of the images. The far left hand panel shows an overlay of the cross-sectional images obtained for the 3 particles at a depth of approximately 14 µm measured into the filter beginning at the upper surface of the DV20 membrane. The small panels between these images are cross-sections through the 40 µm thick membrane

for the individual nanoparticles (fluorescence intensity evaluated after excitation with the appropriate wavelength laser). The yellow-green 20 nm nanospheres penetrate several microns deeper into the filter than either the 40 or 100 nm nanoparticles, consistent with a small asymmetry in pore size within the DV20 membrane (SEM image presented subsequently in Figure 2.6). This type of asymmetry has been observed previously in dextran sieving measurements obtained with flow in the normal and reverse orientations [21]. The 40 nm (purple) and 100 nm (red) nanoparticles appear to be captured at essentially the same location, spanning a depth of approximately 10 μm. This suggests that the pores at the entrance (upper surface) of the DV20 membrane rapidly decrease to a size that is sufficiently small to capture both the 40 and 100 nm nanoparticles, while allowing the 20 nm nanoparticles to penetrate somewhat further into the depth of the filter before being captured in the progressively smaller pores.

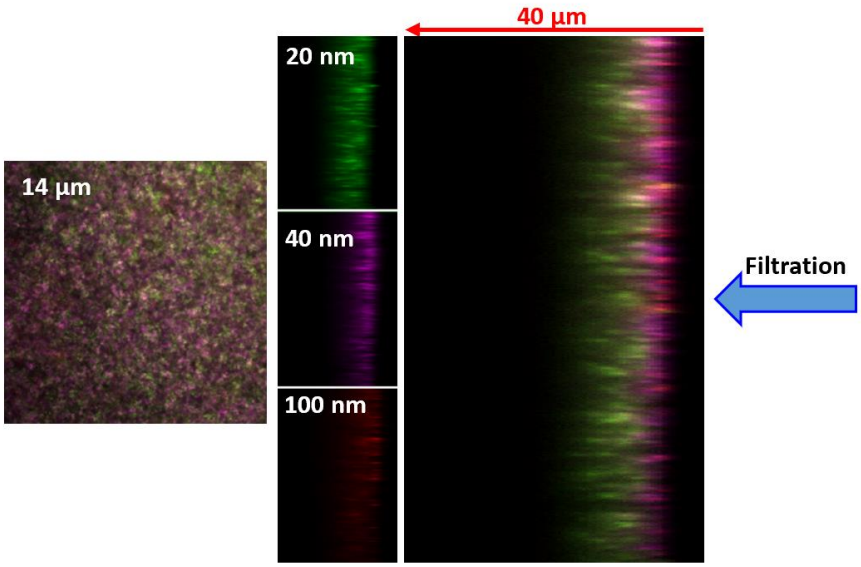

Figure 2.4 Confocal laser scanning microscopy images of the Ultipor® DV20 membrane after filtration of 27 L/m^2 of a suspension of 20 nm (green), 40 nm (purple), and 100 nm (red) FluoSpheres®. Middle images are for the individual FluoSpheres® using different excitation / emission wavelengths while right panel shows an overlay of these images through the depth of the filter. Left-most panel shows a cross-section through the filter located approximately 14 µm into the depth of the membrane.

2.3.4 Viresolve® Pro Membrane

Corresponding confocal images of the highly asymmetric Viresolve® Pro membrane after challenging with a mixture of the green (20 nm), purple (40 nm), and red (100 nm) FluoSpheres® are shown in Figure 2.5. The main panel shows a cross-sectional image through the entire depth of the 140 µm filter; this image was generated by a z-cut through a series of "slices" obtained from confocal images of the upper and lower half of the Viresolve® Pro membrane. The data were again obtained at a constant pressure of 210 kPa (30 psig), in this case corresponding to a constant filtrate flux of 61 µm/s = 220 L/m^2/h. There is a relatively narrow band of fluorescence near the filter entrance, approximately 12

μm in from the upstream surface of the filter, that contains all three FluoSpheres®. The nature of nanoparticle capture in this upper band is unclear; similar results have been reported using fluorescently-labeled bacteriophage [13]. There is then a much brighter and more diffuse band of nanoparticles well within the depth of the filter. The 20 nm (green) nanoparticles penetrated considerably deeper into the filter than either the 40 or 100 nm nanoparticles, which is consistent with the highly asymmetric structure of the Viresolve® Pro membrane (SEM image in Figure 2.6). Separate z-cut images of the FluoSpheres® in the lower half of the membrane (left-most panels) show that the 40 and 100 nm nanospheres were captured at approximately the same location, around 110-120 μm into the depth of the 140 μm filter (measured in from the upstream surface) while the brightest portion of the band corresponding to the green 20 nm nanospheres was located at a position 120-125 μm into the depth of the filter. This suggests that the pore size within the Viresolve® Pro membrane decreases rapidly from >200 nm in the membrane support structure (upper layer of the filter) to a size that is small enough to capture both the 40 and 100 nm nanoparticles before decreasing more gradually to a size that is less than 20 nm.

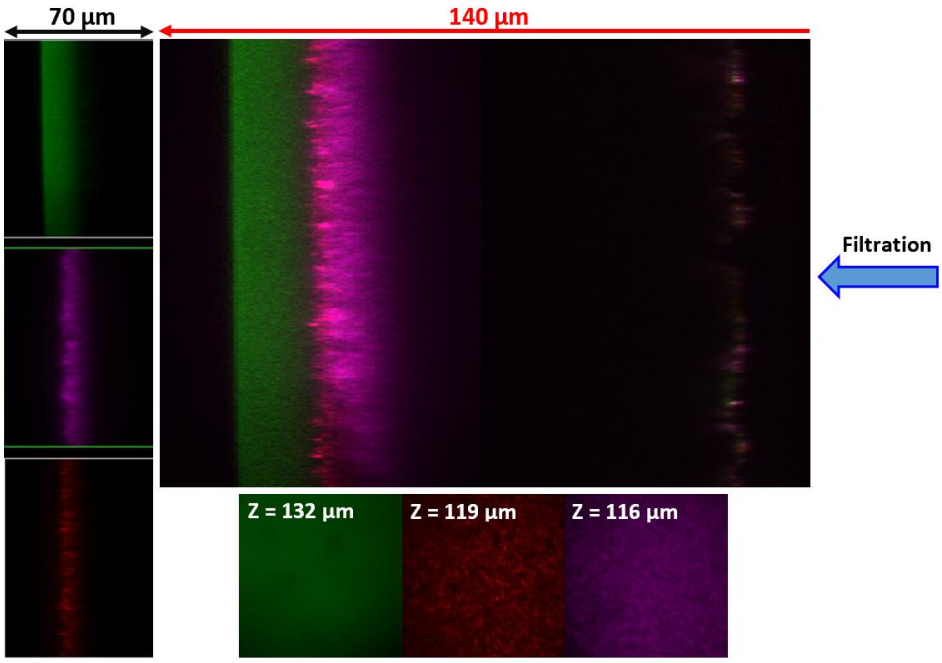

Figure 2.5 Confocal laser scanning microscopy images of the Viresolve® Pro membrane after filtration of 27 L/m^2 of a suspension of 20 nm (green), 40 nm (purple), and 100 nm (red) FluoSpheres® at a constant pressure of 210 kPa. Lower images show x-y planes at depths of 116, 119, and 132 µm measured in from the upper surface of the 140 µm thick membrane. Left images show separate z-cut images through the lower half of the membrane.

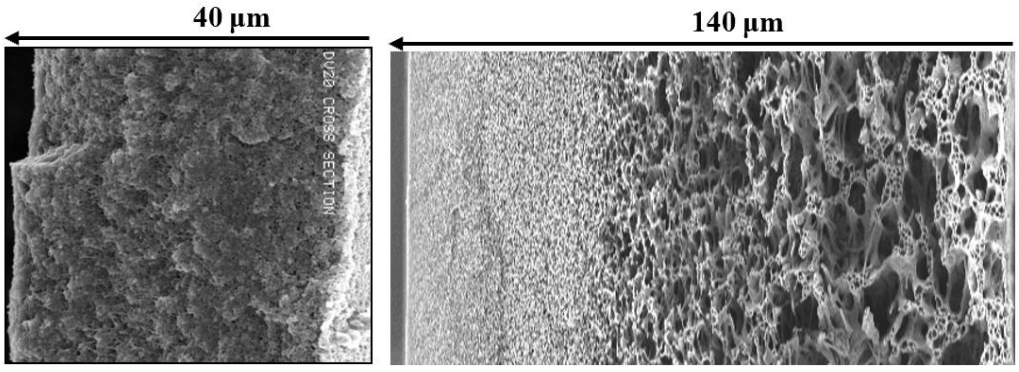

Figure 2.6 Scanning electron micrograph (SEM) of the cross-section of an Ultipor® DV20 membrane (left panel) and a Viresolve® Pro membrane (right panel). In both cases, filtration occurs from right to left.

Additional confocal images were obtained for a cross-sectional slice through the Viresolve® Pro membrane. This eliminates any artifacts arising from light scattering or absorption by the membrane material as one scans through the depth of the filter [22]. Figure 2.7 shows a confocal image of an x-y plane through a 40 μm thick slice of the Viresolve® Pro filter after a 36 L/m^2 challenge using a mixture of the yellow-green (20 nm), purple (40 nm), and red (100 nm) nanoparticles (analogous to the challenge in Figure 2.5). The different size nanoparticles were captured in several bands near the filter exit, with the yellow-green 20 nm particles captured in a diffuse band throughout much of the lower half of the filter including a sharp band right near the filter exit. The purple 40 nm particles were also captured in multiple bands, with the deepest band lying slightly upstream of the 20 nm particles. The red 100 nm particles were captured primarily in a thin band located further upstream of the 40 nm particles. Note that there was no evidence of any particles near the filter inlet as seen in Figure 2.5. The differences in the detailed capture profiles seen in Figure 2.7 (for a cross-section cut through the Viresolve® Pro) and Figure 2.5 (a z-cut obtained from a stack of confocal images obtained by optical scanning through the depth of the Viresolve® Pro) likely reflect the inherent variability in nanoparticle capture in different membrane samples in combination with the differences in membrane preparation (cryo-sectioning for Figure 2.7) and imaging (single x-y plane in Figure 2.7 versus a z-cut through a stack of x-y images in Figure 2.5).

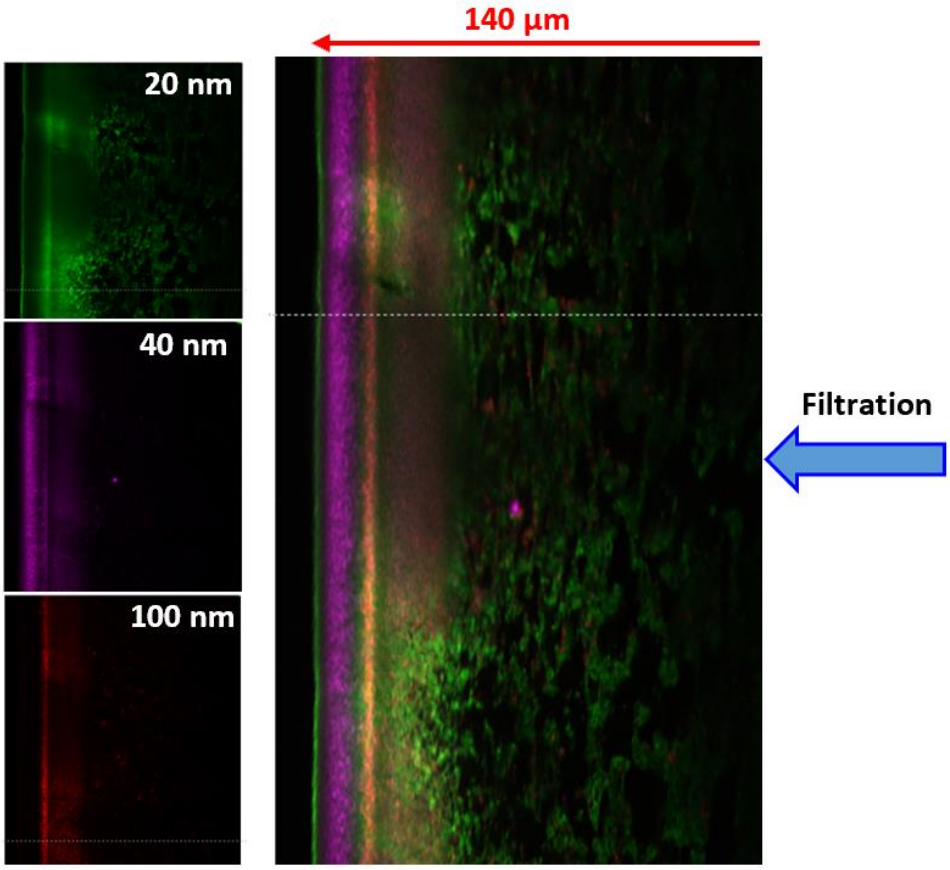

Figure 2.7 Confocal laser scanning microscopy cross-section image of a Viresolve® Pro filter after filtration of 36 L/m^2 of a suspension of 20 nm (green), 40 nm (purple), and 100 nm (red) FluoSpheres® at a constant pressure of 210 kPa. Left images show individual scans of captured nanoparticles within the entire depth of filter.

Figure 2.8 shows a confocal image of a separate Viresolve® Pro membrane used to filter 27 L/m^2 of the nanoparticle mixture but in the reverse orientation, i.e., with the tighter (skin-side) facing the feed. The filtration was again performed at 210 kPa, with no evidence of any flux decline during the course of the filtration. The different size nanoparticles are all captured in a single band at the upper surface of the membrane, i.e., right at the entrance to the tight skin of the Viresolve® Pro membrane. The low fluorescence intensity in these

images is due to the removal of loosely deposited nanoparticles from the external surface of the membrane during the rinsing of the filter prior to mounting on a glass slide. Some of these excess nanoparticles appear to have adsorbed onto the bottom surface of the filter, giving rise to the very faint band of fluorescence at the far left of the upper image. The cross-sectional images of the fluorescence intensity associated with the individual nanoparticles (lower panels) show a relatively uniform distribution of nanoparticles within the x-y plane, without any visible “hot spots” for nanoparticle capture.

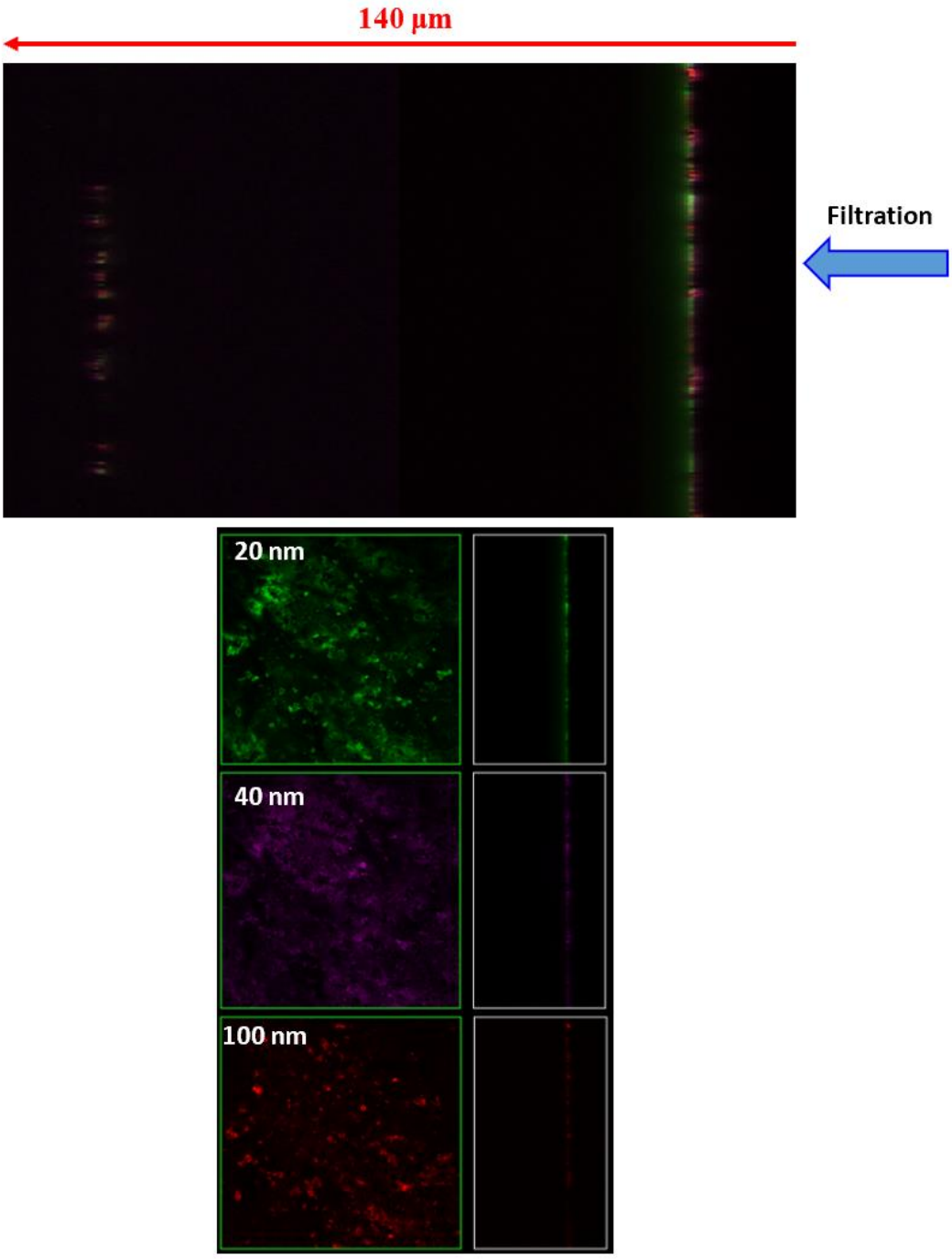

Figure 2.8 Confocal laser scanning microscopy images of the Viresolve® Pro membrane after filtration of 27 L/m^2 of a suspension of 20 nm (green), 40 nm (purple), and 100 nm (red) FluoSpheres® at constant pressure with the skin-side of the membrane facing the feed. Lower panels show cross-sectional images and x-y slices for the different size (color) nanoparticles.

Figure 2.9 shows confocal image of a Viresolve® Pro membrane after challenging with the 20 nm nanoparticles with a 10 min process disruption, following the same protocol as used previously in Figure 2.3. In contrast to the results with the Ultipor® DV20, the yellow-green 20 nm nanoparticles (in the feed after the process disruption) penetrated deeper within the filter than the 20 nm red nanoparticles (in the feed before the process disruption). This suggests that the nanoparticles that were captured before the process disruption remained trapped at the initial capture location, without any further migration into the filter. The nanoparticles that were filtered after the process disruption were captured deeper within the filter since the upstream capture sites were largely unavailable since they were "filled" with the red nanoparticles. The dramatic difference in capture behavior for the Viresolve® Pro and Ultipor® DV20 filters is likely related to the different pore morphology, and possibly surface chemistry, in these membranes.

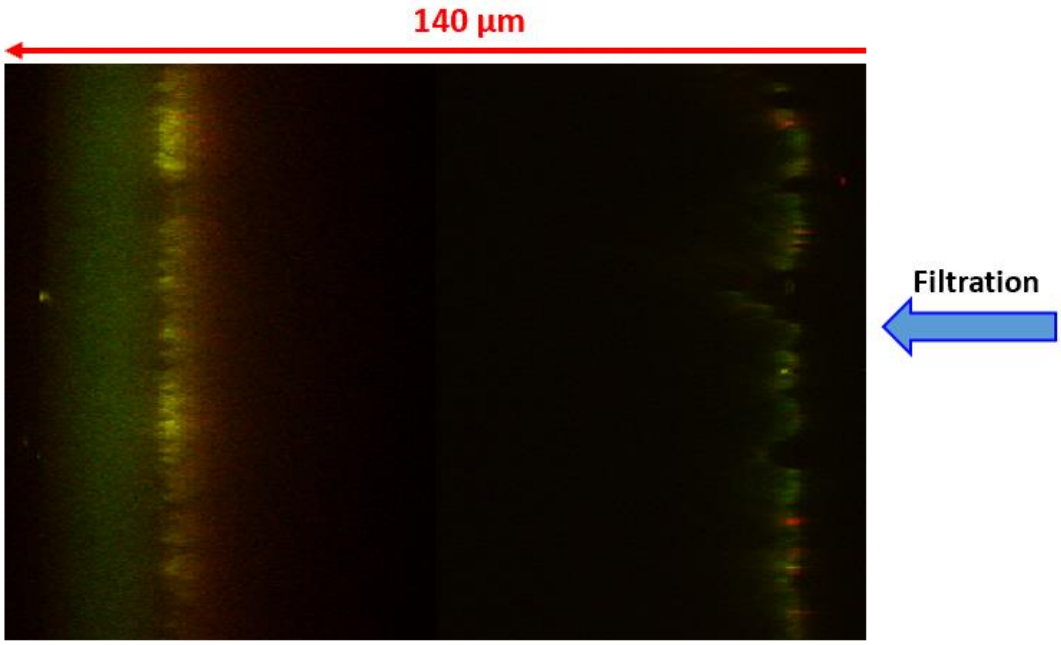

Figure 2.9 Confocal laser scanning microscopy image of a Viresolve® Pro filter after filtering 20 nm red nanoparticles followed by 20 nm yellow-green nanoparticles at a constant pressure of 210 kPa with a pressure release for 10 min.

2.4 Conclusions

The results presented in this Chapter clearly demonstrate the potential of using fluorescently-labeled nanoparticles with confocal laser scanning microcopy to directly visualize nanoparticle capture within commercially available virus filters. The 20 nm FluoSpheres® were captured in a band approximately 10 µm thick near the upstream surface of the Ultipor® DV20 membrane, in good agreement with confocal images obtained previously by Bakhshayeshi et al. using fluorescently-labeled PP7 bacteriophage [18]. Confocal images obtained after pressure release experiments using differently labeled nanoparticles before and after the process disruption show that the FluoSpheres® captured in the DV20 membrane before the pressure release migrate deeper into the filter after the

process disruption, consistent with results reported previously by Dishari et al. using labeled bacteriophage [13]. The gap between the two bands of nanoparticles increases with increasing time for the process disruption. Confocal images obtained with the Viresolve® Pro membrane were dramatically different, with the nanoparticles filtered after the process disruption penetrating deeper into the membrane (past the capture zone for the nanoparticles in the feed before the process disruption).

One of the unique advantages of using the fluorescently-labeled nanoparticles is that the FluoSpheres® are available in different sizes, each with its own fluorescent dye. Confocal microscopy can thus be used to simultaneously capture images of the different size nanoparticles, providing critical information on the variation in pore size and capture capabilities within the internal structure of the virus filter. Results obtained with the DV20 filter show that the different FluoSpheres® were all captured near the entrance of the filter, with the 20 nm nanoparticles penetrating slightly deeper into the membrane than the 40 and 100 nm nanoparticles, consistent with a slight asymmetry in the membrane pore size. The behavior of the Viresolve® Pro was considerably different. There was a relatively thin band of nanoparticles captured near the inlet of the filter in the macroporous substructure; the nature of particle capture in this region is unclear. Most of the nanoparticles are captured in the lower half of the filter, with the 20 nm nanoparticles penetrating significantly deeper into the filter. The 40 and 100 nm nanoparticles were captured at approximately the same location, approximately 110 μm into the depth of the 140 μm Viresolve® Pro filter, suggesting that the pore size decreases relatively rapidly from more than 200 nm in the macroporous support to less than 40 nm before decreasing more

gradually to around the 20 nm size needed to obtain the very high levels of virus removal required in virus filtration applications. Images obtained with the membrane oriented in the reverse orientation (skin-side up) show all of the nanoparticles captured in a thin band right at the entrance to the filter due to the small pore size at the lower surface of the Viresolve Pro® membrane. These results clearly demonstrate that confocal microscopy using fluorescently-labeled nanoparticles with different size (and also different surface chemistries) can be used to study the underlying pore structure and virus capture properties of virus filtration membranes.

2.5 Literature Cited

[1] H. Rabenau, V. Ohlinger, J. Anderson, B. Selb, J. Cinantl, W. Wolf, J. Frost, P. Mellor, H. Wilhelm Doerr, Contamination of genetically engineered CHO-cells by epizootic haemorrhagic disease virus (EHDV), Biologicals. 21 (1993) 207–214.

[2] G. Sofer, J. Carter, Viral Clearance: A Strategy for Quality by Design and the Design Space, in: A. Rathore, R. Mhatre (Eds.), Qual. by Des. Biopharm. Princ. Case Stud., John Wiley & Sons, Inc., Hoboken, NJ, USA, 2009: pp. 143–159.

[3] F. Hesse, R. Wagner, Developments and improvements in the manufacturing of human therapeutics with mammalian cell cultures, Trends Biotechnol. 18 (2000) 173–180.

[4] T. Ireland, H. Lutz, M. Siwak, G. Bolton, Viral filtration of plasma-derived human IgG, Pharm. Technol. Eur. 18 (2006) 43–49.

[5] K. Brorson, S. Krejci, K. Lee, E. Hamilton, K. Stein, Y. Xu, Bracketed generic inactivation of rodent retroviruses by low pH treatment for monoclonal antibodies and recombinant proteins, Biotechnol. Bioeng. 82 (2003) 321–329.

[6] B. Horowitz, M. Wiebe, A. Lippin, M. Stryker, Inactivation of viruses in labile blood derivatives. I. Disruption of lipid-enveloped viruses by tri(n-butyl)phosphate detergent combinations, Transfusion. 25 (1985) 516–522.

[7] P. Roberts, Virus safety in bio products, J. Chem. Technol. Biotechnol. 59 (1994) 110–111.

[8] M. Krishnan, G. Kern, Virus removal by filtration: Points to consider, BioPharm Int. 19 (2006).

[9] S. Curtis, K. Lee, G.S. Blank, K. Brorson, Y. Xu, Generic / matrix evaluation of SV40 clearance by anion exchange chromatography in flow-through mode, Biotechnol. Bioeng. 84 (2003) 179–186.

[10] S.R. Wickramasinghe S. Ranil, E.D. Stump, D.L. Grzenia, S.M. Husson, J. Pellegrino, Understanding virus filtration membrane performance, J. Memb. Sci. 365 (2010) 160–169.

[11] S.R. Wickramasinghe, Tangential-Flow Filtration for Virus Capture, in: N.N. Li, A.G. Fane, W.S.W. Ho, T. Matsuura (Eds.), Adv. Membr. Technol. Appl., John Wiley & Sons, Inc., Hoboken, NJ, USA, 2008.

[12] S. Lute, M. Bailey, J. Combs, M. Sukumar, K. Brorson, Phage passage after extended processing in small-virus-retentive filters, Biotechnol. Appl. Biochem. 47 (2007) 141–151.

[13] S.K. Dishari, A. Venkiteshwaran, A.L. Zydney, Probing effects of pressure release on virus capture during virus filtration using confocal microscopy, Biotechnol. Bioeng. 112 (2015) 2115–2122.

[14] G.R. Bolton, S. Spector, D. Lacasse, Increasing the capacity of parvovirus-retentive membranes: performance of the Viresolve™ Prefilter, Biotechnol. Appl. Biochem. 43 (2006) 55–63.

[15] N.B. Jackson, M. Bakhshayeshi, A.L. Zydney, A. Mehta, R. van Reis, R. Kuriyel, Internal virus polarization model for virus retention by the Ultipor® VF Grade DV20 membrane, Biotechnol. Prog. 30 (2014) 856–863.

[16] D. Lacasse, P. Genest, K. Pizzelli, P. Greenhalgh, L. Mullin, A. Slocum, Impact of process interruption on virus retention of small-virus filters, Bioprocess Int. 11 (2013) 32–44.

[17] S.K. Dishari, M.R. Micklin, K.J. Sung, A.L. Zydney, A. Venkiteshwaran, J.N. Earley, Effects of solution conditions on virus retention by the Viresolve® NFP filter, Biotechnol. Prog. 31 (2015) 1280–1286.

[18] M. Bakhshayeshi, N. Jackson, R. Kuriyel, A. Mehta, R. van Reis, A.L. Zydney, Use of confocal scanning laser microscopy to study virus retention during virus filtration, J. Memb. Sci. 379 (2011) 260–267.

[19] F.W. Pontius, G.L. Amy, M.T. Hernandez, Fluorescent microspheres as virion surrogates in low-pressure membrane studies, J. Membr. Sci. J. 335 (2009) 43–50.

[20] M.A. Woods, A.L. Zydney, Effects of a pressure release on virus retention with the Ultipor DV20 membrane, Biotechnol. Bioeng. 111 (2014) 545–551.

[21] M. Bakhshayeshi, A.L. Zydney, Effect of solution pH on protein transmission and membrane capacity during virus filtration, Biotechnol. Bioeng. 100 (2008) 108–117.

[22] M. Marroquin, T. Bruce, J. Pellegrino, S.R. Wickramasinghe, S.M. Husson, Characterization of asymmetry in microporous membranes by cross-sectional confocal laser scanning microscopy, J. Memb. Sci. 379 (2011) 504–515.

Chapter 3
Probing Pore Structure of Virus Filters Using Scanning Electron Microscopy with Gold Nanoparticles

The work presented in this Chapter is based on the material published in: Nazem-Bokaee, H. F. Fallahianbijan, D. Chen, S.M. O'Donnell, C. Carbrello, S. Giglia, D. Bell, A.L. Zydney, "Probing pore structure of virus filters using scanning electron microscopy with gold nanoparticles," J. Membrane Sci., 552: 144-152 (2018). The author would like to acknowledge the work by Hadi Nazem-Bokaee on the characterization of the hollow fiber membranes.

3.1 Introduction

Virus filtration membranes are used to remove viruses in both bioprocessing [1-3] and water treatment [4, 5]. In bioprocessing applications, virus filters are designed to remove at least 99.9% of the smallest parvovirus (around 20 nm in size) while providing nearly complete transmission of the therapeutic product, e.g., a monoclonal antibody, which is approximately 8 nm in size. This requires very careful design and control of the membrane pore size and morphology to obtain the desired selectivity while also achieving high capacity (large volumetric throughput before fouling).

A number of different approaches have been used to obtain insights into the pore size / morphology of virus filters. Giglia et al. [6] used liquid-liquid displacement porosimetry with mixtures of polyethylene glycol and ammonium sulfate (referred to as CorrTest wetting and intrusion fluids) to evaluate the pore size distribution of a series of co-cast polyethersulfone virus filtration membranes. The calculated values of the pore size distribution were in good agreement with the measured retention of different size bacteriophages (PR772 and ΦX-174) and model mammalian viruses (MVM - minute virus

of mice and PPV – porcine parvovirus). Similar results were obtained by Peinador et al. [7] using isobutanol and water for the liquid-liquid displacement tests and PP7 bacteriophage as a model virus. Calvo et al. [8] found that data for dextran retention coefficients provided similar results to liquid-liquid porosimetry, although neither approach was able to provide accurate information on the tail end of the pore size distribution, which is likely to be critical for achieving very high levels of virus retention. In addition, liquid-liquid porosimetry and dextran retention measurements provide no information on the location of the most selective pores within the depth of the examined virus filtration membranes.

Bakhshayeshi et al. [9] used confocal laser scanning microscopy with fluorescently-labeled bacteriophages (PP7 and MS2) to identify the location of virus capture within flat-sheet virus filters. The results clearly show the highly asymmetric structure of the Viresolve® Pro membrane, with virus capture occurring very close to the filter exit. In contrast, the selective pores within the Ultipor® DV20 membrane were located several microns into the depth of this membrane, which possesses a relatively more symmetric (homogeneous) structure. The work described in Chapter 2 of this thesis, and presented in Fallahianbijan et al. [10], used different size nanoparticles, each with different fluorescent dyes. Confocal images of the captured nanoparticles in the Viresolve® Pro membrane provided a clear picture of the asymmetric structure of the membrane, with the pore size decreasing from 100 to 20 nm over approximately a 10 – 20 μm region near the exit of the filter. However, confocal microscopy has a resolution of only ≈500 nm, making it impossible to detect the capture location of individual viruses / nanoparticles.

Marquez-Rocha et al. [11] used scanning electron microscopy (SEM) and Energy Dispersive X-ray Spectroscopy to study the pore size of a polyethersulfone ultrafiltration membrane. SEM images of the upper and lower surfaces clearly demonstrated the asymmetric character of these ultrafiltration membranes, but it was not possible to determine the actual pore size of the tight "skin" from the SEM images. Calvo et al. [12] used Field Emission Scanning Electron Microscopy (FESEM) to evaluate the pore size distribution of polysulfone ultrafiltration membranes. Image analysis yielded a much broader pore size distribution than determined from liquid-liquid porosimetry measurements, which the authors attributed to the difficulty in evaluating the very small pores and "the confusion between actual pore entrances and simply darker areas of polymeric surface." In addition, FESEM images of the intact membrane only provide information for the pores on the external surface of the membrane, which may or may not be the critical pores for virus retention.

A number of studies have used gold nanoparticles to evaluate the pore size and retention characteristics of virus filtration membranes. Sekine et al. [13] described the use of gold nanoparticle retention as an integrity test for Planova^{TM} hollow fiber virus filtration membranes. Tsurumi et al. [14, 15] were able to image captured gold nanoparticles within frozen fractured sections of a regenerated cellulose hollow fiber (BMM) virus filtration membrane. The nanoparticles were visible throughout the wall of the hollow fiber, with the greatest capture of 30 nm particles occurring approximately 10 μm into the filter as measured from the inner (lumen) surface of the fiber. A subsequent study showed that even gold nanoparticles as large as 100 nm were present through the depth of the pore structure

of this filter. However, the resolution of the SEM images was insufficient to identify the location of individual nanoparticles.

More recently, Kosiol et al. [16] examined the filtration of different size gold nanoparticles through a series of virus filtration membranes from different manufacturers. Optical micrographs of the tested membrane showed that 20 nm particles were captured primarily close to the feed-facing side of the membrane in the absence of sodium dodecyl sulfate (SDS), but the particles were observed deeper in the membrane upon the addition of SDS to the feed. This difference in behavior was attributed to the reduction in nanoparticle adsorption in the presence of SDS. Data for the retention of different size nanoparticles in the presence of SDS were used to evaluate the membrane pore size distribution, but the results provide no information on the nature of the membrane asymmetry, and the resolution of the optical microscopy was on the order of a micron (50 times the size of the nanoparticles). In their most recent work, Kosiol et al. [17] examined the capture of gold nanoparticles using SEM, with the membranes prepared by freeze-fracture with liquid nitrogen following procedures that were similar to those used in this Chapter. However, SEM images were shown for only a single membrane (manufacturer not identified) using very small 7.5 nm gold particles (well below the typical pore size of the virus filter), and the high nanoparticle loading used in these experiments made it difficult to identify individual particles. In addition, the use of gold nanoparticles in the presence of SDS could significantly alter the surface properties of both the nanoparticles and the membranes, potentially leading to artifacts in the observed capture behavior.

The objective of the work described in this Chapter was to develop a new methodology for evaluating the internal pore size / structure of different virus filtration membranes by direct visualization of different size gold nanoparticles (captured within the membrane during filtration) using scanning electron microscopy. SEM images were obtained using both hollow fiber (Planova™ 20N and BioEX) and flat sheet (Viresolve® Pro and Ultipor® DV20) membranes. The results provide important insights into the pore size / morphology and virus capture properties of different commercial virus filters.

3.2 Experimental

3.2.1 Gold Nanoparticles

Gold nanoparticles were purchased from Sigma-Aldrich (St. Louis, MO) as stabilized suspensions in citrate buffer (Table 3 1). The nanoparticle size was determined by Dynamic Light Scattering (DLS) measurements performed using a Zetasizer Nano ZS (Malvern Instruments Ltd, Worcestershire, UK). Nanoparticle suspensions were prepared by diluting the stock solutions with DI water obtained from a Direct-Q® 3 UV Water Purification System (MilliporeSigma, Billerica, MA) with resistivity greater than 18 MΩ.cm.

Table 3.1 Properties of gold nanoparticles used in this study

Product Number	Size (nm)	Stock Concentration (particles/mL)
741965	25±8	6.5×10^{11}
741981	42±12	7.2×10^{10}
742031	100±30	3.8×10^{9}

3.2.2 Virus Filters

Nanoparticle capture was examined using four different virus filters (Table 3.2): Planova™ 20N and Planova™ BioEX hollow-fiber virus filters from Asahi Kasei Medical Co., Ltd (Tokyo, Japan), highly asymmetric flat sheet Viresolve® Pro membrane filters from MilliporeSigma (Bedford, MA), and relatively homogeneous flat sheet Ultipor® DV20 filters from Pall Corp. (Port Washington, NY). These membranes were cast from different polymers (cellulose, polyethersulfone, and polyvinylidene fluoride) and with different morphologies as summarized in Table 3.2. The flat sheet membranes were cut into 47 mm disks and used in single layer format to facilitate observation by electron microscopy; the commercial flat sheet filters employ multi-layer membranes to obtain the high levels of virus removal needed in bioprocessing applications. The hollow fiber membranes were provided in cartridges containing 12 parallel fibers.

3.2.3 Gold Nanoparticle Filtration

Filtration experiments were performed at constant pressures of 70 and 210 kPa (10 and 30 psig) maintained by nitrogen pressurization of a feed reservoir filled with the nanoparticle suspension. Hollow fiber membranes were used in 0.001 m^2 modules oriented vertically as per the manufacturer's recommendations. Flat sheet membranes were used as 47 mm disks placed in a stainless steel filter holder (MilliporeSigma, Bedford, MA) with the skin-side away from feed (unless noted otherwise). Filters were initially flushed with at least 50 L/m^2 of DI water to ensure proper wetting and to eliminate any air bubbles. At the end of the filtration, the hollow fiber cartridge was cut open using a BrassCraft rotary tube cutter. Individual fibers were removed using a tweezer for examination by SEM.

Table 3.2. Summary of different virus filters examined in this study

Membrane	Material	Geometry	Asymmetry	Manufacturer
Planova™ BioEX	PVDF†	Hollow Fiber	Partially Asymmetric	Asahi Kasei
Planova™ 20N	Regenerated Cellulose	Hollow Fiber	Relatively Symmetric	Asahi Kasei
Viresolve® Pro membrane	Polyether-sulfone	Flat Sheet	Highly Asymmetric	MilliporeSigma
Ultipor® DV20	PVDF†	Flat Sheet	Symmetric	Pall

† Polyvinylidene difluoride

3.2.4 Membrane Preparation for SEM

Membranes were prepared using either a Leica EM UC6 Ultramicrotome or a Leica CM1950 Cryostat (Leica Biosystems Inc., Buffalo Grove, IL). For ultra-microtomy, small lengths of individual hollow fibers (~5 mm) or rectangles of the flat sheet membranes (10 × 3 mm) were cut using a scissor and dehydrated using progressively more concentrated ethanol solutions, beginning with 50% ethanol in water followed by 70%, 90%, and then 100% ethanol. The samples were then infiltrated with a 1:1 ratio (v/v) of 100% ethanol and LR white medium grade embedding resin (Electron Microscopy Sciences, Hartfield, PA) for a minimum of one hour at room temperature. The resin-ethanol mixture was replaced with 100% LR white resin (twice) and the sample incubated for an additional hour, with the membranes then transferred to a clean snap-fit gelatin capsule (Ted Pella. Inc., Rodding, CA), which was filled with fresh 100% LR white resin. The resin was cured by placing the capsule in an oven at 65˚C for 24-48 hours. The capsules were allowed to cool to room temperature, the cap and hardened LR white resin were trimmed using a metal razor, and the samples were then placed in the ultramicrotome holder and sectioned using a custom-made glass knife at a cutting speed of 200 µm/s for the hollow fibers and 1 mm/s for the flat sheet membranes. The thin slices (0.5 to 1 µm thick) were collected in a water-containing boat attached to the glass knife by nail polish and then transferred to a cover slip using a custom-made metal loop.

For cryo-sectioning, the small pieces of membrane were placed in a disposable vinyl Tissue-Tek® Cryomold (Sakura Finetek USA Inc., Torrance, CA) pre-filled with Shandon™ Cryomatrix™ embedding resin (Thermo Scientific, Kalamazoo, MI). The mold

was kept inside a Leica CM1950 Cryostat Microtome (Leica Biosystems Inc., Buffalo Grove, IL) at -20˚C until the resin became fully frozen. The membranes were then removed from the mold and mounted on top of a specimen holder disc that had been pre-filled with partially frozen Cryomatrix™ solution. Samples were cut into 10-15 µm thick sections using a MB35 Premier Microtome Blade (34˚/80mm, Thermo Scientific, Kalamazoo, MI) and placed on a glass coverslip pre-cleaned with ethanol and dust remover. Samples were gently washed with DI water to remove excess melted Cryomatrix™ solution and then heated slowly on a heater plate to evaporate any remaining water.

All samples were coated with a thin layer of iridium using an Emitech K575X sputter coater (Quorum Technologies Ltd, UK) to prevent charging from the membrane material; this also increased the secondary electron emission and enhanced contrast in the SEM.

3.2.5 Variable Pressure Field-Emission Scanning Electron Microscopy (VP-FESEM)

High resolution images of the membrane cross-section were obtained using a Zeiss Sigma VP-FESEM (Carl Zeiss Microscopy, Thornwood, NY, US). A retractable five-diode backscattered detector with accelerating voltage between 8 to 20 kV and 30 µm aperture was used; this provided high contrast between the gold nanoparticles and the sputter-coated polymer membrane. The microscope was also equipped with Energy Dispersive X-ray Spectrometry (EDS), which was used to obtain local elemental analysis of the samples.

3.2.6 Euclidian Distance Mapping

An independent estimate of the pore size of the Viresolve® Pro membrane was obtained by Euclidian distance mapping of a freeze fractured membrane. A high resolution (4096×3536 pixels) image was obtained by SEM and converted to a binary image map using standardized image analysis, rendering the pore area as white and the polymer as black. The binary image was then subdivided into smaller image strips at different positions through the thickness of the cross section. Each binary strip was then used to create a "skeleton image", representing the mid-line of each binary feature, and a Euclidean Distance Map (EDM), with the latter created by assigning each pixel a gray level equivalent to its distance from the feature's edge. The edge was assigned a gray level of zero, with the next pixel a gray level of one, and so on until the center of the feature is reached. The two images were mathematically combined using a logical AND operation, resulting in a Skeletonized Distance Map (SDM). The SDM represents the actual radii measurements in pixels of each feature within the image. This gray level data was exported to Excel and used to evaluate the pore size as a function of the pixel distance. The process was repeated for each binary strip to construct a plot of the mean pore radius versus the cross sectional position in the membrane.

3.3 Results and Discussion

3.3.1 SEM Analysis

In order to verify that the gold nanoparticles were monodisperse, samples of the 20, 40, and 100 nm particles were analyzed by dynamic light scattering, with typical results shown in Figure 3.1. In each case, the samples showed only a single peak, with mean size of 25 ± 8 nm, 42 ± 12 nm, and 100 ± 30 nm. The size distributions for the 20 and 40 nm gold nanoparticles showed considerable overlap; thus, the membranes were challenged with suspensions of either the individual nanoparticles or of the 100 nm nanoparticles in a mixture with either the 20 or 40 nm nanoparticles.

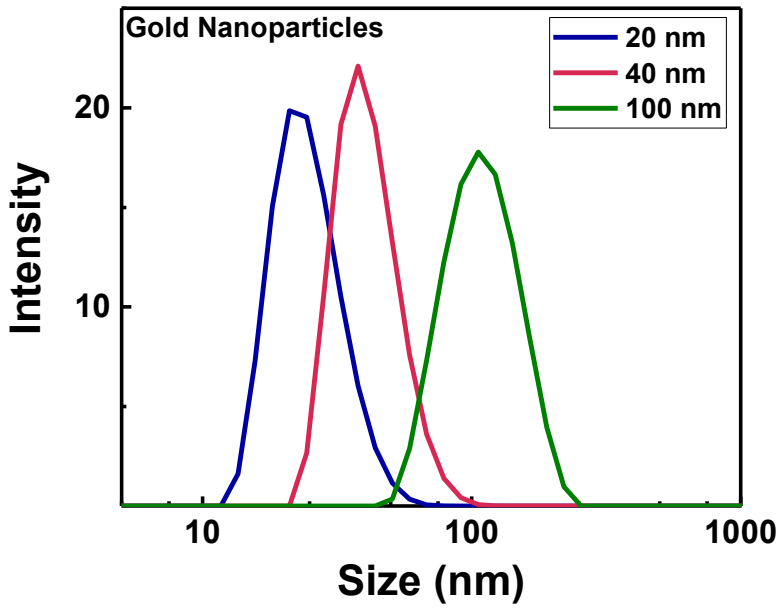

Figure 3.1 Dynamic Light Scattering (DLS) analysis of gold nanoparticle suspensions

Figure 3.2 shows an SEM image (left panel) along with the corresponding Energy Dispersive X-ray Spectrometry image (right panel) of a Planova™ BioEX membrane challenged with a suspension of 100 nm gold particles at a concentration of 4×10^8 nanoparticles per mL (corresponding to a particle volume fraction of approximately 2×10^{-10}). The filtration was performed at a constant pressure of 210 kPa (30 psig) for 60 min, giving an average filtrate flux of 20 µm/s (71 L/m^2/h) over a volumetric throughput of 60 L/m^2. There was no evidence of any flux decline during the filtration (variation in flux of <5%), and there were no detectable gold nanoparticles in the collected permeate. At the end of the filtration, single hollow fibers were removed from the cartridge, cryo-sectioned, and sputter-coated with iridium. The SEM images clearly show the capture of a large number of the 100 nm gold particles at the entrance to the filter, consistent with the high degree of exclusion of these relatively large nanoparticles from the pore structure of the BioEX membrane. However, individual nanoparticles are also observed well within the membrane pore structure; this is discussed in more detail in the following sections.

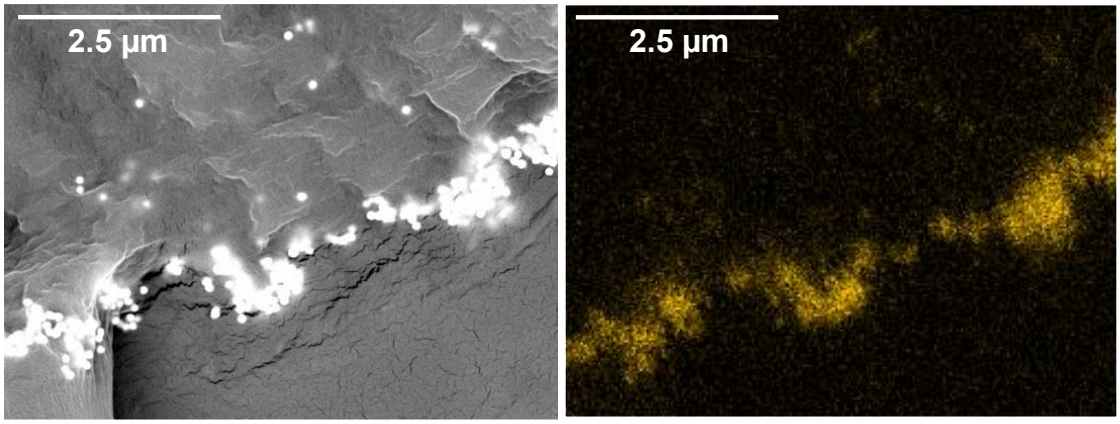

Figure 3.2 SEM (left) and EDS (right) images of the entrance region to the Planova™ BioEX membrane after challenging with 100 nm gold nanoparticles (28,500X magnification). Fiber lumen is to the lower right, with filtration occurring from the pressurized lumen.

3.3.2 Planova™ BioEX

Figure 3.3 shows a high-contrast image of a Planova™ BioEX fiber after challenging with a mixture of 100 nm (4×10^8 nanoparticles / mL) and 20 nm (6×10^{10} nanoparticles / mL) gold nanoparticles. The 100 nm nanoparticles are captured primarily in the upper 5 µm region near the inlet (lumen-side) of the fiber, although a small number of nanoparticles are observed much deeper into the membrane. In contrast, the 20 nm nanoparticles are captured further into the filter, with the majority of particles located within a region around 5 to 15 µm into the depth of the filter. We were unable to detect any nanoparticles in the permeate for any of our experimental runs, suggesting that the large majority (well above 99%) of the particles were captured within the filters. This behavior is consistent with the high retention of 20 nm viruses reported in the literature for all of the filters that were examined. The percent captured in Figure 3.4 were not the percent based on the feed but are instead the fraction of the total number of countable particles within each region of the filter.

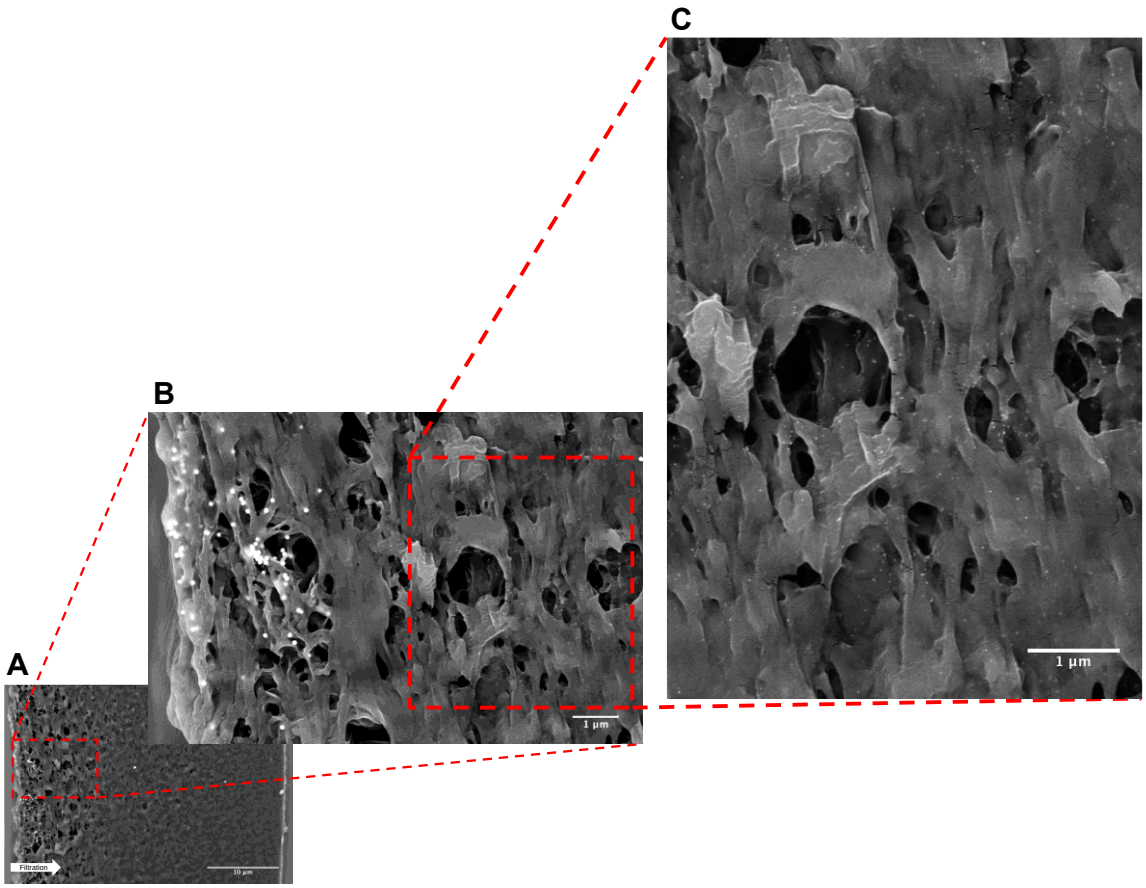

Figure 3.3 High-contrast SEM image of a PlanovaTM BioEX fiber (A) challenged with a mixture of 100 nm and 20 nm particles. Sub-images at higher magnification show: (B) 100 nm particles and (C) 20 nm particles.

Further quantification of the distribution of gold nanoparticles within the depth of Planova^{TM} BioEX filters were obtained by counting the number of nanoparticles in "slices" that were approximately 7 µm across and 35 µm deep (extending through the entire cross-section of the hollow fiber membrane) using ImageJ software. Results obtained at 3 separate locations within a single fiber are shown in Figure 3.4. A total of 3357 nanoparticles were counted; 210 of the 100 nm and 3147 of the 20 nm nanoparticles; the much larger number of 20 nm nanoparticles is consistent with the different particle

concentrations in the feed. The large majority (approximately 90%) of the 100 nm nanoparticles were detected within the first five microns of the filter (measured in from the lumen surface). However, a small number of 100 nm nanoparticles were observed at multiple locations within the depth of the filter, with 7 nanoparticles (3%) located in a band that was only several microns in from the outer surface of the hollow fiber. In contrast, less than 20% of the 20 nm gold nanoparticles were caught within the first five microns of the filter, with the large majority of these smaller particles (greater than 65%) positioned in a band lying between 5 and 15 μm as measured from the inner (lumen) side of the filter. The significant variability in the capture profiles at the different locations is indicative of the distribution in pore size and the highly stochastic nature of nanoparticle capture within the BioEX filter. Similar variability was seen in SEM images of separate fibers obtained from either a single or multiple filter cartridges, although the general profiles were comparable to those shown in Figures 3.3 and 3.4. Using larger sample size did not affect the key conclusions regarding the distribution or location of gold nanoparticles captured, although more than three fibers and three locations on each fiber of Planova filters were analyzed.

3.3.3 Planova^{TM} 20N

Corresponding SEM images for the Planova^{TM} 20N after filtration of a mixture of 100 and 20 nm gold nanoparticles are shown in Figure 3.5. In this case, the filtration was performed at a transmembrane pressure of 70 kPa (10 psig) as per the manufacturer's recommendation, giving a nearly constant filtrate flux of 12 μm/s (43 L/m^2/h). The

filtration was continued until a cumulative filtrate volume of 60 L/m^2 for direct comparison of the results with those obtained using the Planova^{TM} BioEx.

The 100 nm particles are easily visible (Figure 3.5) near the filter inlet (lumen side of the hollow fiber membrane). The majority of the 20 nm nanoparticles are captured within a band that is approximately 2-3 μm thick and located just beyond the capture region for the 100 nm particles. However, isolated particles of both sizes are observed throughout the depth of the membrane. The distribution of captured nanoparticles, determined using the ImageJ software, across the thickness of the Planova^{TM} 20N filter (total thickness of approximately 20 μm) is shown in the middle panel of Figure 3.4. More than one-half of the 100 nm nanoparticles are captured within the first 5 μm of the membrane, with most of the remaining 100 nm particles captured over the next 5 μm. In contrast, the 20 nm nanoparticles are captured throughout the depth of the filter, with more than 5% captured in the outer 5 μm region and nearly 10% captured in the outer half (10 μm) of the fiber.

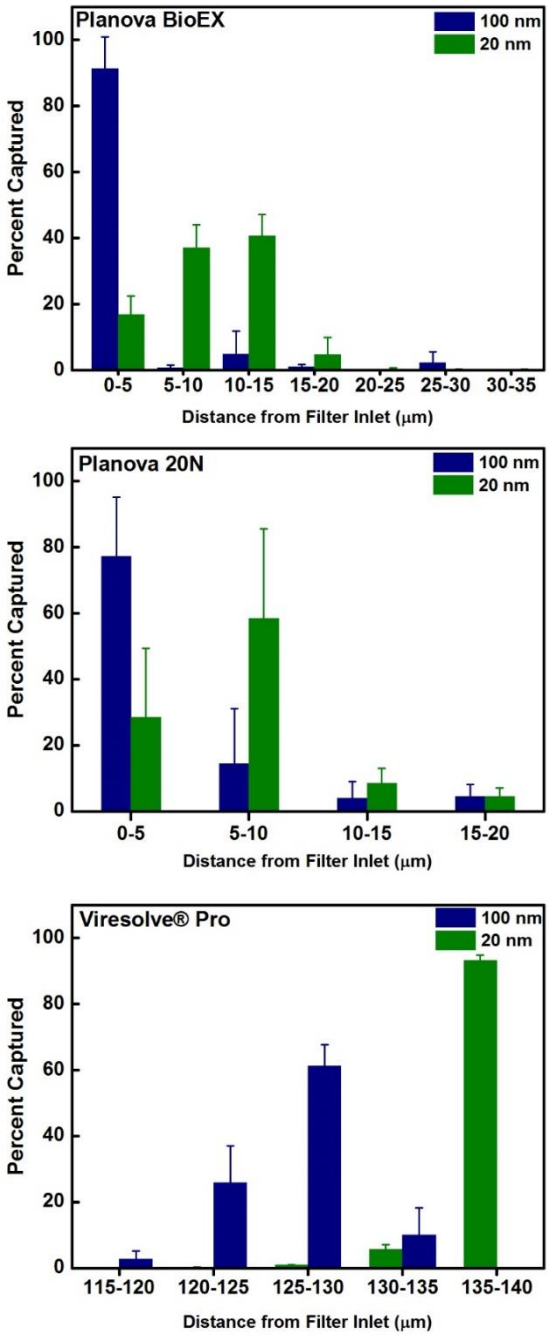

Figure 3.4 Distribution of gold nanoparticles within the depth of the Planova™ BioEX, Planova™ 20N, and Viresolve® Pro membrane filters after challenging with a mixture of 20 and 100 nm gold nanoparticles. Percent captured is evaluated as the ratio of the number of countable gold nanoparticles (visible by SEM) over a given region of the filter divided by the total number of counted nanoparticles across the full thickness of the filter.

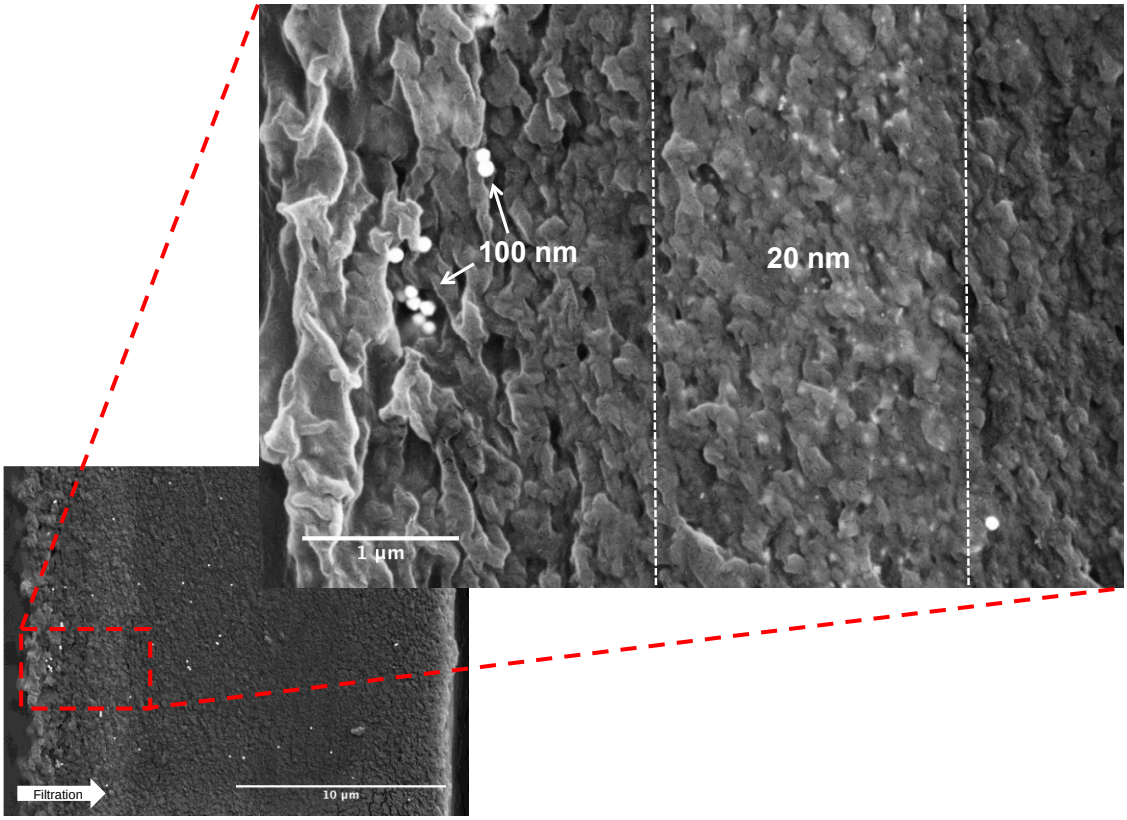

Figure 3.5 High-contrast SEM image of a Planova™ 20N fiber challenged with a mixture of 20 and 100 nm gold nanoparticles.

3.3.4 Viresolve® Pro

In contrast to the Planova™ filters, the Viresolve® Pro membrane is a highly asymmetric flat sheet membrane approximately 140 µm thick; it is used commercially as a two-layer structure to achieve very high levels of virus removal. Filtration experiments were performed with single-layers of the Viresolve® Pro membrane membrane, using mixtures of the 40 and 100 nm gold nanoparticles or 20 and 100 nm nanoparticles, with the SEM images shown in Figure 3.6. In both cases, the filtration was performed at a constant pressure of 210 kPa (30 psig) with the membrane oriented with the skin side facing

away from the feed as per the manufacturer's recommendation. This gave an essentially constant filtrate flux of 65 μm/s (230 L/m^2/h) over a volumetric throughput of 24 L/m^2. The low filtrate flux (compared to the expected value of 1000 L/m^2/h at this pressure) was due to pore blockage associated with the screen in the stainless steel holder; this is discussed in more detail in Chapter 5 of this thesis. Experiments performed with a spacer element beneath the membrane gave filtrate flux of 1000 ± 200 L/m^2/h with comparable SEM images.

The upper region of the membrane showed very few (if any) nanoparticles (Figures 3.6A and 3.6B). Thus, the nanoparticles were transported through most of the depth of the filter, depositing in the final 20 μm region near the filter exit, i.e., in the region just upstream of the selective skin layer of the membrane. The large majority of the 20 nm gold nanoparticles were captured in a narrow band that was approximately 600 nm thick and located only 500 - 1000 nm upstream of the filter exit (Figure 3.6C). The 40 and 100 nm gold nanoparticles were captured somewhat further "upstream" within the filter, with the mid-point of the 40 nm band lying approximately 5 μm in from the filter exit while the 100 nm nanoparticles were located approximately 15 μm in from the skin (Figures 3.6A and 3.6B). Qualitatively similar capture profiles were observed using fluorescently-labeled nanoparticles as discussed in Chapter 2, although it was difficult to identify the actual location of the particle bands due to light scattering / absorption and the challenges in accurately locating the exit of the filter in the confocal (optical) microscope.

The images shown in Figure 3.6 are consistent with the known asymmetric structure of the Viresolve® Pro membrane, with the capture profile suggesting that the membrane

pore size declines from around 100 to <20 nm over a 20-25 μm thick region just upstream of the tight skin layer. The pore size / gradient estimates based on the gold nanoparticle capture profiles were compared with results from the Euclidian Distance Mapping performed using an SEM image of a separate sample of the Viresolve® Pro membrane (Figure 3.7). The estimated pore size at the exit of the filter is just below 20 nm, consistent with the high degree of parvovirus retention for the Viresolve® Pro membrane. The pore size increases smoothly with distance as one moves into the depth of the membrane (above the skin), with the pore size approaching a value of 40 nm approximately 4 μm in from the skin layer and 100 nm approximately 20 μm into the membrane. These values are in excellent agreement with results from the SEM images in Figure 3.6.

Detailed analysis of the distribution of gold nanoparticles across the depth of Viresolve® Pro membrane are shown in the lower panel of Figure 3.4 (total of 2608 gold nanoparticles examined, 2478 of the 20 nm and 130 of the 100 nm nanoparticles). Over 99% of all nanoparticles were captured in a 25 μm region extending inwards from the membrane skin, with the pore size decreasing from >100 to <20 nm over this region (Figure 3.4). More than 90% of the 20 nm particles were captured in the final five microns of the 140 μm thick filter (region closest to the skin), while almost 60% of the 100 nm particles were captured in a band located between 10 and 15 μm in from the filter exit. These results are dramatically different than those for the Planova™ membranes, consistent with the highly asymmetric structure of the Viresolve® Pro membrane.

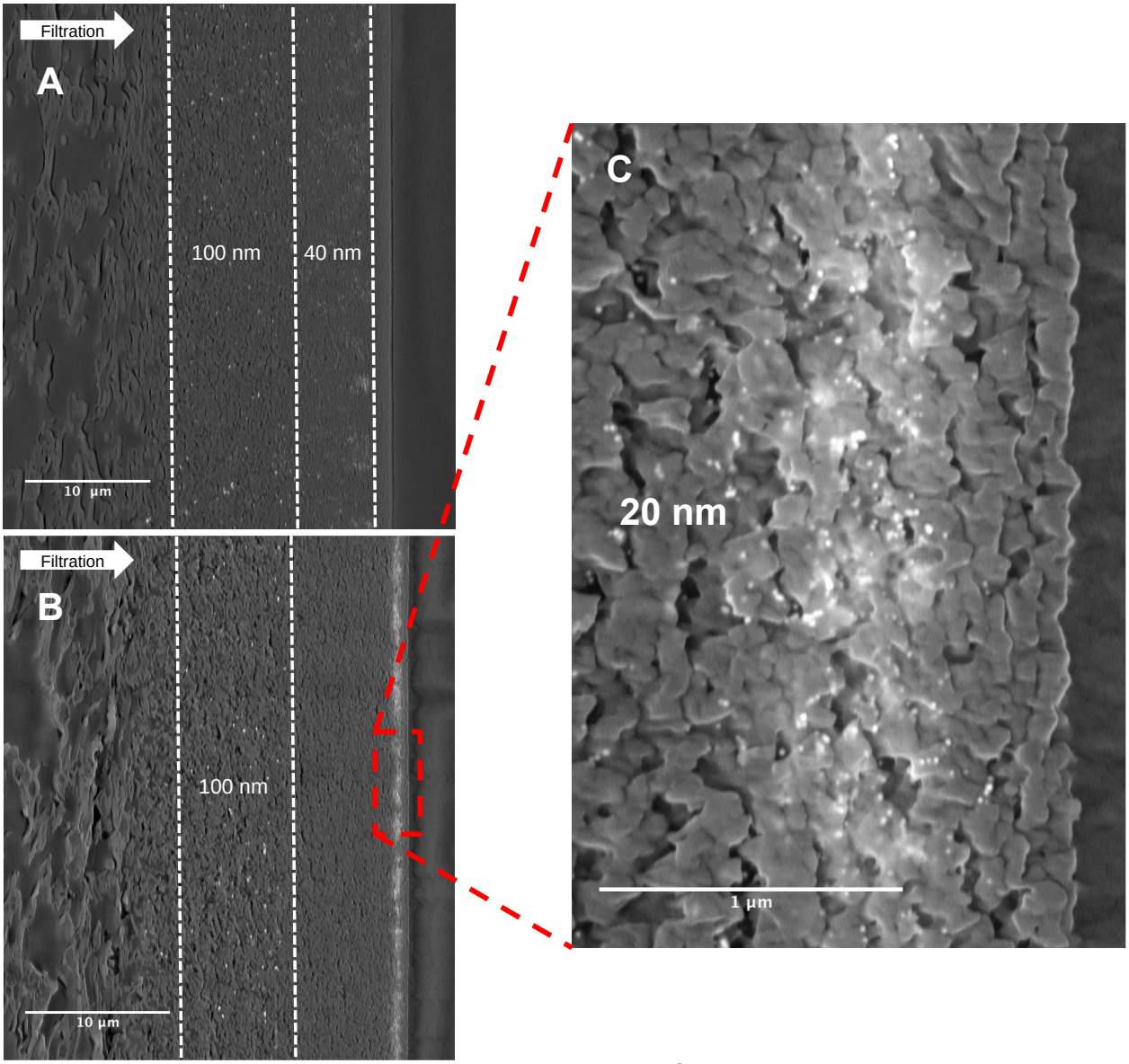

Figure 3.6 SEM images of cross-sections of the Viresolve® Pro membrane after challenge with (A) a mixture of 40 and 100 nm gold particles or (B) a mixture of 20 and 100 nm gold particles. (C) High magnification image (100,000X) of a small region showing capture of the 20 nm gold nanoparticles right near the skin-side (exit) of the membrane.

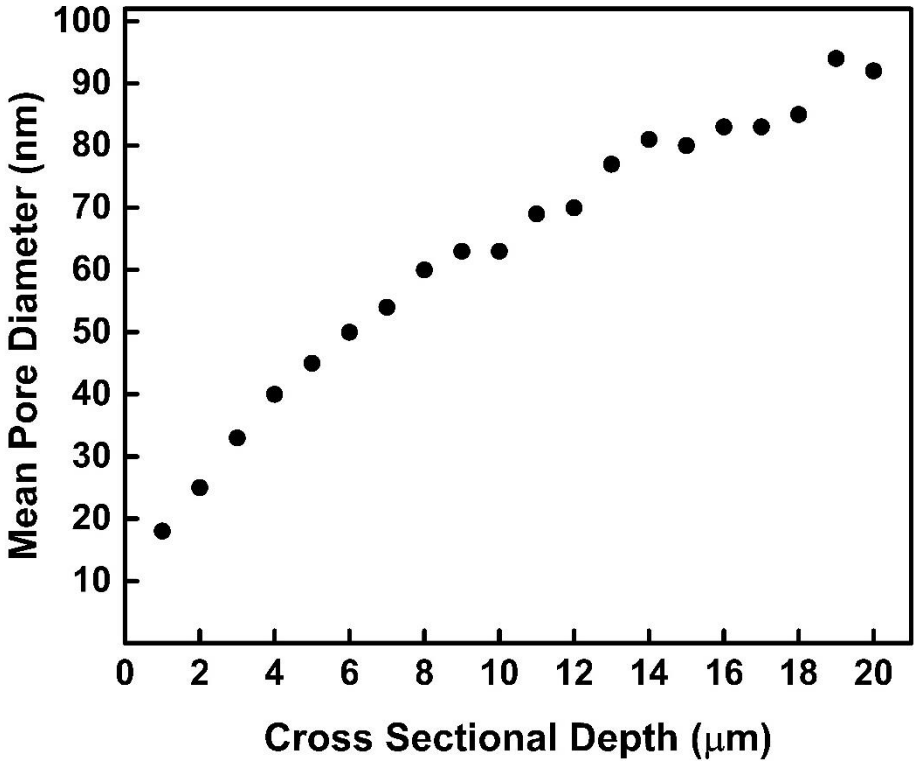

Figure 3.7 Euclidian Distance Mapping (EDM) estimation of pore size gradient for a typical Viresolve® Pro membrane.

3.3.5 Ultipor® DV20

The Ultipor® DV20 is also a flat-sheet membrane, but it has a much more homogeneous (symmetric) pore structure than the Viresolve® Pro membrane. Previous studies using dextran sieving measurements suggest that the pore size decreases by around a factor of two as one moves through the depth of the filter [17]. Filtration experiments were performed with a single-layer of the DV20 membrane using mixtures of the 20 and 100 nm nanoparticles at a pressure of 210 kPa (30 psig), yielding a nearly constant filtrate flux of 4.9 μm/s (18 L/m^2/h). The much lower filtrate flux with the DV20 compared to the

Viresolve® Pro membrane is consistent with the difference in pore structure; the nearly homogeneous pore size throughout the depth of the 20-25 µm thick DV20 provides much greater resistance to flow than the very large pores that dominate the structure through the more macroporous substructure of the Viresolve® Pro membrane.

An SEM image of the DV20 membrane (Figure 3.8) shows that most of the 20 nm gold nanoparticles are captured in a band approximately 3 µm thick near the filter inlet, although a number of them penetrated a few microns deeper into the filter. However, the 100 nm particles were retained immediately at the filter entrance, consistent with a pore size that is significantly less than 100 nm [17]. A separate experiment performed with the membrane oriented with the shiny side up (facing the nanoparticles suspension) showed that both the 20 and 100 nm gold particles were captured in a very thin band right at the entrance to the filter, with many particles simply sloughed off the filter when it was removed from the stainless steel holder. In both cases, there were essentially no nanoparticles observed in the depth of the DV20 filter. Similar conclusions were obtained using confocal microscopy with fluorescently-labeled bacteriophage and polystyrene nanoparticles [9,10].

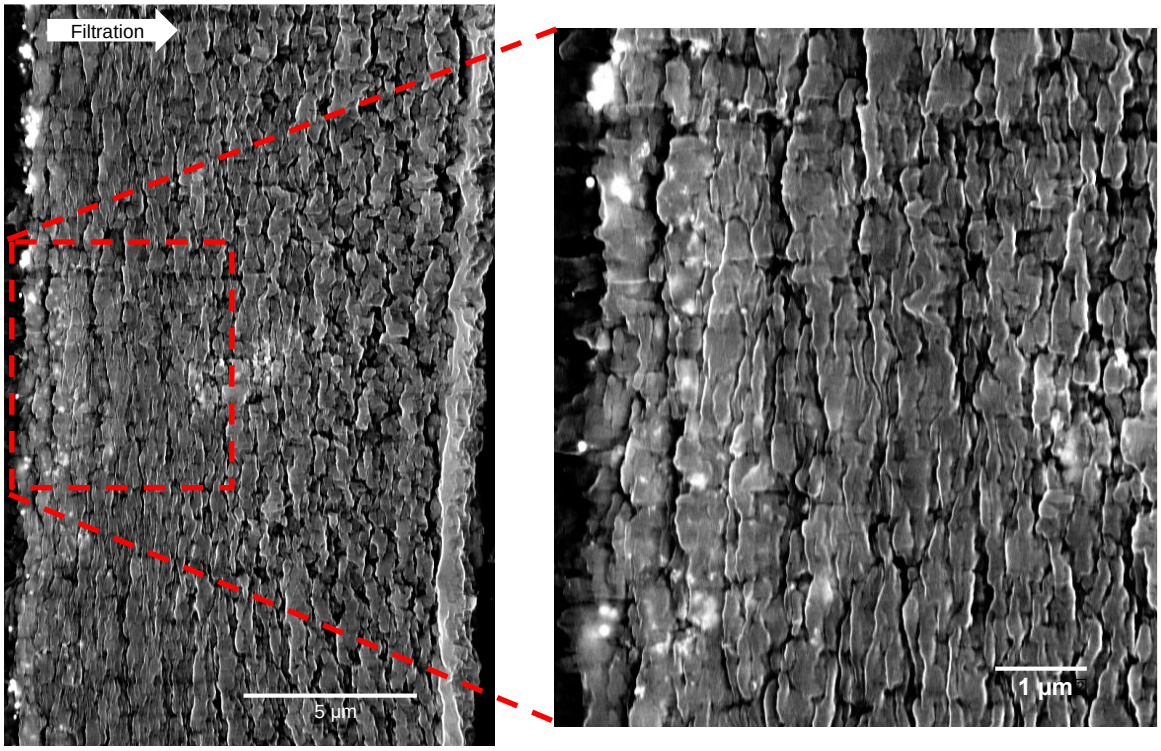

Figure 3.8 SEM image of a cross-section through an Ultipor® DV20 membrane after filtration of 30 L/m^2 of a suspension containing 20 and 100 nm gold nanoparticles at a constant pressure of 210 kPa (30 psig) with the skin-side away from feed.

3.4 Conclusions

Virus filtration is a critical part of the overall viral clearance strategy in the production of biotherapeutics like monoclonal antibodies. A number of manufacturers currently make virus filtration membranes with very different pore structures / morphology, but none of the available characterization techniques provide detailed insights into the variation of the pore size through the depth of the membrane or how this affects virus capture. This Chapter presents a new approach for characterizing virus filtration membranes based on the use of scanning electron microscopy to image gold nanoparticles captured within the membrane pores during actual filtration experiments. The gold

nanoparticles are monodisperse and available in a range of particle sizes, providing an opportunity to visualize the variation in pore size through the depth of the membrane.

SEM images of the hollow fiber Planova™ BioEx and 20N membranes show a slight asymmetry in the membrane pore size, with the 100 nm particles captured in the upper 5 µm of the membrane while the majority of the 20 nm particles were captured several microns into the membrane pore structure. This asymmetry was somewhat more pronounced with the Planova™ BioEx, with the peak in the distribution for the 20 nm particles occurring approximately 15 µm into the filter. A small number of isolated nanoparticles were observed throughout the depth of the Planova™ BioEx and 20N membranes, consistent with the stochastic nature of particle capture and the presence of some larger flow paths well into the depth of the filter.

In contrast to the results with the hollow fibers, nanoparticle capture in the highly asymmetric Viresolve Pro occurred deep within the filter, just upstream of the tight skin layer on the filter exit. The large majority of the 20 nm nanoparticles were captured in a thin band only 500 - 1000 nm upstream of the skin, while the 40 and 100 nm particles were captured further upstream. This behavior is consistent with the confocal microscopy images of fluorescently labeled viruses and nanoparticles presented in Chapter 2, but the much higher resolution of the SEM provides much more detailed and quantitative information on the variation in pore size within the depth of the filter.

SEM images of the flat sheet Ultipor® DV20 show a much more homogeneous pore structure, with the 100 nm particles nearly entirely excluded from the membrane pores while the 20 nm particles are captured relatively close to the filter inlet. This homogeneous

pore structure provides high levels of virus removal but very low permeability (water flux) due to the large resistance to flow.

The results reported in this Chapter clearly demonstrate the utility of using SEM analysis of gold nanoparticle capture to study the pore size and pore asymmetry in both hollow fiber and flat sheet virus filtration membranes. The application of indirect techniques such as evapoporometry for pore size estimation is often limited when asymmetric membranes with complex pore structures are being studied [18]. Besides, such approaches provide no information on the variation of the pore size with position through the depth of the membrane, which was one of the primary advantages of the SEM analysis. Direct techniques such as confocal laser scanning microscopy or optical coherence tomography, on the other hand, are unable to provide the resolution that is needed to detect sizes of small parvoviruses (i.e., 10 nm). The methodology presented in this Chapter should provide an important tool in developing a more fundamental understanding of the factors controlling the performance of virus filters with pores in the 10 – 100 nm size range.

Nonetheless, like any other characterization methodology, our approach is not free from potential sources of error or artifacts. For instance, the information acquired by SEM is limited by its small field of view to a small area of the membrane. Also, SEM does not allow for direct visualization of particles buried beneath the surface of a sectioned membrane. However, it should be possible to overcome these shortcomings by integrating images taken from multiple locations of a membrane or by membrane surface reconstruction using advanced 3D SEM techniques.

3.5 Literature Cited

[1] G. Miesegaes, S. Lute, K. Brorson, Analysis of viral clearance unit operations for monoclonal antibodies, Biotechnol Bioeng, 106 (2010) 238-246.

[2] P. Nestola, C. Peixoto, R.R. Silva, P.M. Alves, J.P. Mota, M.J. Carrondo, Improved virus purification processes for vaccines and gene therapy, Biotechnol Bioeng, 112 (2015) 843-857.

[3] G. Bolton, M. Cabatingan, M. Rubino, S. Lute, K. Brorson, M. Bailey, Normal-flow virus filtration: detection and assessment of the endpoint in bio-processing, Biotechnol Appl Biochem, 42 (2005) 133-142.

[4] M.E. Verbyla, J.R. Mihelcic, A review of virus removal in wastewater treatment pond systems, Water Res, 71 (2015) 107-124.

[5] M. Amarasiri, M. Kitajima, T.H. Nguyen, S. Okabe, D. Sano, Bacteriophage removal efficiency as a validation and operational monitoring tool for virus reduction in wastewater reclamation: Review, Water Res, 121 (2017) 258-269.

[6] S. Giglia, D. Bohonak, P. Greenhalgh, A. Leahy, Measurement of pore size distribution and prediction of membrane filter virus retention using liquid-liquid porometry, J Membrane Sci, 476 (2015) 399-409.

[7] R.I. Peinador, J.I. Calvo, K. ToVinh, V. Thom, P. Pradanos, A. Hernandez, Liquid-liquid displacement porosimetry for the characterization of virus retentive membranes, J Membrane Sci, 372 (2011) 366-372.

[8] J.I. Calvo, R.I. Peinador, P. Pradanos, L. Palacio, A. Bottino, G. Capannelli, A. Hernandez, Liquid-liquid displacement porometry to estimate the molecular weight cut-off of ultrafiltration membranes, Desalination, 268 (2011) 174-181.

[9] M. Bakhshayeshi, N. Jackson, R. Kuriyel, A. Mehta, R. van Reis, A.L. Zydney, Use of confocal scanning laser microscopy to study virus retention during virus filtration, J Membrane Sci, 379 (2011) 260-267.

[10] F. Fallahianbijan, S. Giglia, C. Carbrello, A.L. Zydney, Use of fluorescently-labeled nanoparticles to study pore morphology and virus capture in virus filtration membranes, J Membrane Sci, 536 (2017) 52-58.

[11] F.J. Marquez-Rocha, M. Aguilar-Juarez, M.J. Acosta-Ruiz, M.I. Gradilla, Rapid characterization of ultrafiltration membranes by scanning electron microscopy, Russ Chem B+, 50 (2001) 1320-1322.

[12] J.I. Calvo, R.I. Peinador, P. Pradanos, A. Bottino, A. Comite, R. Firpo, A. Hernandez, Porosimetric characterization of polysulfone ultrafiltration membranes by image analysis and liquid-liquid displacement technique, Desalination, 357 (2015) 84-92.

[13] S. Sekine, M. Komuro, T. Sohka, T. Sato, Integrity testing of Planova BioEX virus removal filters used in the manufacture of biological products, Biologicals, 43 (2015) 186-194.

[14] T. Tsurumi, T. Sato, N. Osawa, H. Hitaka, T. Hirasaki, K. Yamaguchi, Y. Hamamoto, S. Manabe, T. Yamashiki, N. Yamamoto, Structure and filtration performances of improved cuprammonium regenerated cellulose hollow fiber (improved Bmm hollow fiber) for virus removal, Polym J, 22 (1990) 1085-1100.

[15] T. Tsurumi, N. Osawa, T. Hirasaki, K. Yamaguchi, S. Manabe, T. Yamashiki, Mechanism of removing monodisperse gold particles from a suspension using cuprammonium regenerated cellulose hollow fiber (Bmm hollow fiber), Polym J, 22 (1990) 304-311.

[16] P. Kosiol, B. Hansmann, M. Ulbricht, V. Thom, Determination of pore size distributions of virus filtration membranes using gold nanoparticles and their correlation with virus retention, J Membrane Sci, 533 (2017) 289-301.

[17] M. Bakhshayeshi, A.L. Zydney, Effect of solution pH on protein transmission and membrane capacity during virus filtration, Biotechnol Bioeng, 100 (2008) 108-117.

[18] W.B. Krantz, A.R. Greenberg, E. Kujundzic, A. Yeo, S.S. Hosseini, Evapoporometry: A novel technique for determining the pore-size distribution of membranes, J Membrane Sci, 438 (2013) 153-166.

Chapter 4
Impact of Protein Fouling on Nanoparticle Capture within the Viresolve® Pro and Viresolve® NFP Virus Removal Membranes

The work presented in this Chapter is based on the material published in:
Fallahianbijan, F., S. Giglia, C. Carbrello, A.L. Zydney, "Impact of Protein Fouling on Nanoparticle Capture within the Viresolve® Pro and Viresolve® NFP Virus Removal Membranes," Biotech. Bioeng. (in press).

4.1 Introduction

Complex recombinant therapeutic proteins, including monoclonal antibodies that are used to treat cancers and immune disorders, are commonly expressed in mammalian cell lines [1]. These biopharmaceutical products can thus be contaminated by endogenous retroviruses like particles derived from the cell culture or by adventitious parvoviruses introduced into the product stream through media supplements, buffers, and process equipment [2,3]. Therefore, the downstream purification process used in clinical manufacturing must provide sufficiently high levels of virus clearance to ensure the safety of these biotherapeutics [4].

Virus filtration is a robust and well-established technique that provides high levels of virus removal based primarily on a size exclusion mechanism[5,6]. Commercial parvovirus filters are specifically designed to achieve more than 99.99% removal of small parvoviruses (18-26 nm) while allowing high transmission of the product of interest, e.g., monoclonal antibodies that are around 8-10 nm in size. Virus filtration is typically performed using normal flow (dead-end) operation due to the simplicity and lower cost

compared to tangential flow filtration [7]. However, the use of normal flow filtration can often cause significant membrane fouling, leading to a reduction in filtrate flux, a loss in product yield, and changes in virus retention. For example, Bolton et al. (2005) [8] showed a high correlation between virus retention (LRV = log reduction value) and the extent of flux decline during filtration of an IgG solution through the Viresolve® NFP membrane. The authors attributed this behavior to the preferential blockage of the smaller pores within the membrane by the filtered protein. In contrast, membrane fouling by large polystyrene beads led to cake formation which had no affect on virus retention. However, studies using the Viresolve® Pro membrane showed no change in LRV during filtration of highly fouling protein feeds [9,10], while studies of the Ultipor® DV20 virus filter showed a significant decrease in virus retention even in the absence of any flux decline [11]. The origin of these differences in behavior is currently uncertain.

The objective of the work described in this Chapter was to obtain quantitative information on the effects of protein fouling on the retention characteristics of the Viresolve® Pro and Viresolve® NFP membranes using gold nanoparticles. The location of the nanoparticles within the virus filters, either “clean” or after protein fouling, was determined by scanning electron microscopy using the approach described in Chapter 3. The combination of the SEM images and flux decline data provide new insights into the underlying fouling mechanisms and their relationship to the virus retention characteristics of these widely-used virus filters.

4.2 Materials and Methods

4.2.1 Virus Filtration Membranes

Highly asymmetric Viresolve® Pro (PES) and Viresolve® NFP (PVDF) parvovirus-retentive membranes provided by MilliporeSigma (Burlington, MA). The membranes were cut into 47 mm discs from flat sheet-stock and used in single layer format to facilitate imaging by confocal microscopy. The commercial devices employ multiple layers of membrane to obtain the high levels of viral clearance required in bioprocessing applications.

4.2.2 Solution Preparation

Phosphate buffer solutions were prepared by dissolving 0.03 M Na_2HPO_4 and 0.03 M KH_2PO_4 (both from MilliporeSigma, Burlington, MA) in deionized distilled water obtained from a Direct-Q® 3 UV Water Purification System (MilliporeSigma, Burlington, MA) with resistivity greater than 18 MΩ cm. The pH was measured using a model 420Aplus Thermo Orion pH meter (Orion Technology, Beverly, MA) and adjusted to 7.2 by adding small quantities of 1 M NaOH (J.T. Baker) as needed. Buffer solutions were pre-filtered through 0.2 μm pore-size Supor®-200 membranes (Pall Corp., Ann Arbor, MI) to remove any particles or undissolved salts prior to use.

Human serum immunoglobulin G (IgG, SeraCare Life Sciences, Milford, MA, Product Number HS-470) was used as a model protein in most experiments. IgG solutions were prepared fresh for each experiment by dissolving the appropriate amount of protein

powder in phosphate buffer at room temperature. All protein solutions were filtered through 0.2 µm syringe filters (VWR 28145-487) immediately prior to performing the virus filtration experiments. Protein concentrations were evaluated using a NanoDrop™ 2000 (Thermo Scientific, Wilmington, DE) UV-Vis spectrophotometer, with the absorbance measured at 280 nm.

Gold nanoparticles (20, 40, and 100 nm) were obtained from MilliporeSigma (Burlington, MA) as stabilized suspensions in citrate buffer. Nanoparticle suspensions were diluted with phosphate buffer and ultrasonicated for a short time to eliminate any aggregates. More details on the nanoparticle solutions are provided in Chapter 3

4.2.3 Protein / Nanoparticle Filtration

All filtration experiments were performed using a 47 mm stainless steel filter holder (MilliporeSigma, Burlington, MA), with the virus membrane oriented with the selective skin layer (shiny side) facing downstream as per the manufacturer's recommendation. The virus membranes were supported on a stainless screen. Experiments were performed at a constant pressure of 210 kPa (30 psig), which was maintained by nitrogen pressurization of the feed reservoir. The membranes were initially flushed with at least 40 L/m^2 of phosphate buffer to ensure complete wetting and to remove any air bubbles trapped in the system. Protein fouling was performed using 1 g/L solutions of IgG, while gold nanoparticle suspensions had concentrations around 10^{10} particles / mL for the 20 nm particles and 10^8 particles / mL for the 40 and 100 nm particles. Filtrate flux was evaluated by timed collection. At the end of the experiment, i.e., after challenging the filter with

nanoparticles and / or protein, the membrane was removed from the holder, rinsed gently with DI water, and prepared for imaging.

4.2.4 Scanning Electron Microscopy

The virus membranes were cut into small strips (10×3 mm) and air-dried for at least 48 hr. Drying in ethanol, as was used in Chapter 3, led to artifacts with the protein-fouled membranes. The individual strips were incubated with LR white medium grade embedding resin (Electron Microscopy Sciences, Hartfield, PA) twice for two hours at room temperature. The samples were transferred to clean snap-fit gelatin capsules (Ted Pella, Inc., Rodding, CA), which were then filled with fresh LR white resin and placed in an oven at 65 °C to cure for 48 hr. A Leica EM UC6 Ultramicrotome (Leica Biosystems Inc., Buffalo Grove, IL) was used to obtain thin (1 μm thick) slices of the virus membrane. These were coated with a thin layer of iridium using an Emitech K575X sputter coater (Quorum Technologies Ltd, UK) to avoid charging of the membrane in the high energy electron beam. Additional details on the sample preparation are available in Chapter 3.

The membrane cross-section was examined at high-magnification using a Zeiss Sigma VP-FESEM (Carl Zeiss Microscopy, Thornwood, NY, US) equipped with a retractable five-diode backscattered detector. This provided high contrast between the gold nanoparticles and the sputter-coated membrane.

Figure 4.1 is an illustration of the cross-sections of both the Viresolve® Pro (right panel) and Viresolve® NFP (left panel) membranes obtained by scanning electron microscopy. The pore size in the Viresolve® Pro membrane decreases gradually from

micron scale to approximately 20 nm as one moves from membrane entrance toward the retentive layer across the 140 μm thickness of the membrane. However, the pore structure of the Viresolve® NFP membrane is more uniform over the entrance region of the filter, reflecting the casting of the ultrafiltration layer on top of a 0.2 μm pore size microfiltration membrane. The pore size then decreases sharply within the last 10-15 μm near the filter exit.

More details on the pore size gradients within the Viresolve® Pro and Viresolve® NFP membranes was obtained by Euclidian Distance Mapping (EDM) using high resolution SEM images across the depth of the membrane as described in Chapter 3. Figure 4.2 shows a comparison of the results of the EDM analysis, with the estimated mean pore size plotted as a function of the distance measured inwards from the filter exit. The pore size at the exit of the Viresolve® Pro membrane was approximately 18 nm, increasing smoothly and monotonically as one moves into the depth of the filter (away from skin). The pore size attains a value of approximately 650 nm at the opposite end of the membrane, i.e., the feed inlet since these membranes are operated with the flow entering through the macroporous region first. In contrast, the pore size within the Viresolve® NFP membrane increases sharply from about 14 nm at the filter exit to 300 nm about 12 μm into the depth of the membrane, after which the pore size remains nearly constant at a value of about 300 nm.

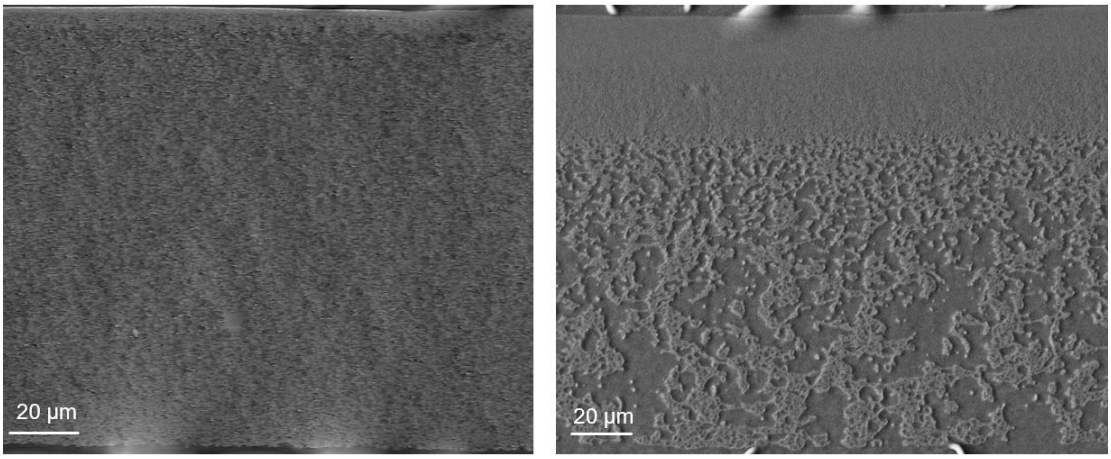

Figure 4.1 Scanning Electron Micrographs (SEM) of the cross-section of Viresolve® NFP (left panel) and Viresolve® Pro (right panel) membranes.

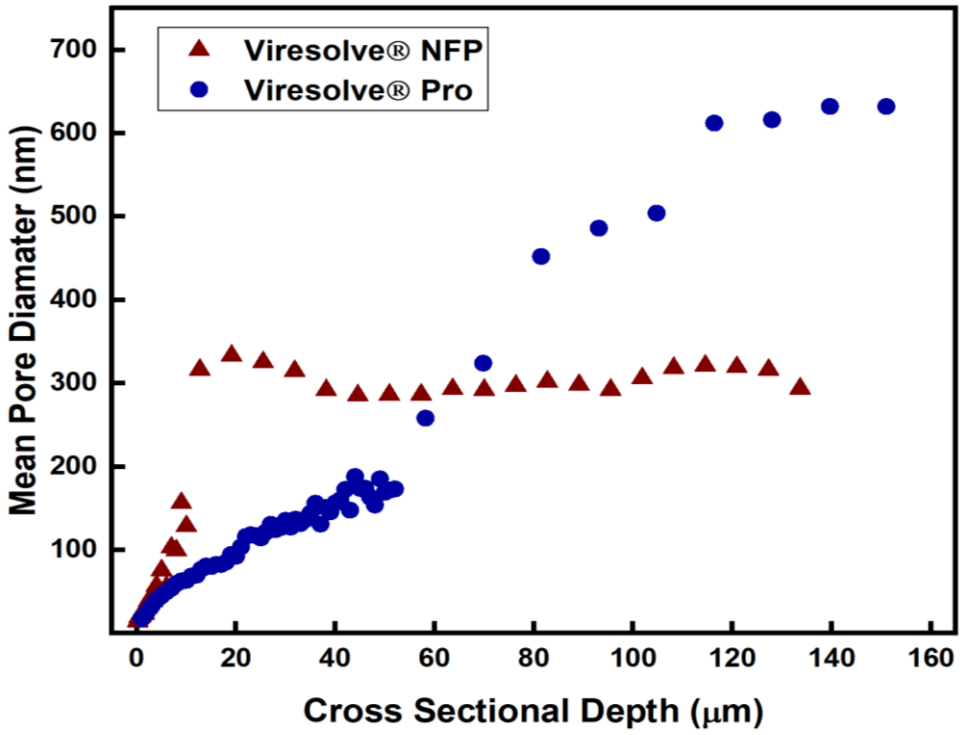

Figure 4.2 Euclidian Distance Mapping (EDM) analysis of pore size gradient for Viresolve® NFP and Viresolve® Pro membranes

4.3 Results and Discussion

4.3.1 Flux Decline Behavior

Figure 4.3 shows typical experimental data for the filtrate flux during filtration of 1 g/L solutions of the IgG through the Viresolve® Pro and Viresolve® NFP membranes at a constant pressure of 210 kPa (30 psig). The data are plotted as a function of the volumetric throughput, which is defined as the cumulative filtrate volume (V) divided by the membrane cross-sectional area (A). Results are shown for two repeat experiments for each membrane, using a fresh membrane for each experiment, with the data showing a high degree of reproducibility (variations typically less than 10%). The initial flux through the Viresolve® Pro membrane (1250 $L/m^2/h$) was nearly 30% greater than that through the Viresolve® NFP membrane (950 $L/m^2/h$). In addition, the Viresolve® Pro membrane showed a much lower rate of fouling, with the flux decreasing by 90% after filtration of approximately 40 L/m^2 of the IgG solution compared to a similar flux decline after only 10 L/m^2 with the Viresolve® NFP membrane. The net result is that the flux through the Viresolve® Pro membrane after filtration of 10 L/m^2 was more than 6 times as large as the flux through the Viresolve® NFP membrane at the same throughput. Both membranes showed high transmission of the IgG, with the permeate concentrations being greater than 0.95 g/L in all samples (after a small dilution effect in the first couple of samples).

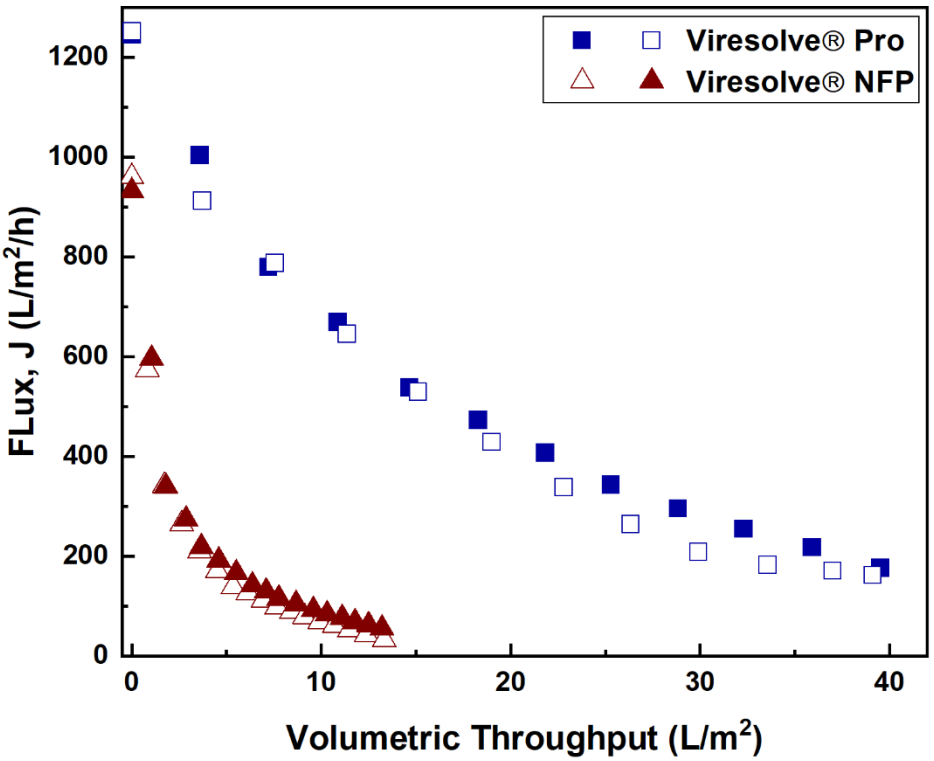

Figure 4.3 Filtrate flux as a function of volumetric throughput for filtration of 1 g/L solutions of IgG through the Viresolve® Pro and Viresolve® NFP membranes at constant pressure of 210 kPa (30 psig).

4.3.2 Nanoparticle Capture in Viresolve® Pro

Figure 4.4 shows a series of SEM images of four Viresolve® Pro membranes, each challenged with 15 L/m^2 of a solution containing 20 nm gold nanoparticles at a concentration of approximately 6×10^{10} particles / mL. The left-most panel (A) shows results for a clean membrane which was flushed with buffer and then immediately challenged with the gold nanoparticles. The other panels show membranes that were first used to filter 1 g/L solutions of the IgG at a constant pressure of 210 kPa until a target level of fouling: B = 30% flux decline, C = 60%, and D = 90%, with the protein-fouled membranes immediately challenged with the gold nanoparticles after completion of the

protein filtration. The filtrate flux through each membrane during the gold nanoparticle filtration remained relatively constant (variation in flux of less than 5% except for the experiment in Panel B which showed a somewhat larger flux decline during the gold nanoparticle filtration).

The high magnification images show the region near the filter exit above the open gaps in the stainless steel support; there were almost no nanoparticles visible in the first 130 μm into the depth of the 140 μm thick filter. The 20 nm gold nanoparticles are easily visible as bright spots located in a relatively narrow band located between 300 and 950 nm upstream from the filter exit for the clean membrane (Panel A). The location of the particle band was shifted further upstream after membrane fouling, particularly for the more heavily fouled membranes, with the midpoint of the band moving from 670 ± 20 nm for the clean membrane to 750 ± 20 nm after the 30% flux decline, 860 ± 20 after the 60% flux decline, and 1460 ± 30 after the 90% flux decline. This shift in nanoparticle capture is likely due to a reduction in the effective pore size within the selective region of the Viresolve® Pro membrane, with the pore size decreasing to <20 nm at a point further away from the skin layer (membrane exit) as the membrane becomes more heavily fouled.

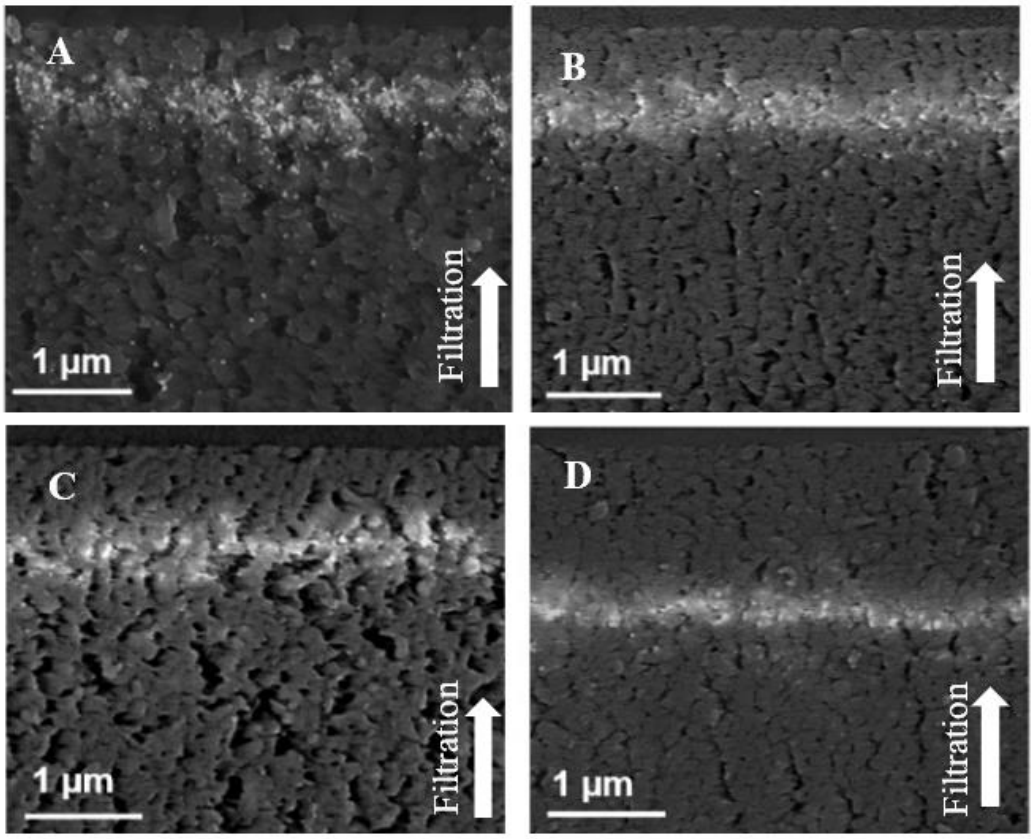

Figure 4.4 High magnification SEM images of the cross-section of Viresolve® Pro membranes challenged with 15 L/m^2 of a suspension containing 20 nm gold nanoparticles at 210 kPa: (A) Clean (B) after fouling with IgG to a 30% flux decline, (C) after fouling to a 60% flux decline, and (D) after fouling to a 90% flux decline.

The distribution of 20 nm gold nanoparticles captured within the Viresolve® Pro membranes were quantified by direct counting of the individual nanoparticles in the SEM images using ImageJ software. A total of more than 500 nanoparticles were counted in each filter. The resulting histograms for the clean and IgG-fouled membranes (from Figures 4.4A and 4.4D) are shown in Figure 4.5, where the count represents the percentage of captured nanoparticles within a given 0.5 µm thick slice within the Viresolve® Pro membrane. More than 65% of the 20 nm gold particles were captured in the 1.0 µm region

located immediately upstream of the exit (skin layer) in the clean membrane. In contrast, less than 2% of the 20 nm nanoparticles were captured in this same 1.0 µm region in the Viresolve® Pro membrane that had been initially fouled with the 1 g/L IgG solution to a flux decline of 90%. Instead, the largest fraction of the captured nanoparticles in the fouled membrane was located between 1.5 and 2.0 µm upstream from the membrane exit.

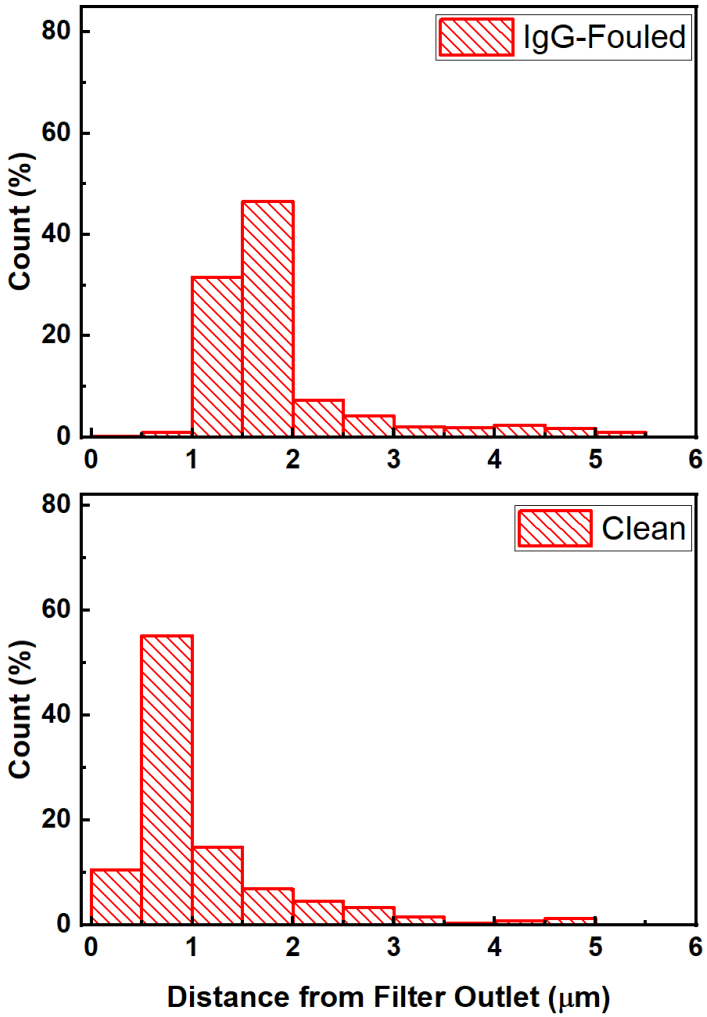

Figure 4.5 Distribution of 20 nm gold nanoparticles captured within the depth of the Viresolve® Pro membrane either clean (bottom) or after IgG fouling with 90% flux decline (top panel). Count is defined as the percentage of 20 nm particles retained in the specific region of interest (0.5 µm thick) relative to the total number of 20 nm particles captured within the membrane as determined by ImageJ analysis of the SEM images.

The fouling experiments in Figure 4.4 were repeated using a series of Viresolve® Pro membranes challenged with 30 L/m^2 of a suspension containing a mixture of 40 and 100 nm gold nanoparticles at a constant pressure of 210 kPa. SEM images for the clean membrane and for a membrane that was first used to filter a 1 g/L IgG solution until a 90% decline in filtrate flux are shown in Figure 4.6. The 40 and 100 nm gold nanoparticles are captured significantly further upstream of the membrane exit than the 20 nm particles, a direct result of the pore size gradient within the Viresolve® Pro membrane (Figure 4.2). In sharp contrast to the results in Figure 4.4, the locations of the 40 and 100 nm particles were essentially identical for the clean and fouled membranes even though the image in the right hand panel was obtained after a 90% decline in filtrate flux during the IgG filtration. Both images show the 40 nm particle bands at 5.4 ± 0.2 μm in from the membrane exit, with the 100 nm bands located at 14.7 ± 0.3 μm and 13.6 ± 0.2 μm within the clean and fouled membranes, respectively. This small difference for the 100 nm bands likely reflects the inherent variability in images for different membrane samples.

Further analysis of the location and distribution of captured 40 nm and 100 nm particles within the depth of the Viresolve® Pro membrane was obtained by ImageJ software and is shown in Figure 4.7. More than 400 nanoparticles, including both 40 and 100 nm gold particles were counted. The large majority of the 40 nm particles were retained in the region 2-10 μm upstream of the filter exit with no noticeable difference seen in the histograms for the fouled and clean membrane. The capture of the 100 nm particles occurred considerably further into the depth of the filter, with over 95% of the 100 nm particles captured in the region located 10-20 μm from filter exit for both the fouled and

clean Viresolve® Pro membranes. Thus, IgG fouling appears to have no significant affect on the capture of the larger size particles (>40 nm) within the Viresolve® Pro membrane.

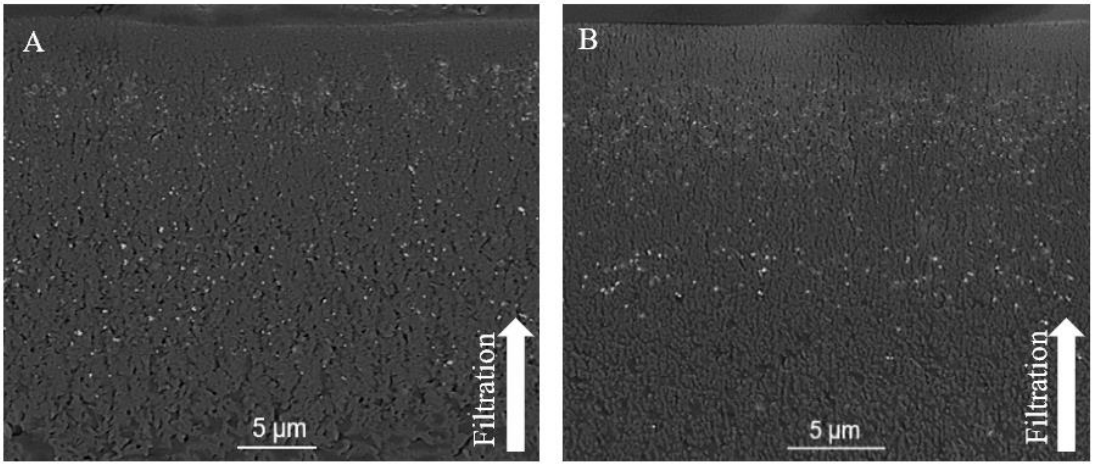

Figure 4.6 SEM images of Viresolve® Pro membranes challenged at 210 kPa with 30 L/m^2 of a suspension containing 40 and 100 nm gold nanoparticles: (A) Clean membrane, (B) After filtration of a 1 g/L IgG solution to 90% flux decline.

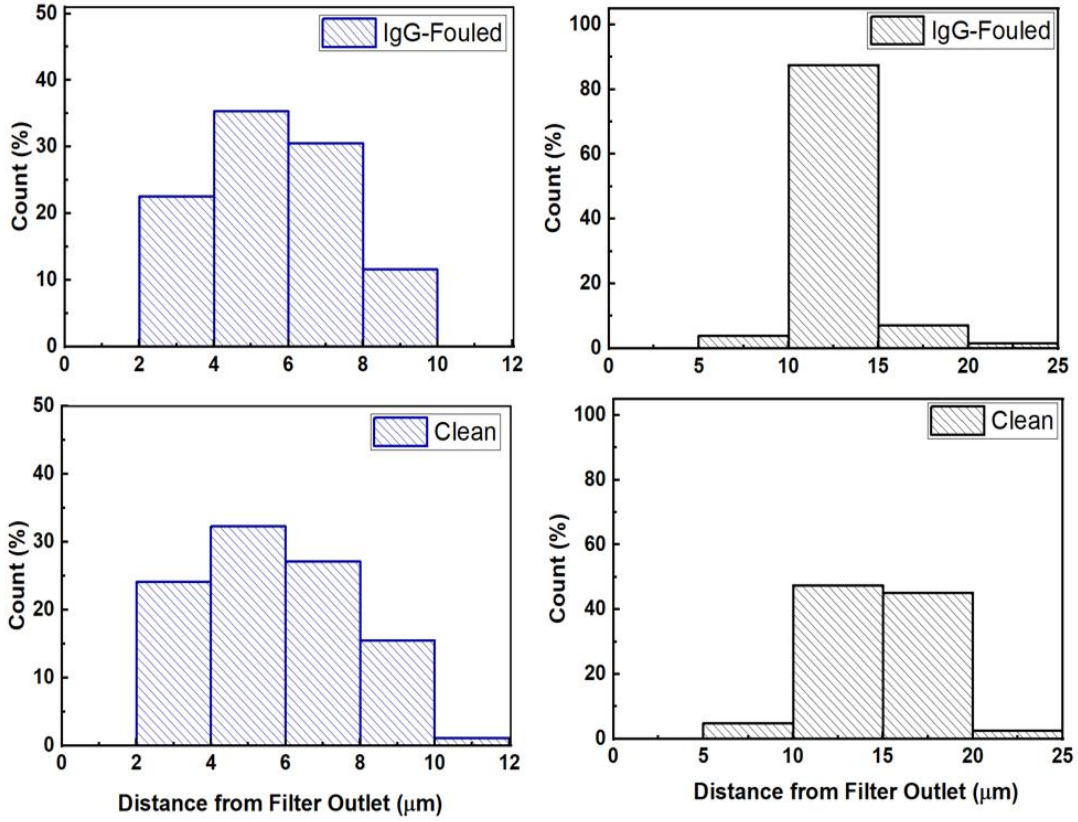

Figure 4.7 Distribution of 40 nm (left panel) and 100 nm (right panel) gold nanoparticles captured through the depth of the clean Viresolve® Pro membrane (bottom) or after IgG fouling up to 90% flux decline (top panel).

4.4 Nanoparticle Capture in Viresolve® NFP Membrane

Figure 4.8 shows SEM images of two Viresolve® NFP membranes challenged with 15 L/m^2 of 20 nm gold nanoparticles, one clean (left panel) and one after filtration of a 0.5 g/L solution of IgG until a flux decline of approximately 90% (right panel). A more dilute IgG solution was used in these experiments due to the much more rapid flux decline for the Viresolve® NFP membrane compared to that for the Viresolve® Pro membrane. The 20 nm gold nanoparticles are captured in a narrow band located approximately 250 nm upstream of the membrane exit, which is much closer to the skin than was seen with the

Viresolve® Pro membrane. In addition, there was a small number of nanoparticles captured somewhat further upstream of the bright band. In contrast to the results with the Viresolve® Pro membrane (shown in Figure 4.4), the SEM images of the 20 nm particles in the clean and fouled Viresolve® NFP membranes were essentially identical. Thus, IgG fouling caused no measurable shift in the nanoparticle capture profile within the Viresolve® NFP membrane, even after nearly a 90% decline in flux.

The distribution of captured 20 nm gold nanoparticles across the depth of both the clean and 90% fouled Viresolve® NFP membranes is shown in Figure 4.9 based on the ImageJ analysis. More than 95% of the 20 nm particles were retained within the last 1.5 μm of both the clean and fouled membranes, and there was again no significant difference in the location of the captured nanoparticles after fouling of the Viresolve® NFP membrane. Similar results were obtained with the 40 and 100 nm gold nanoparticles as shown in Figure 4.10, with no observable change in capture behavior after IgG fouling. However, the much steeper pore size gradient of the Viresolve® NFP membrane did cause the 40 and 100 nm particles to be captured much closer to the filter exit than was seen with the Viresolve® Pro.

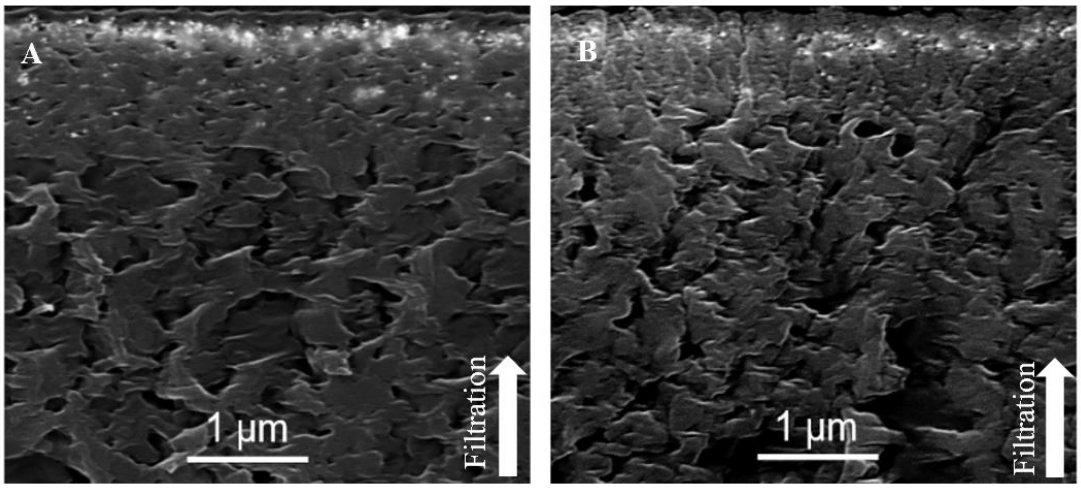

Figure 4.8 SEM images of Viresolve® NFP membranes challenged at 210 kPa with 15 L/m^2 of a suspension of 20 nm gold nanoparticles: (A) clean, (B) after filtration of a 0.5 g/L IgG solution to a flux decline of 90%.

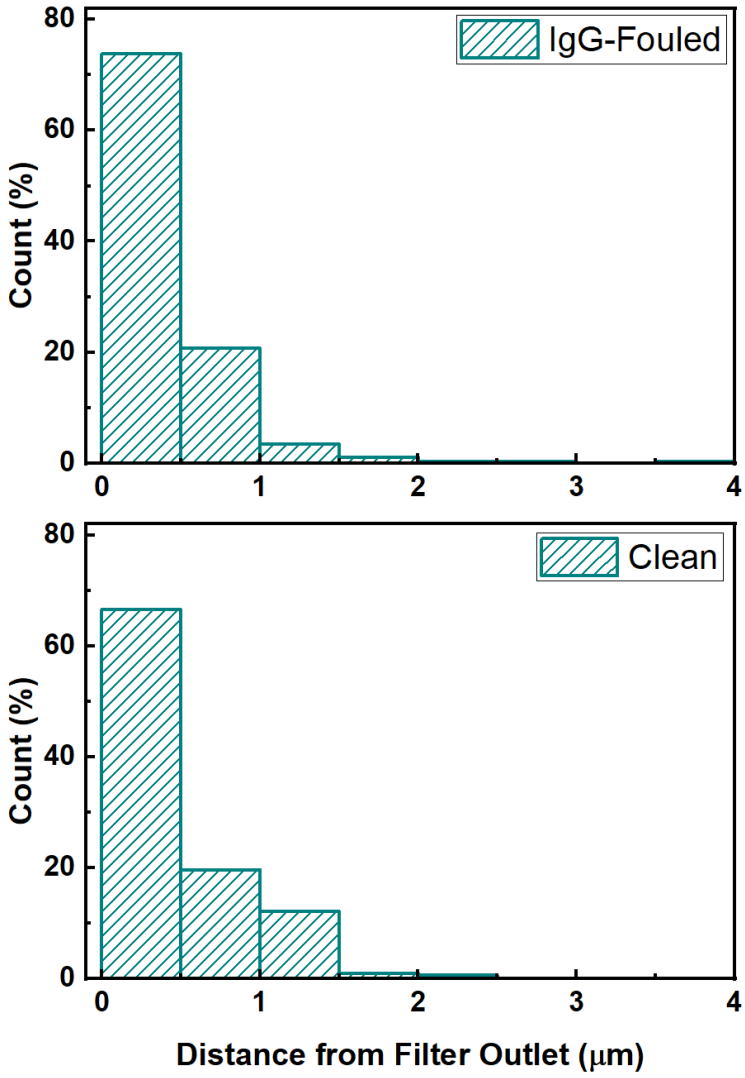

Figure 4.9 Distribution of 20 nm gold nanoparticles captured within the depth of the clean (bottom) and IgG-fouled to 90% flux decline (top) for the Viresolve® NFP membrane.

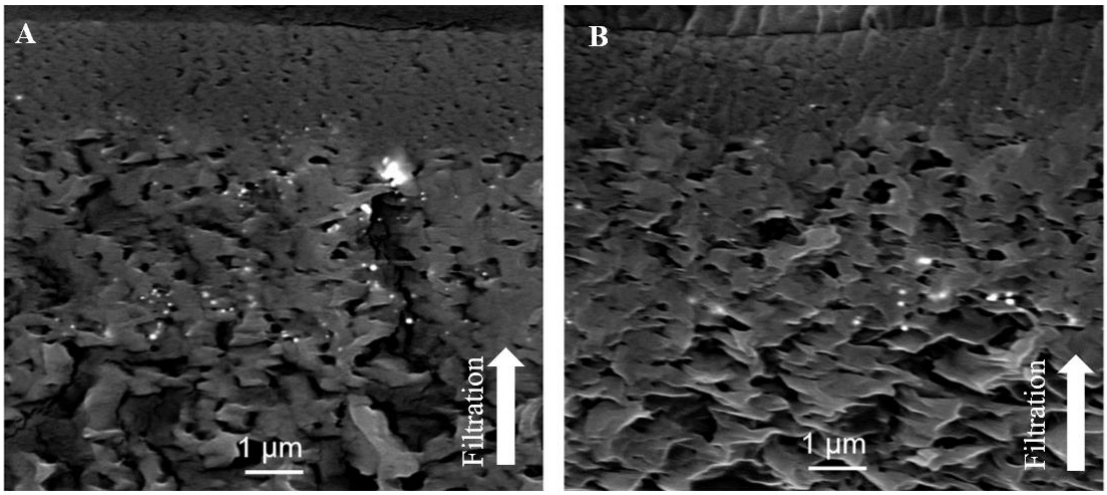

Figure 4.10 SEM images of the Viresolve® NFP membranes challenged with a mixture of 40 and 100 nm gold nanoparticles at 210 kPa: (A) Clean, (B) after filtration of a 0.5 g/L solution of IgG until a flux decline of 90%.

4.5 Conclusions

Although a number of previous studies have demonstrated that membrane fouling can alter the virus retention characteristics in certain virus filters, the results presented in this Chapter provide the first evidence for how protein fouling alters the nature / location of nanoparticle capture within these filters. IgG fouling in the Viresolve® Pro membrane caused a distinct shift in the location at which the 20 nm gold nanoparticles were captured, with the particle band moving further upstream (away from the skin layer and into the depth of the membrane) as the extent of fouling increased. Very few nanoparticles were captured within the first 1 µm upstream of the exit for the Viresolve® Pro membrane after a 90% flux decline with IgG, even though this was the region where the large majority of the 20 nm particles were located in the clean membrane. This shift in nanoparticle location was not seen with the larger 40 and 100 nm particles.

In contrast to the results with the Viresolve® Pro membrane, nanoparticle capture in the Viresolve® NFP membrane was largely unaffected by IgG fouling for any of the different size nanoparticles. Thus, the affect of protein fouling on nanoparticle capture clearly depends on the underlying structure / properties of the membrane. The rate of flux decline seen with the Viresolve® NFP membrane was much greater than that for the Viresolve® Pro membrane, and nanoparticle capture occurred closer to the membrane exit (for the 20, 40, and 100 nm nanoparticles). Note that Kosiol et al. [12] have previously observed that protein fouling is more rapid in virus filtration membranes with steeper pore size gradients.

Although it is not possible to directly determine the location / nature of the underlying protein fouling from the data presented in this Chaper, the observed differences in nanoparticle capture within the Viresolve® Pro and Viresolve® NFP membranes do suggest the following interpretation. IgG fouling within Viresolve® Pro membrane likely occurs in the region right near the membrane exit, reducing the effective pore size in this region thereby shifting the location of the 20 nm nanoparticles further upstream (away from) the membrane skin. This behavior is consistent with experimental observations showing highly robust virus retention by the Viresolve® Pro membrane even in the presence of significant protein fouling. IgG fouling had minimal affect on the location of the captured 40 and 100 nm nanoparticles in the Viresolve® Pro membrane, either because there was minimal fouling in these large pores or because any change in effective pore size was small relative to the size of these pores. The lack of any measurable shift in the capture location of the 20 nm nanoparticles in the Viresolve® NFP membrane, even after a flux

decline of 90%, would be consistent with the hypothesis that protein fouling occurs preferentially in the smallest pores in the Viresolve® NFP membrane, which is the physical model used by Bolton et al. [8] to explain the observed increase in virus transmission through the Viresolve® NFP membrane after protein fouling. The ability to directly observe the effects of protein fouling on nanoparticle capture provides unique insights into the fouling phenomena in these virus filtration membranes and the potential impact of this fouling on virus retention.

4.6 Literature Cited

[1] H. Rabenau, V. Ohlinger, J. Anderson, B. Selb, J. Cinantl, W. Wolf, J. Frost, P. Mellor, H. Wilhelm Doerr, Contamination of genetically engineered CHO-cells by epizootic haemorrhagic disease virus (EHDV), Biologicals. 21 (1993) 207–214.

[2] G. Sofer, J. Carter, Viral Clearance: A strategy for quality by design and the design space, in: A. Rathore, R. Mhatre (Eds.), Qual. by Des. Biopharm., John Wiley & Sons, Inc., Hoboken, NJ, USA, 2008: pp. 143–159. doi:10.1002/9780470466315.ch8.

[3] G. Miesegaes, S. Lute, K. Brorson, Analysis of viral clearance unit operations for monoclonal antibodies, Biotechnol. Bioeng. 106 (2010) 238–246. doi:10.1002/bit.22662.

[4] T. Ireland, H. Lutz, M. Siwak, G. Bolton, Viral filtration of plasma-derived human IgG, Pharm. Technol. Eur. 18 (2006) 43–49.

[5] M. Burnouf, T; Radosevich, Nanofiltration of plasma-derived biopharmaceutical products, Haemophilia. 9 (2003) 24–37.

[6] F. Fallahianbijan, S. Giglia, C. Carbrello, A.L. Zydney, Use of fluorescently-labeled nanoparticles to study pore morphology and virus capture in virus filtration membranes, J. Memb. Sci. 536 (2017) 52–58. doi:10.1016/j.memsci.2017.04.066.

[7] Z.H. Syedain, D.M. Bohonak, A.L. Zydney, Protein fouling of virus filtration membranes: Effects of membrane orientation and operating conditions, Biotechnol. Prog. 22 (2006) 1163–1169. doi:10.1021/bp050350v.

[8] G. Bolton, M. Cabatingan, M. Rubino, S. Lute, K. Brorson, M. Bailey, Normal-flow virus filtration: detection and assessment of the endpoint in bio-processing., Biotechnol. Appl. Biochem. 42 (2005) 133–142. doi:10.1042/BA20050056.

[9] P. Genest, H. Ruppach, C. Geyer, M. Asper, J. Parrella, B. Evans, A. Slocum, Artifacts of virus filter validation, Bioprocess Int. 11 (2013) 54–61.

[10] D. Lacasse, P. Genest, K. Pizzelli, P. Greenhalgh, L. Mullin, A. Slocum, Impact of Process Interruption on Virus Retention of Small-Virus Filters, Bioprocess Int. 11 (2013) 32–44.

[11] N.B. Jackson, M. Bakhshayeshi, A.L. Zydney, A. Mehta, R. van Reis, R. Kuriyel, Internal virus polarization model for virus retention by the Ultipor® VF Grade DV20 membrane, Biotechnol. Prog. 30 (2014) 856–863. doi:10.1002/btpr.1897.

[12] P. Kosiol, M.T. Müller, B. Schneider, B. Hansmann, V. Thom, M. Ulbricht, Determination of pore size gradients of virus filtration membranes using gold nanoparticles and their relation to fouling with protein containing feed streams, J. Memb. Sci. 548 (2017) 598–608. doi:10.1016/j.memsci.2017.11.048.

Chapter 5
Use of SEM to Study the Internal Flow Distribution of Asymmetric Membranes

5.1 Introduction

Membrane filtration technologies have been used extensively in a wide variety of applications for the purification of biotherapeutics, sterilization of biological products, wastewater treatment, and production of drinking water [1]. However, the performance of the membranes used in these processes can be substantially affected by membrane fouling leading to a significant decline in filtrate flux as well as a change in selectivity, reducing the membrane lifetime and capacity [2,3].

Several studies have demonstrated that the filtration performance and the rate of membrane fouling can both be significantly affected by the membrane pore structure and morphology. For example, Ho et al. [4–6] showed that the fouling characteristics of microfiltration membranes were highly dependent on both the porosity and pore connectivity of the membrane. Membranes with straight through, non-interconnected, pores had much higher rates of fouling since any pore blockage on the membrane surface led to the elimination of any flow in those pores. In contrast, membranes with highly interconnected pores allowed fluid to flow around and under any pore blockage, significantly reducing the extent of flux decline at an equivalent degree of pore blockage.

Ho and Zydney [7] developed the only published method for evaluating the pore connectivity of microporous membranes. This involved measuring the water flow rate, or diffusive solute flux, through flat sheet microfiltration membranes in which the upper and

lower surfaces of the membrane were partially blocked by “overlapping” tape. Thus, a membrane with straight through, non-interconnected, pores would have zero flow / diffusion, while membranes with highly interconnected pores would show significant transport. The rate of flow (or diffusion) was then used to evaluate the ratio of the hydraulic permeabilities in the directions parallel to and normal to the membrane surface based on a mathematical description of the velocity / pressure profiles. However, this technique cannot be applied easily to composite or asymmetric membranes since the magnitude of the flow rate will no longer be a unique function of the permeability ratio. For example, the macroporous substructure in an asymmetric membrane might be highly interconnected, while the pores in the selective skin layer could (at least in principle) have very low interconnectivity; simple measurements of the flow through the partially blocked membrane would be unable to determine the properties of this type of structure.

A number of recent studies have suggested that the membrane pore morphology also plays a significant role in determining the retention characteristics of virus filtration membranes [8–10]. For example, Woods and Zydney [11] hypothesized that the increase in virus transmission after a process disruption was due to lateral diffusion of previously captured virus within the Ultipor® DV20 membrane. This type of lateral diffusion can only occur if the pores are highly interconnected, allowing transport in the directions both parallel and perpendicular to the normal fluid flow.

The objective of the work described in this Chapter was to develop a new approach for measuring the pore interconnectivity based on direct observation of gold nanoparticles captured within a porous membrane in which the membrane exit (skin) surface was

partially blocked. Experiments were performed using Viresolve® Pro, Viresolve® NFP, and Ultipor® DV20 membranes using a mixture of different size gold nanoparticles following the procedures described in Chapter 3. The extent of pore interconnectivity was then evaluated by comparing the nanoparticle capture profiles with the calculated flow streamlines determined by numerical analysis of the flow and pressure profiles based on Darcy's law expressions in the directions normal to and parallel to the membrane surface.

5.2 Methods and Materials

5.2.1 Membranes

Experiments were performed using flat sheet, commercially-available virus filtration membranes: highly asymmetric Viresolve® Pro and Viresolve® NFP membranes provided by MilliporeSigma (Burlington, MA) and the Ultipor® DV20 membrane with a fairly homogeneous pore structure from Pall Corp. (Port Washington, NY). The Viresolve® Pro is made of polyethersulfone (PES) while the Viresolve® NFP and DV20 are both polyvinylidene difluoride (PVDF). These flat sheet membranes were cut into 47 mm disks from large sheet-stock and used in single layer format. The specifications of the membranes examined in this study are provided in Table 5.1.

Table 5.1 Properties of virus filtration membranes.

Membrane	Material	Asymmetry	Thickness (μm)	Manufacturer
Viresolve® Pro	Polyether-sulfone (PES)	Asymmetric	140	MilliporeSigma
Viresolve® NFP	Polyvinylidene fluoride (PVDF)	Highly Asymmetric	140	MilliporeSigma
Ultipor® DV20	Polyvinylidene fluoride (PVDF)	Symmetric	40	Pall

5.2.2 Nanoparticle Filtration

Membranes were placed in a 47 mm stainless steel filter holder (MilliporeSigma, Burlington, MA), with the retentive layer (shiny side) facing downstream as per the manufacture's recommendation. A stainless steel screen with a circular pattern of voids was used as a support; this screen blocked approximately 60% of the outlet surface of membrane. Experiments were conducted in normal flow filtration mode at a constant pressure of 210 kPa (30 psig) maintained by nitrogen pressurization of the feed reservoir. The membranes were initially flushed with at least 40 L/m^2 of deionized distilled water obtained from a Direct-Q® 3 UV Water Purification System (MilliporeSigma, Burlington, MA) prior to use to ensure complete wetting of the membrane and to remove any trapped air bubbles in the system.

Gold nanoparticles (20, 40, 100, and 200 nm) were obtained from MilliporeSigma (Burlington, MA) as stabilized suspensions in citrate buffer. Nanoparticle suspensions were diluted with DI water and ultrasonicated for a short time to eliminate any aggregates.

At the end of filtration, the filter was removed from the stainless steel holder, rinsed gently with DI water, and then prepared for electron microscopy as discussed below.

5.2.3 Scanning Electron Microscopy

The membranes were cut into small strips (10×3 mm) and dehydrated using progressively more concentrated ethanol solutions, beginning with 50% ethanol in water followed by 70%, 90%, and then 100% ethanol. The samples were then infiltrated with a 1:1 ratio (v/v) of 100% ethanol and LR White medium grade embedding resin (Electron Microscopy Sciences, Hartfield, PA) for one hour, followed by incubation in LR white twice, each for two hours, at room temperature. The samples were transferred to a clean snap-fit gelatin capsule (Ted Pella. Inc., Rodding, CA), which was filled with fresh LR white resin and placed in an oven at 65 °C and allowed to cure for 48 hrs. Thin slices were made through the membrane cross-section, approximately 1 µm in thickness, using a Leica EM UC6 Ultramicrotome (Leica Biosystems Inc., Buffalo Grove, IL). The slices were coated with a thin layer of iridium using an Emitech K575X sputter coater (Quorum Technologies Ltd, UK) to avoid charging when the polymeric membrane was exposed to the high energy electron beam as discussed in Chapter 3.

The membrane cross-section was examined at high-magnification using a Zeiss Sigma VP-FESEM (Carl Zeiss Microscopy, Thornwood, NY), equipped with a retractable five-diode backscattering detector, which provides high contrast between the gold nanoparticles and the sputter-coated polymeric membrane.

5.3 Theoretical Modeling

The flow distribution within the membranes was evaluated for different values of the pore connectivity by numerical solution of the Darcy flow equations:

$$V_r = -k_r \frac{\partial P}{\partial r}, \qquad V_z = -k_z \frac{\partial P}{\partial z} \tag{5.1}$$

where k_r and k_z are the Darcy permeabilities in the directions parallel to and perpendicular to the membrane surface, respectively. The velocities V_r and V_z must satisfy the continuity equation for an incompressible fluid which is given by:

$$\frac{1}{r}\frac{\partial}{\partial r}(rV_r) + \frac{\partial V_z}{\partial z} = 0 \tag{5.2}$$

Substitution of Eq. (5.1) into Eq. (5.2) yields the following partial differential equation for the local pressure:

$$\frac{k_r}{r}\frac{\partial}{\partial r}(r\frac{\partial P}{\partial r}) + k_z \frac{\partial^2 P}{\partial z} = 0 \tag{5.3}$$

As discussed earlier, due to the complex morphology of porous membranes, generally, a simple model is considered to study the fluid transport in which the membrane is modeled as an array of uniform cylindrical pores [12]. In a pressure-driven process, the fluid velocity (V) through a single cylindrical pore of the membrane can be calculated using Hagen-Poiseuille equation:

$$V = \frac{{r_p}^2 \Delta P_{TM}}{8\mu\delta_m} \tag{5.4}$$

where ΔP_{TM} is the transmembrane pressure, μ is the solution viscosity, r_p is the pore radius, and δ_m is the membrane thickness. However, the rate of fluid transport through a porous membrane containing an array of isotropic pores is analyzed by the membrane hydraulic permeability, L_p, defined as:

$$L_p = \frac{J_v}{\Delta P} = \frac{\varepsilon {r_p}^2}{8\mu\delta_m} \tag{5.5}$$

where Jv is the volumetric filtrate flux and ε is the membrane porosity (the fractional area of the membrane occupied by cylindrical pores) [12,13].

Based on Equation (5.5), the membrane hydraulic permeability is strongly dependent on the membrane pore radius. Thus, the permeability of asymmetric membranes such as Viresolve® Pro and Viesolve® NFP would be a function of pore size that varies across the membrane depth. In order to evaluate the flow streamlines within the asymmetric membranes for different values of pore interconnectivity, it is assumed that the membrane hydraulic permeability (Lp) is equal to the Darcy permeability at each depth of the membrane. Since the membrane porosity and fluid viscosity are considered constant, the only variable in the permeability equation is the pore size which is a function of membrane depth. By having the membrane pore size distribution for both Viresolve® Pro and Viresolve® NFP obtained by EDM analysis (Figure 4.2), we would be able to calculate the Darcy permeability as a function of z in the direction normal to the membrane surface. In

order to solve the differential equation derived from the Darcy's law (Eq. (5.3)), the ratio of permeability in the direction parallel to and normal to the membrane surface, K, is considered constant and independent of position. Considering this assumption simplifies the complexity of the numerical simulation in which the permeability varies based on the membrane pore size.

Equation (5.3) was solved for the system geometry shown in Figure 5.1. The dark regions are the open spaces ("holes") in the stainless steel support, with the grid defined over the region within the membrane above both the blocked and open regions. No flow boundary conditions were applied over the region covered by the stainless steel support, with symmetry conditions applied at the outer boundary of each cylindrical space above the exit space. The pressure at the upper surface of the membrane was uniform giving the following set of boundary conditions:

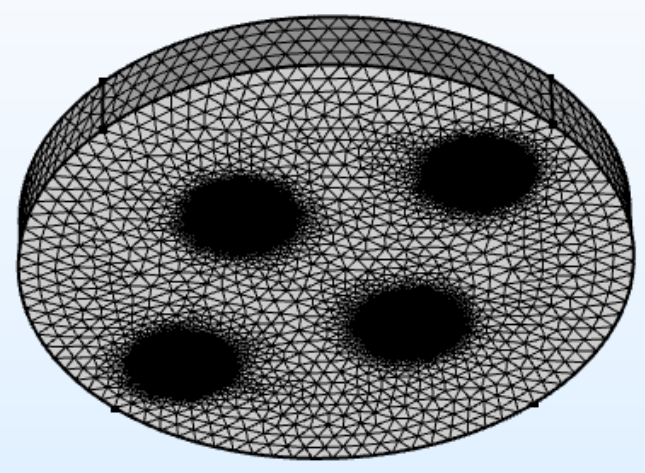

Figure 5.1 Schematic of lower surface of partially blocked membrane. Dark circles represent the open regions at the filter exit.

$$r = 0, \qquad \frac{\partial P}{\partial r} = 0 \tag{5.6}$$

$$r = \frac{L}{2}, \qquad \frac{\partial P}{\partial r} = 0 \tag{5.7}$$

$$z = \delta_m, \qquad \mathrm{P} = P_{Feed} \tag{5.8}$$

$$z = 0, \qquad \mathrm{P} = P_{Permeate} \;\; 0 \leq r \leq \frac{D}{2} \tag{5.9}$$

$$z = 0, \qquad \frac{\partial P}{\partial z} = 0 \quad \frac{D}{2} \leq r \leq \frac{L}{2} \tag{5.10}$$

$$K = \frac{k_r}{k_z} \tag{5.11}$$

where L is the center-to-center distance between two adjacent exit regions and D is the diameter of each open area. The permeability ratio K = $\frac{k_r}{k_z}$ was assumed to be constant throughout the membrane: $K = 0$ corresponds to a membrane with non-interconnected pores (no lateral flow) while $K = 1$ corresponds to a membrane with a homogeneous (isotropic) structure with equal resistance to flow in both directions.

Equations (5.3) to (5.10) were solved numerically using the finite element analysis in COMSOL Multiphysics software (version 5.3) for different values of the pore connectivity. The resulting pressure values were then used to evaluate the local velocity

profiles using Eq. (5.1), with the flow streamlines calculated based on the numerical results for V_r and V_z.

The predicted distribution of captured nanoparticles within the membrane was evaluated as follows. The membrane was "challenged" with a feed containing a distribution of nanoparticles (described by a simple Gaussian function). Each nanoparticle was released at a different location and assumed to follow the flow streamline until it reached a point within the depth of the membrane where the local pore size first became equal to the particle size; the pore size profile for the Viresolve® Pro and NFP membranes are given in Figure 4.2 in Chapter 4. A total number of 100,000 nanoparticles were placed at the entrance of the filter (z = 140 μm) and distributed based on the magnitude of the local flow velocity. It was assumed that nanoparticle capture has no affect on the membrane pore size distribution and that there was no interference between particles. Subsequently, the nanoparticles were carried by flow streamlines, which was obtained by Darcy local velocities, to the membrane pores.

5.4 Result and Discussion

5.4.1 Viresolve® Pro Membrane

Figure 5.2 shows optical images of two Viresolve® Pro membranes after filtration of a suspension of gold nanoparticles with membrane shiny-side (retentive layer) placed on either a stainless steel screen (left panel) or a 20 μm pore size microfiltration membrane (right panel), both used as spacers beneath the membrane in the stainless steel holder. The

dark red color shows the captured gold nanoparticles. The image of membrane on the stainless steel screen shows a regular array of red dots, representing regions with permeate flow (over the open region of the screen) and where the flow was blocked (white areas above the solid portion of the screen). In contrast, a uniform distribution of nanoparticles was seen over the entire surface of Viresovle® Pro membrane when used on the microfiltration membrane (at resolution by eye). The reduction in the effective area of the membrane caused by the screen was also reflected in the much lower measured permeability of the membrane. In the case of the Viresolve® Pro membrane, the flux through the clean membrane at a pressure of 210 kPa (30 psig) decreased by more than a factor of 4, from 1150 $L/m^2/h$ for the membrane on the microfiltration support to only 260 $L/m^2/h$ for the membrane on the stainless steel screen. The image in Figure 5.2 and the permeability data both suggest that approximately 60% of the membrane area was blocked by the screen.

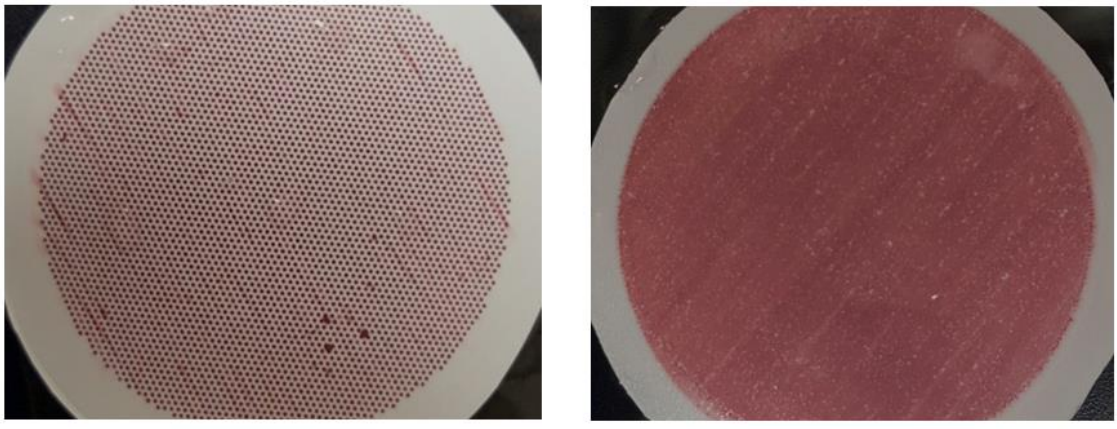

Figure 5.2 Optical images of the membrane lower surface challenged with gold nanoparticles placed on stainless steel screen (left panel) and on a microfiltration membrane support (right panel).

Figure 5.3 shows an SEM image of the cross-section through the Viresolve® Pro membrane, focusing on the region immediately above the boundary between the open and blocked regions of the stainless steel support. The membrane was challenged at a constant pressure of 210 kPa (30 psig) with a suspension containing a mixture of the 20, 40, 100, and 200 nm gold nanoparticles, with mean size of 25 ± 8 nm, 42 ± 12 nm, 100 ± 30 nm, and 200 ± 45, respectively. The SEM image shows distinct "bands" for the different size nanoparticles, with the 20 nm particles captured right near the filter exit while the 200 nm nanoparticles are captured around 25 μm into the depth of the filter (similar to the results discussed in Chapter 3). More strikingly, the bands for the larger particles are spread out into the space above the blocked region of the membrane, with the "span" for the band increasing as the size of the nanoparticle increases. The net result is that the inner edge of the bands generates a curve (shown in red) that defines the capture profile within the Viresolve® Pro membrane; the shape of this curve is determined by the extent of lateral flow within this region of the membrane.

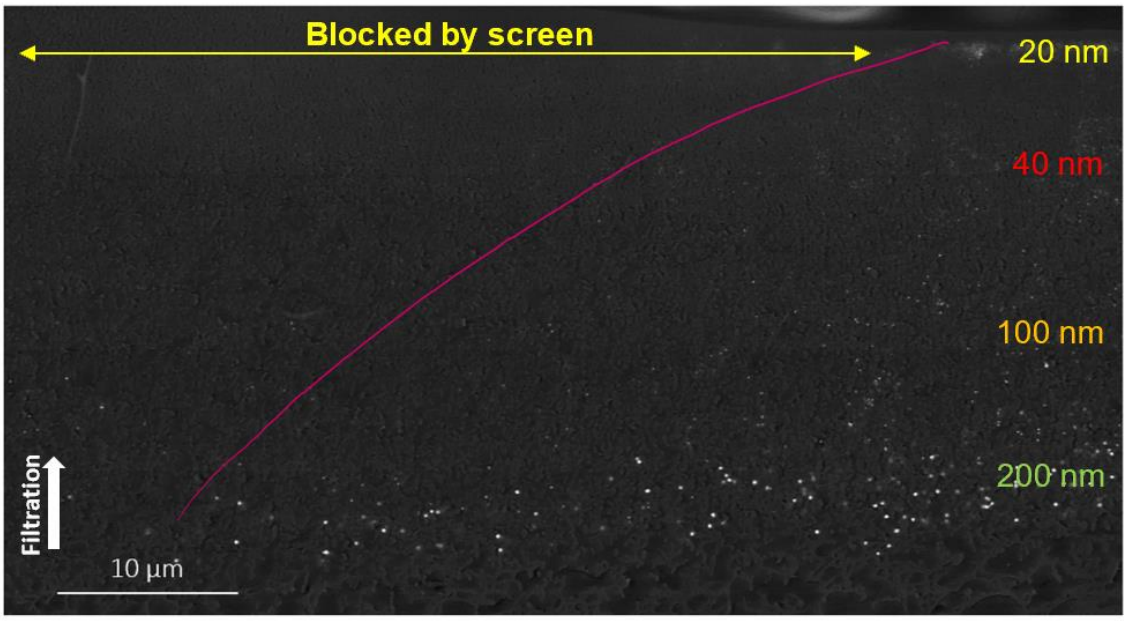

Figure 5.3 High contrast SEM image of the cross-section of a Viresolve® Pro membrane challenged with 60 L/m^2 of a suspension containing 20, 40, 100 and 200 nm gold nanoparticles at 210 kPa with the skin side placed on top of the stainless steel screen spacer.

The calculated values of the flow streamlines within the Viresolve® Pro membrane were evaluated numerically using COMSOL Multiphysics software for different values of the pore connectivity: K = 1, 0.1, 0.01, with results shown in Figure 5.4. At the smallest value of K, the streamlines are directed almost perpendicular to the feed / permeate surfaces of the membrane, similar to what would be expected for flow through a membrane with straight-through non-interconnected pores, with essentially no bulk flow through the regions upstream of the blocked surface. As K increases, the streamlines begin to move out into the portion of the membrane above the blocked region due to the increase in the lateral flow through the porous membrane (similar to the profile for the gold nanoparticles seen in Figure 5.3). For K = 1, there is a measurable flow over almost the entire entrance to the membrane even though more than 60% of the exit region is blocked by the stainless steel screen.

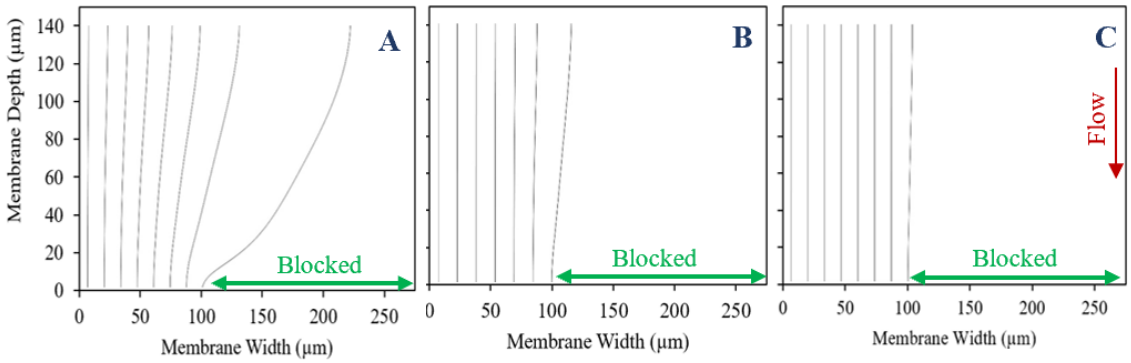

Figure 5.4 Internal flow streamlines within the Viresolve® Pro membrane for (A) K=1, (B) K= 0.1, and (C) K=0.01.

The positions of individual gold nanoparticles retained within the membrane were quantified using ImageJ software. The distribution of gold nanoparticles obtained by SEM images analysis demonstrating the trajectory of internal flow upstream of blocked and open regions contact point.

The best fit value of K for the Viresolve® Pro membrane was estimated (qualitatively) by comparison of the nanoparticle capture profile shown in Figure 5.3 with the calculated streamlines shown in Figure 5.4. First, the positions of the individual gold nanoparticles retained with the membrane were determined using ImageJ software and plotted in Figure 5.5, with each particle shown by a red circle (irrespective of the particle size). The particles were "aligned" with the outer boundary of the open region based on the location of the 20 nm particles that are captured immediately upstream of the retentive skin. The flow streamlines were then overlaid on the same plot, with the results for K = 1 shown in Figure 5.5. The shape of the calculated streamlines is well-aligned with the particle capture zone using K = 1, suggesting that this value of K provides a reasonable estimate of the pore interconnectivity for the Viresolve® Pro membrane. Note that there were

significant discrepancies between the location of the flow streamlines and the nanoparticle capture profiles when performing this analysis using either smaller, or larger, values of K.

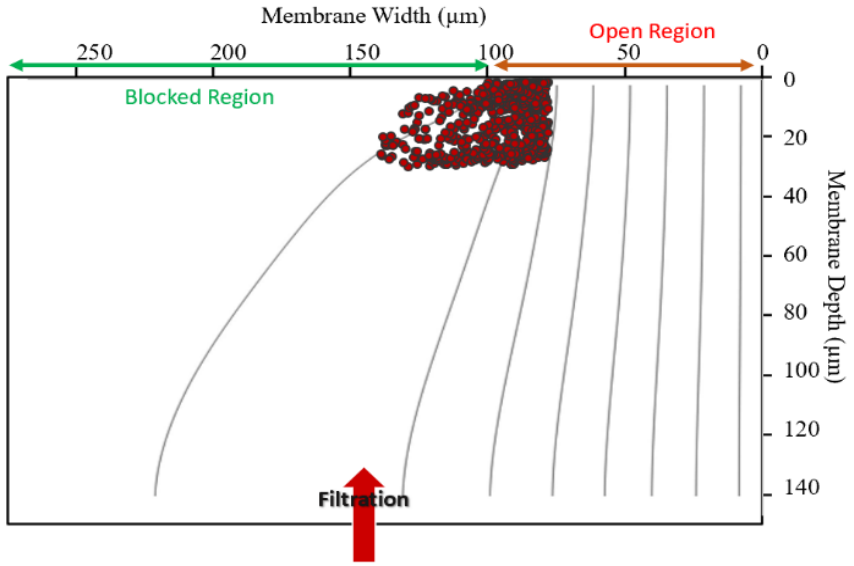

Figure 5.5 Comparison of captured nanoparticles within the Viresolve® Pro membrane (determined by ImageJ software) and calculated streamlines from solution of Equation (5.3) using K=1.

A more quantitative analysis of the pore interconnectivity in the Viresolve® Pro membrane was performed by simulating the nanoparticle capture in MATLAB using the velocities calculated in COMSOL for specific values of K. The membranes were "challenged" with a distribution of particles, in this case defined by a mixture of particles with mean size of 20, 40, 100, and 200 nm having standard deviations of 4, 6, 10, and 15 nm, respectively. Each particle was captured at a location (z-value) at which the local membrane pore size was equal to the size of the nanoparticle. The resulting simulation results are shown in Figure 5.6, with each panel showing the behavior with a different value of K. As K increases, the nanoparticles are captured in a more diffuse band spreading out over the blocked region of the membrane. Again, the best agreement between the observed

and simulated nanoparticle capture was obtained using K = 1; simulations with smaller values of K gave nanoparticle profiles that remained too focused over the open region of the membrane.

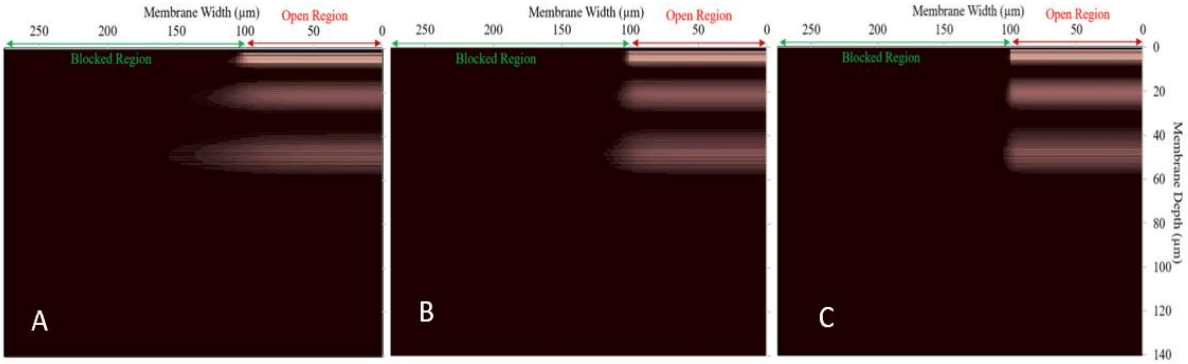

Figure 5.6 Simulation of different size nanoparticles (20, 40, 100, and 200 nm) captured within the Viresolve® Pro membrane for (A) K=1, (B) K= 0.1, and (C) K=0.01.

5.4.2 Viresolve® NFP Membrane

Corresponding results for the Viresolve® NFP membrane are shown in Figures 5.7 to 5.9. The top panel of Figure 5.7 shows an SEM image after filtration of a mixture containing 20, 40, 100, and 200 nm gold particles at a constant pressure of 210 kPa (30 psig). The 20 nm gold particles are captured very close to the membrane exit (skin layer) over the open region of the stainless steel support. The 40 and 100 nm particles were captured in bands that are mostly above the open region but do extend slightly into the space above the blocked region. In contrast, the 200 nm particles are scattered throughout the depth of the membrane over both the open and blocked flow regions, reflecting the nearly uniform pore size in the microporous support on which the Viresolve® NFP is case.

The bottom panel of Figure 5.7 shows the distribution of captured nanoparticles obtained by ImageJ analysis; the software is able to identify the individual particles much more effectively by properly adjusting the threshold limits. Again, the nanoparticles are "aligned" with the open region on the membrane based on the location of the "last" 20 nm particle visible in the SEM image. The furthest most nanoparticle seen in the ImageJ output is located 12 μm to the left of the open region, reflecting the small amount of lateral flow within the Viresolve® NFP membrane.

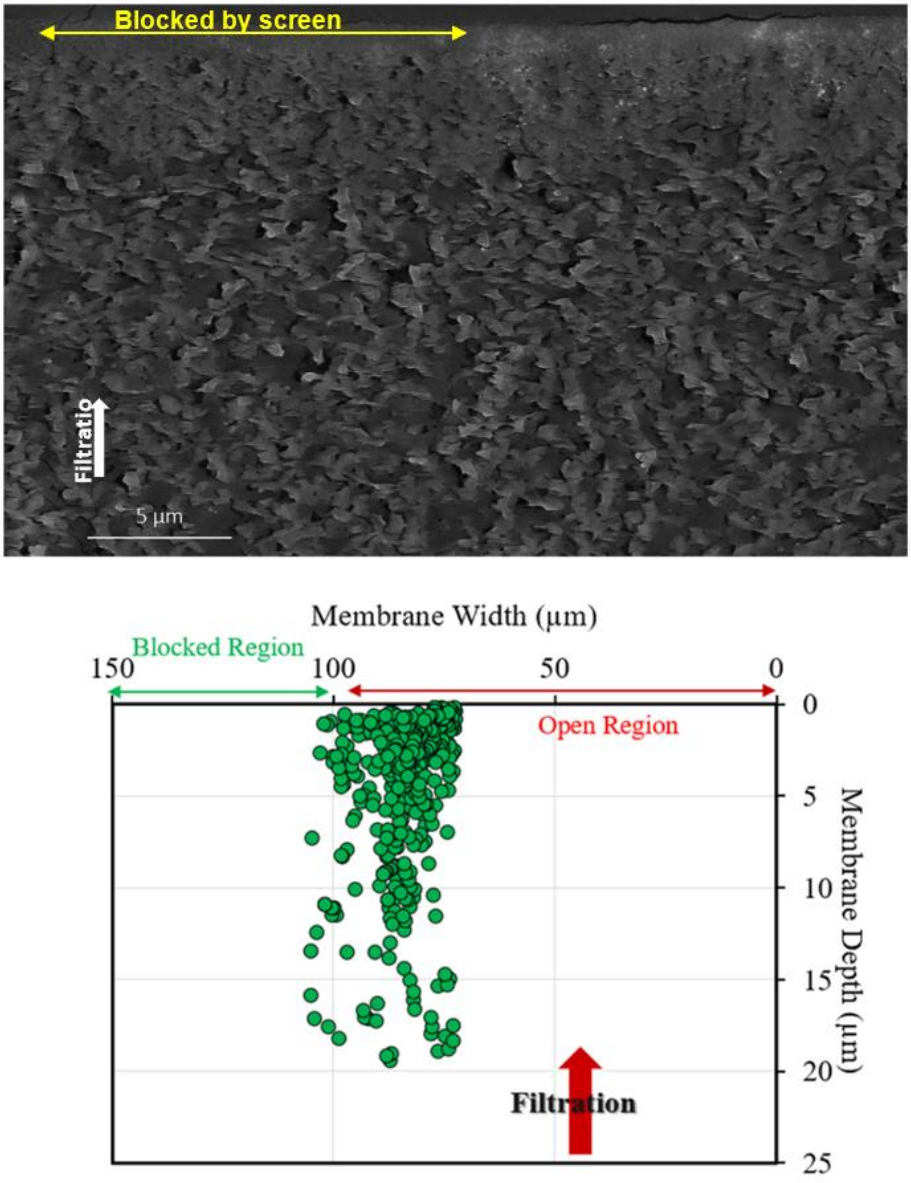

Figure 5.7 High contrast SEM image of the cross-section of a Viresolve® NFP membrane challenged with 60 L/m^2 of a suspension containing 20, 40, 100 and 200 nm gold nanoparticles at 210 kPa with the skin side placed on top of the stainless steel screen spacer (top panel). The distribution of captured nanoparticles (in green circles) within Viresovle® NFP membrane near the retentive layer as determined by ImageJ software (bottom panel).

Figure 5.8 shows the calculated flow streamlines in the Viresolve® NFP for K =1, 0.1, 0.01, and 0.001. As expected, the flow bends out further into the space above the

blocked region as K increases, with the streamlines for K = 0.001 remaining almost entirely over the open region of the membrane. The flow streamlines for K =0.01 are shown in an overlay with the ImageJ results for the nanoparticle capture in the left-hand panel of Figure 5.9. Although there is some discrepancy between the streamlines and the particle profile, the data are in fairly good agreement with K = 0.01 (or smaller), which is two orders of magnitude smaller than the value of the pore interconnectivity determined for the Viresolve® Pro membrane.

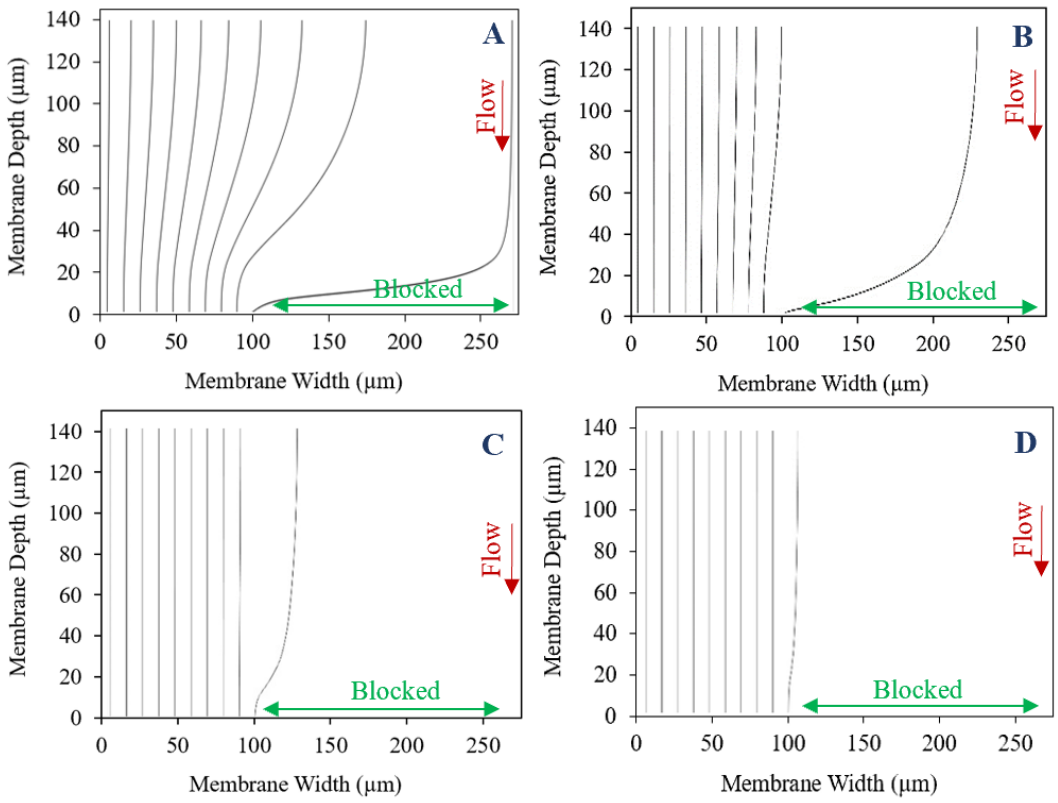

Figure 5.8 Internal flow streamlines within the Viresolve® NFP membranes for (A) K=1, (B) K= 0.1, (C) K=0.01, (D) K=0.001.

As described earlier, a MATLAB simulation was performed to evaluate the capture location of different size nanoparticles within the Viresolve® NFP membrane based on the

previously calculated velocity profiles. The pore size at each location within the depth of the filter was evaluated from EDM measurements (shown in Figure 4.2). The simulation results using K = 0.01 are in good agreement with the ImageJ picture of nanoparticle capture, providing further confirmation that this value of K gives an appropriate measure of the pore interconnectivity within the Viresolve® NFP membrane.

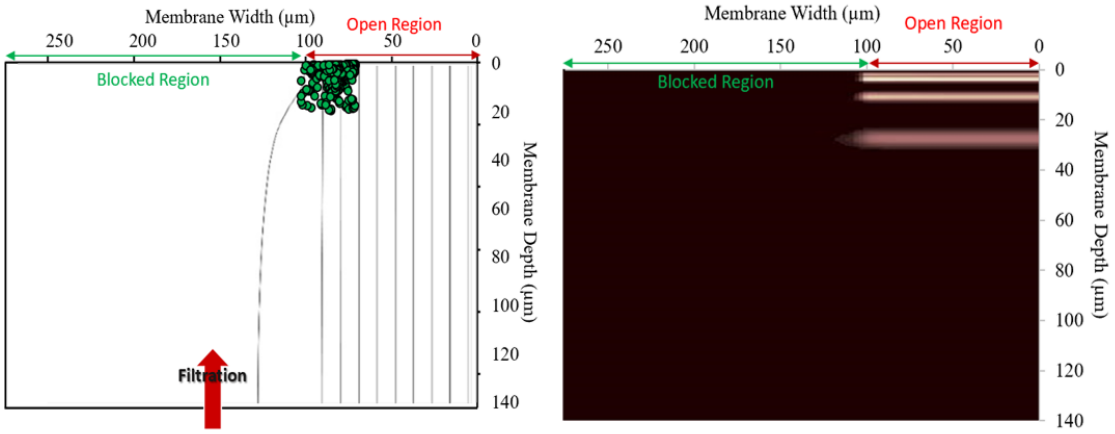

Figure 5.9 Profiles of captured nanoparticles within the Viresolve® NFP membrane determined from flow streamlines (left panel) and nanoparticle simulations (right panel) both with K = 0.01.

5.4.3 Ultipor® DV20 Membrane

In contrast to the Viresolve® Pro and Viresolve® NFP membranes, the Ultipor® DV20 membrane has a fairly uniform pore size throughout the depth of the 40 µm thick membrane; only a slight asymmetry was observed using dextran sieving measurements [3] and the capture of fluorescent nanoparticles (images in Chapter 2). Figure 5.10 shows an SEM image of the cross-section through a DV20 membrane after challenging with the nanoparticle mixture following the same procedures as used for the Viresolve® Pro and NFP membranes. However, in this case, all of the nanoparticles were captured near the

filter inlet, opposite the blockage by the stainless steel support, with the 20 and 40 nm particles penetrating about 2-3 μm into the depth of the membrane. However, the nanoparticles were only observed at distinct locations on the membrane surface, consistent with the circular pattern of open spaces defined by the stainless steel support located beneath the membrane (at the membrane exit). The lack of any particles over the "blocked" regions of the membrane is consistent with the absence of any significant pore interconnectivity in the DV20 membrane.

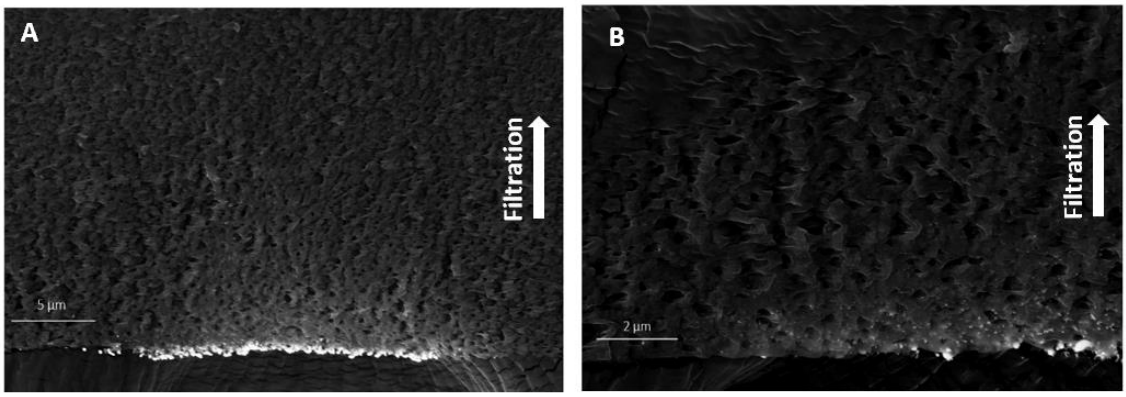

Figure 5.10 High contrast SEM image of the cross-section of an Ultipor® DV20 membrane challenged with 60 L/m^2 of a suspension containing 20, 40, 100 and 200 nm gold nanoparticles at 210 kPa showing the nanoparticles capture near the filter entrance (lower surface). Images show: (A) Low magnification, (B) High magnification.

Figure 5.11 shows the calculated streamlines for the DV20 membrane for the different values of the pore interconnectivity. The streamlines with K = 1 extend across most of the entrance region to the filter, in sharp contrast to the nanoparticle capture profiles in Figure 5.10. The results suggest that the best fit value of K for the DV20 membrane is less than 0.001; simulations with larger values of K show significantly more spreading of the flow than would be suggested based on the nanoparticle capture.

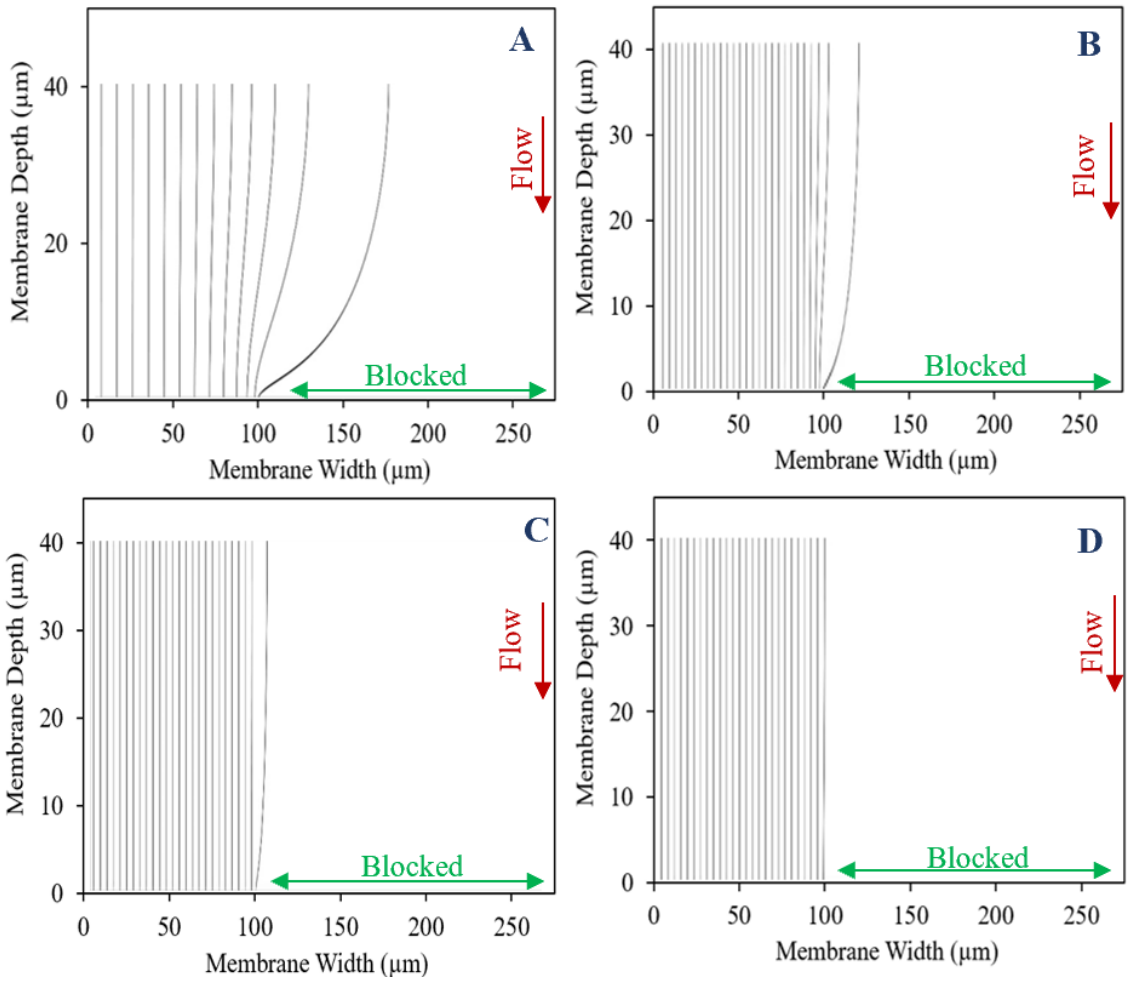

Figure 5.11 Internal flow streamlines within the Ultipor® DV20 membrane for (A) K=1, (B) K= 0.1, (C) K=0.01 and (D) K=0.001.

In order to confirm the very low degree of lateral flow within the DV20 membrane, an independent measure of the pore interconnectivity was obtained following the general approach described by Ho and Zydney [7]. A DV20 membrane was first flushed with water to fully wet the pores, with the permeability evaluated as 1.1×10^{-10} m based on the flow rate at 210 kPa (30 psig). The top and bottom surfaces of the membrane were then partially covered with tape, with the two taped sections overlapping by approximately 1 mm. The

membrane was then placed in the base of a stirred cell which was re-pressurized to 210 kPa (30 psig). No measurable filtrate flux was observed after 180 minutes of filtration, corresponding to a permeability of less than 2×10^{-16} m based on the approximate volume of one drop of water. This low a permeability would correspond to $K < 0.001$ based on the model calculations, in good agreement with the results obtained from the gold nanoparticles, providing further confirmation of this methodology.

5.5 Conclusions

The work described in this Chapter presents a new method for evaluating the pore interconnectivity in virus filtration membranes based on the capture profiles for different size gold nanoparticles as visualized by scanning electron microscopy. The membranes were used with the skin-side placed directly on top of a stainless steel spacer that blocked a significant fraction of the pores in the membrane skin (filter exit), forcing the fluid flow to exit the membrane only through the open (unblocked) regions. The "blocked" membrane was then challenged with a mixture of gold nanoparticles, with the location of the captured nanoparticles providing a picture of the flow streamlines within the interior of the membrane.

Experiments performed with the Ultipor® DV20 membrane showed particles captured on the upper (inlet) surface of the membrane, but only over the regions of the membrane that were open on the downstream (exit) surface. This clearly indicates that the flow streamlines in the DV20 membrane must be directed almost perpendicular to the membrane surface, with minimal lateral flow. The very low degree of pore

interconnectivity in the DV20 membrane was confirmed using the "overlapping tape" method described previously by Ho and Zydney for symmetric (homogeneous) microfiltration membranes, with no measurable permeability (flow) when the tape on the upper and lower surfaces of the membrane overlap. However, the "overlapping tape" method cannot be used with highly asymmetric virus filtration membranes since the high degree of pore interconnectivity in the membrane support structure will obscure the effects of the interconnectivity in / near the membrane skin, which is the region of interest in understanding the performance characteristics of these virus filters.

The nanoparticle capture profiles obtained with the highly asymmetric Viresolve® Pro membrane show a significant spreading of the nanoparticles over the blocked regions as one moves further into the depth of the membrane, i.e., as the size of the nanoparticles increase. The shape of the nanoparticle capture profile was used to calculate the pore interconnectivity using a numerical analysis of the flow streamlines and predicted nanoparticle capture within the membrane. Images for the Viresolve® Pro were well described by a permeability ratio, $K = \frac{k_r}{k_z} = 1$, consistent with a high degree of lateral flow within the membrane. In contrast, the nanoparticle capture profiles in the Viresolve® NFP were best fit using K = 0.01, indicating that the permeability in the direction normal to the membrane surface is much larger than that in the transverse direction.

The potential impact of these differences in pore interconnectivity on protein fouling of the virus filtration membranes is discussed in Chapter 6. In addition, it is important to note that the Viresolve® NFP and Ultipor® DV20 membranes, both with low pore interconnectivities, show a significant loss in virus retention after a process disruption

[11,14]. In contrast, the Viresolve® Pro, which has a high pore interconnectivity, shows highly robust virus retention in response to a process disruption and to extensive membrane fouling. The connection between the pore interconnectivity and the virus retention characteristics of these different virus filters is beyond the scope of this work. However, the results presented in this Chapter clearly demonstrate the potential of using nanoparticle capture profiles to obtain quantitative estimates of the membrane pore interconnectivity, even for highly asymmetric membranes like those used for virus filtration.

5.6 Notation

δ_m	Membrane thickness (m)
D	Open region diameter (m)
K	Permeability ratio
k	Darcy permeability in membrane (m^3 s/kg)
L	Membrane width (m)
P	Local hydrostatic pressure (N/m^2)
P_{feed}	Feed pressure (N/m^2)
$P_{permeate}$	Filtrate pressure (N/m^2)
V	Fluid velocity (m/s)
μ	Solution viscosity (N s/m^2)
ΔP_{TM}	Transmembrane pressure (N/m^2)
r_p	Membrane pore radius (m)
L_p	Hydraulic permeability (m^3/N s)
ε	Membrane porosity
J_v	Filtrate flux (m/s)

5.7 Subscripts

r	direction parallel to membrane surface
z	direction normal to membrane surface

5.8 Literature Cited

[1] R. van Reis, A. Zydney, Bioprocess membrane technology, J. Memb. Sci. 297 (2007) 16–50. doi:10.1016/j.memsci.2007.02.045.

[2] A.D. Marshall, P.A. Munro, G. Trägårdh, The effect of protein fouling in microfiltration and ultrafiltration on permeate flux, protein retention and selectivity: A literature review, Desalination. 91 (1993) 65–108. doi:10.1016/0011-9164(93)80047-Q.

[3] M. Bakhshayeshi, A.L. Zydney, Effect of solution pH on protein transmission and membrane capacity during virus filtration, Biotechnol. Bioeng. 100 (2008) 108–117. doi:10.1002/bit.21735.

[4] C.C. Ho, A.L. Zydney, Protein fouling of asymmetric and composite microfiltration membranes, Ind. Eng. Chem. Res. 40 (2001) 1412–1421. doi:10.1021/ie000810j.

[5] C.C. Ho, A.L. Zydney, Effect of membrane morphology on the initial rate of protein fouling during microfiltration, J. Memb. Sci. 155 (1999) 261–275. doi:10.1016/S0376-7388(98)00324-X.

[6] C.C. Ho, A.L. Zydney, Theoretical analysis of the effect of membrane morphology on fouling during microfiltration, Sep. Sci. Technol. 34 (1999) 2461–2483. doi:10.1081/SS-100100785.

[7] C.C. Ho, A.L. Zydney, Measurement of membrane pore interconnectivity, J. Memb. Sci. 170 (2000) 101–112. doi:10.1016/S0376-7388(99)00360-9.

[8] F. Fallahianbijan, S. Giglia, C. Carbrello, A.L. Zydney, Use of fluorescently-labeled nanoparticles to study pore morphology and virus capture in virus filtration membranes, J. Memb. Sci. 536 (2017) 52–58. doi:10.1016/j.memsci.2017.04.066.

[9] H. Nazem-Bokaee, F. Fallahianbijan, D. Chen, S.M. O'Donnell, C. Carbrello, S. Giglia, D. Bell, A.L. Zydney, Probing pore structure of virus filters using scanning electron microscopy with gold nanoparticles, J. Memb. Sci. 552 (2018) 144–152. doi:10.1016/j.memsci.2018.01.069.

[10] M. Bakhshayeshi, N. Jackson, R. Kuriyel, A. Mehta, R. van Reis, A.L. Zydney, Use of confocal scanning laser microscopy to study virus retention during virus filtration, J. Memb. Sci. 379 (2011) 260–267. doi:10.1016/j.memsci.2011.05.069.

[11] M.A. Woods, A.L. Zydney, Effects of a pressure release on virus retention with the Ultipor DV20 membrane, Biotechnol. Bioeng. 111 (2014) 545–551. doi:10.1002/bit.25112.

[12] L.J. Zeman, A. Zydney, Microfiltration and ultrafiltration : Principles and applications, CRC Press, 2017.

[13] S. Mochizuki, A.L. Zydney, Theoretical analysis of pore size distribution effects on membrane transport, J. Memb. Sci. 82 (1993) 211–227.

[14] S.K. Dishari, A. Venkiteshwaran, A.L. Zydney, Probing effects of pressure release on virus capture during virus filtration using confocal microscopy, Biotechnol. Bioeng. 112 (2015) 2115–2122. doi:10.1002/bit.25614.

Chapter 6
Effect of Transmembrane Pressure on the Fouling Behavior of Virus Filters

6.1 Introduction

Virus filtration has been widely used as an essential part of the downstream purification process during the manufacture of protein-based biotherapeutics derived from mammalian cell lines or blood plasma [1–3]. Virus filtration membranes can achieve very high removal of both enveloped and nonenveloped viruses regardless of their chemical or surface properties [4,5]. Virus filtration is usually performed in normal flow operation with the membrane designed to provide high transmission / recovery of the therapeutic protein in the collected permeate [6]. However, the pores in the retentive layer of the membrane are only slightly larger than the size of the proteins, which can lead to significant issues with membrane fouling, altering both the capacity and retention characteristics of the membrane.

Several studies have examined the effects of operating conditions on the fouling characteristics of different virus filtration membranes. For example, Syedain et al. [7] evaluated the effect of transmembrane pressure on protein fouling of the Viresolve® 180 membrane using 1 g/L solutions of cysteinylated bovine serum albumin (cys-BSA). Data obtained with the membrane skin-layer facing downstream gave a capacity (volumetric throughput at a given percentage flux decline) that was essentially independent of the transmembrane pressure. However, the capacity decreased dramatically at high transmembrane pressure when the filtration was performed with the skin-side up [7].

Bakhshayeshi studied the filtration of BSA solutions with concentrations of 1 and 8 g/L through the DV20 virus filtration membrane. The volumetric capacity of the DV20 membrane using 8 g/L BSA was independent of the transmembrane pressure, whereas the capacity increased significantly with increasing pressure for the 1 g/L BSA [8]. No detailed explanation for the different effects of pressure on the fouling of the different concentration BSA solutions was provided.

It has also been reported previously that the use of inline adsorptive or size-based prefilters can improve the performance of virus filtration membranes by removing large protein aggregates thereby reducing the extent of fouling [9–11]. Bolton et al. have shown that implementation of a prefilter that contains diatomaceous earth eliminated absorptive foulants significantly increasing the capacity of virus filtration membranes [9]. A subsequent study showed that the Viresolve^{TM} Prefilter, which also has entrapped diatomaceous earth to bind hydrophobic species, provided a dramatic increase in the capacity of the Viresolve® NFP virus filter during filtration of human IgG or a variety of monoclonal antibodies [12]. Additionally, Brown et. al found that ion exchange membranes could be used as inline pre-filters to improve the throughput of monoclonal antibodies (mAbs) during virus filtration due to the removal of high molecular weight species ranging from 8 to 13 nm in hydrodynamic radius [10]. In contrast, Hamamoto et al. found that irreversible IgG adsorption and conformational changes in IgG molecules were the major factors causing flux decline and membrane fouling during filtration through cellulose-based hollow fiber virus filters [13].

Although these studies provide important insights into the fouling characteristics of different commercially available virus filters, there is currently no fundamental understanding of the effects of pressure or protein characteristics on the underlying fouling mechanisms or their relationship to the membrane structure. The objective of the work described in this Chapter was to quantify the impact of operating pressure on the fouling behavior of the Viresolve® Pro and Viresolve® NFP membranes. Experiments were performed using bovine serum albumin (BSA) and Immunoglobulin G (IgG) as model proteins; limited data were also obtained using nanoparticle suspensions. In addition, the cross-sections of the fouled membranes were observed using both confocal laser scanning microscopy and scanning electron microscopy to determine the location of the deposited foulants within the membrane.

6.2 Materials and Methods

6.2.1 Virus Filters

Filtration experiments were conducted using Viresolve® Pro and Viresolve® NFP parvovirus-retentive membranes provided by MilliporeSigma (Burlington, MA). Both membranes are highly asymmetric, with the flow directed in through the more open pore region so that the highly selective skin is located at the filter exit. The Viresolve® Pro membrane is made from polyethersulfone (PES), while the Viresolve® NFP membrane is polyvinylidene difluoride (PVDF). Small 47 mm membrane disks were cut from large sheet-stock and used in single layer format to facilitate imaging; commercial devices

employ multiple layers of membrane (two layers for the Viresolve® Pro and three layers for the Viresolve® NFP) to obtain the high levels of virus removal required in bioprocessing applications.

6.2.2 Solution Preparation

Phosphate buffer solutions were prepared by dissolving 0.03 M Na_2HPO_4 and 0.03 M KH_2PO_4 (both from MilliporeSigma, Burlington, MA) in deionized distilled water obtained from a Direct-Q® 3 UV Water Purification System (MilliporeSigma) with resistivity greater than 18 MΩ cm. The buffer pH was determined using a model 420Aplus Thermo Orion pH meter (Orion Technology, Beverly, MA) and adjusted to 7.2 by adding small quantities of 1 M NaOH (J.T. Baker) as needed. Buffer solutions were pre-filtered through 0.2 μm pore-size Supor®-200 membranes (Pall Corp., Ann Arbor, MI) to remove any particles or undissolved salts prior to use.

Human serum immunoglobulin G (IgG, SeraCare Life Sciences, Milford, MA, Product Number HS-470) and bovine serum albumin (BSA, Sigma A2153) were used as model proteins. IgG and BSA solutions were prepared fresh for each experiment by dissolving the appropriate amount of powdered protein in phosphate buffer at room temperature. In order to remove insoluble aggregates, all protein solutions were filtered through 0.2 μm syringe filters (VWR 28145-487) immediately prior to performing the virus filtration experiments. Protein concentrations were determined using a NanoDrop™ 2000 (Thermo Scientific, Wilmington, DE) UV-Vis spectrophotometer, with the absorbance measured at 280 nm.

For the confocal microscopy, the IgG was first labeled with Alexa Fluor® 647 (A20173) labeling kit, obtained from Molecular Probes, Inc. (Eugene, OR). The labeling protocol was provided by Molecular Probes; the reaction involves the ester moiety of the dye and the free amine groups on the protein. The conjugation occurs at pH greater than 8; thus, 1 M sodium bicarbonate buffer was added to 0.5 mL of a 2 g/L IgG solution to raise the pH to 8.3. The resulting protein solution was transferred to one vial of Alexa Fluor dye and stirred for 2 hrs at room temperature. The labeled IgG was separated from the unreacted dye using a Bio-Rad Bio-Gel® P-30 fine size exclusion resin; the purified fluorescently labeled IgG was stored at 4 °C in the dark.

Gold nanoparticles used in the SEM analysis were obtained from MilliporeSigma (Burlington, MA) as stabilized suspensions in citrate buffer. The properties of the gold nanoparticles are provided in Chapter 3. Aliquots from the stock solution of nanoparticles were diluted in phosphate buffer to obtain the desired concentration and then ultrasonicated to break up any nanoparticle aggregates.

6.2.3 Protein / Nanoparticle Filtration

All filtration experiments were conducted using a 47 mm stainless steel filter holder (MilliporeSigma), with the virus membrane oriented with the skin (shiny) side down as per the manufacturer's recommendation. The virus membrane was supported on a large pore size (20 μm) membrane with high permeability. Experiments were performed in normal flow filtration mode at constant pressure, which was maintained by nitrogen pressurization of the feed reservoir. The membranes were initially flushed with at least 40 L/m^2 of buffer

to ensure complete wetting and to eliminate any air bubbles trapped in the system. The feed reservoir was then refilled with the protein or nanoparticle solution, the transmembrane pressure reapplied, and the filtrate flow rate evaluated as a function of time by timed collection. After completion of the filtration experiment, the membrane was removed from the holder, rinsed gently with DI water, and prepared for imaging.

6.2.4 Confocal Scanning Laser Microscopy

Membranes challenged with fluorescently labeled protein were prepared by mounting a small piece (about 1 cm × 1 cm) directly on a glass slide or by cutting the membrane in cross-section using a cryostat microtome (Leica model CM1950) as described in Chapter 2. The samples were covered by a drop of ProLong Gold Antifade Mountant obtained from Molecular Probes, Inc. (Eugene, OR) and cured for 48 hr at room temperature to protect the fluorescent dyes from fading during confocal imaging by the Olympus Fluoview™ 1000 confocal laser scanning microscope (Olympus American Inc., New Jersey). The Alexa Fluor 647 dye was excited with a 633 nm (red) laser. The emitted fluorescent light was collected through a 60x or 100x oil objective lens. A confocal image was generated through the depth of the filter by stacking multiple x-y optical sections obtained at 0.5 μm intervals using the Olympus Fluoview™ software. A fluorescent image of the cryo-sectioned membrane cross-section was obtained by simple scanning.

6.2.5 Scanning Electron Microscopy

Membranes challenged with gold nanoparticles were imaged at high-magnification using a Zeiss Sigma VP-FESEM (Carl Zeiss Microscopy, Thornwood, NY, US) equipped with a retractable five-diode backscattered detector. This provided high contrast between the gold nanoparticles and the sputter-coated membrane. Additional details on the sample preparation are available in Chapter 3.

6.2.6 Size Exclusion Chromatography (SEC)

BSA and IgG solutions were characterized by size exclusion chromatography using an Agilent 1200 HPLC system (Agilent Technologies, Palo Alto, CA) with a pre-packed Superdex 200 column (GE Healthcare, Uppsala, Sweden). Injection volume was 80 μL and phosphate buffer was used as the mobile phase at a flow rate of 0.5 mL/min at 25 °C. Protein detection was by UV absorbance at 280 nm.

Limited filtration experiments were performed with protein samples that were depleted in dimers and higher order oligomers. These IgG solutions were prepared by size exclusion column using an AKTA Pure chromatography system (GE Healthcare, Uppsala, Sweden) available in the CSL Behring Fermentation Facility at Penn State. 1 mL of a 10 g/L IgG solution was injected manually into the column using a 1 mL loop. The fractions associated with the IgG monomer were collected manually from the exit of the SEC column based on the previously determined elution volume. The preparative SEC was run multiple times to obtain sufficient volume of the “monomeric IgG” for use in the virus filtration

experiment. The pooled IgG from the SEC was stored at 4 ^{o}C and used less than 24 hr of preparation to minimize reaggregation.

6.3 Results and Discussion

6.3.1 Viresolve® Pro Membrane

Figure 6.1 shows the normalized filtrate flux as a function of the volumetric throughput during filtration of 1 g/L solutions of IgG through the Viresolve® Pro membranes with the skin-side (retentive layer) facing downstream. The initial membrane permeability was evaluated prior to protein filtration using protein-free buffer, with values of $9.0\pm0.2\times10^{-13}$ m for all membranes examined in this Chapter. Experiments were performed at constant transmembrane pressures of 15 psi (105 kPa), 30 psi (210 kPa), and 45 psi (315 kPa). The dashed line represents the membrane capacity, defined as the volumetric throughput when the flux drops by 80% compared to the initial buffer flux. The rate of flux decline was much faster at the lowest transmembrane pressure, with the capacity at 45 psi (40 L/m^2) approximately twice that at 15 psi (20 L/m^2).

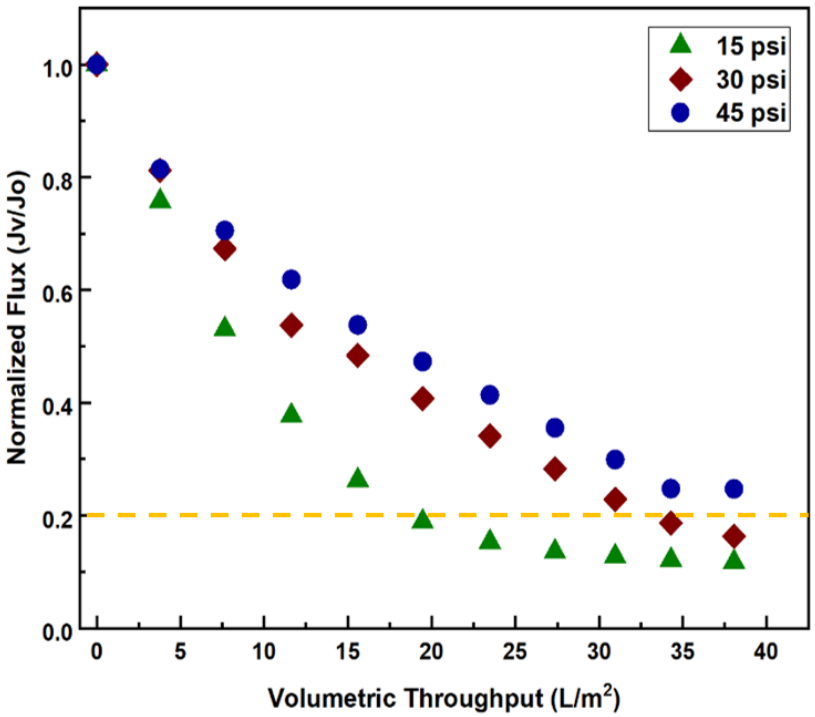

Figure 6.1 Normalized filtrate flux as a function of protein volumetric throughput for filtration of 1 g/L IgG solutions through Viresolve® Pro membranes at constant transmembrane pressures of 15, 30, and 45 psi.

Figure 6.2 shows the corresponding data for the IgG concentrations in the filtrate during the protein filtration. The IgG concentrations were 0.96 ± 0.02 g/L throughout each of the filtration experiments, indicating high transmission of IgG through the Viresolve® Pro membrane as desired.

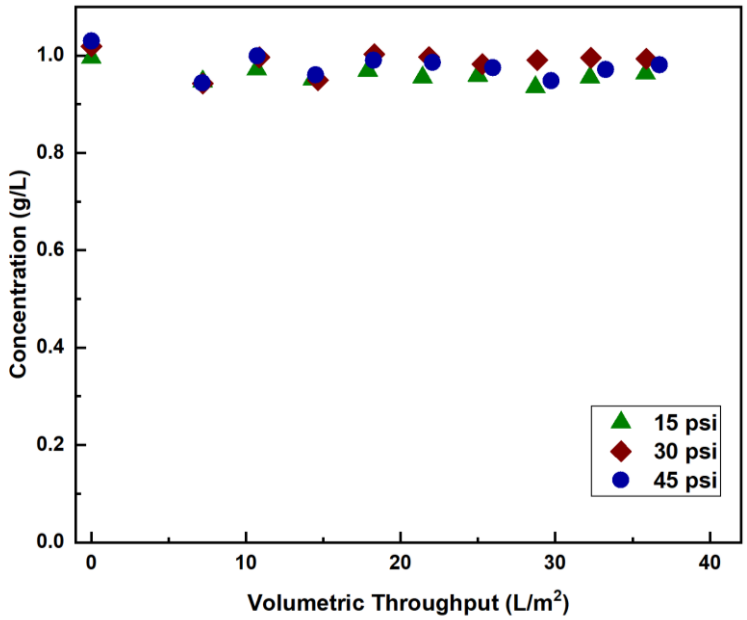

Figure 6.2 IgG concentration in filtrate as a function of protein volumetric throughput for filtration of 1 g/L IgG solutions through Viresolve® Pro membranes at constant transmembrane pressures of 15, 30, and 45 psi.

6.3.1.1 Confocal Microscopy

In order to obtain additional insights into the effects of transmembrane pressure on the fouling behavior, filtration experiments were performed using fluorescently labeled IgG over the range of transmembrane pressures examined in Figure 6.1, with the cross-sections of the fouled membranes examined by confocal microscopy. The total concentration of the protein solution was adjusted to 1 g/L, with approximately 2.5% of the labeled IgG; the flux profiles in these experiments were essentially identical to those shown in Figure 6.1. Figure 6.3 shows confocal images of the cross-section of the Viresolve® Pro membranes after filtration of 30 L/m^2 of the IgG solutions at constant

pressures of 15 psi (left) and 45 psi (right), corresponding to filtrate flux decline of ≈90% and ≈70%, respectively. In both cases, a narrow red band was observed just upstream of the filter exit with thickness <5 µm, representing the deposition of IgG within the small pores within the retentive layer of the filter. The locations of the captured IgG are very similar at 15 and 45 psi, but the band at 15 psi is brighter, consistent with the greater amount of fouling seen in Figure 6.1.

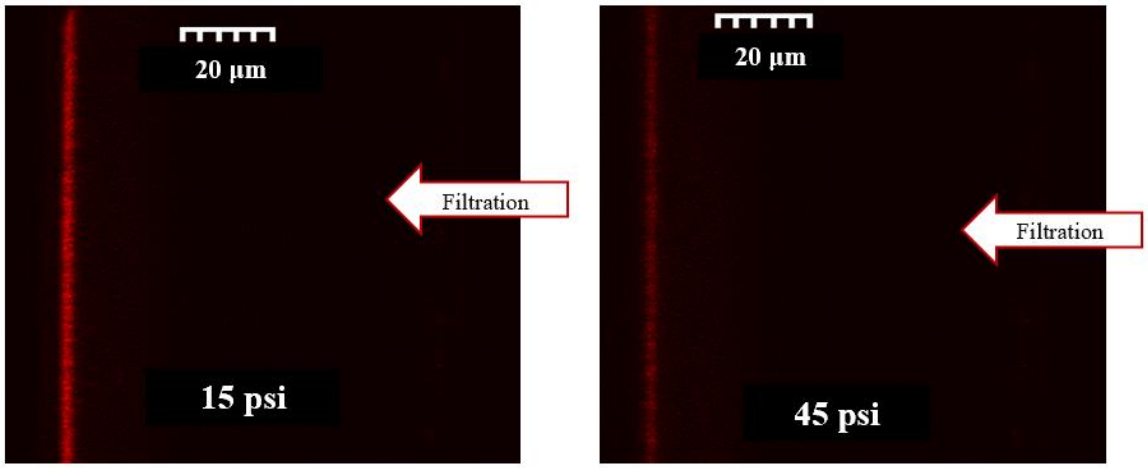

Figure 6.3 Confocal laser scanning microscopy images of the Viresolve® Pro membranes after filtration of 1 g/L solutions of fluorescently labeled IgG at a constant pressure of 15 psi (left panel) and 45 psi (right panel).

6.3.1.2 Size Exclusion Chromatography

In order to identify the origin of the fouling seen in Figures 6.1 and 6.3, the IgG solution was analyzed by size exclusion chromatography with results shown in Figure 6.4 as the solid blue curve. Major peaks were apparent at elution times of 15, 20, 24 minutes.

The peak at 24 min corresponds to the IgG monomer, while the peaks at 15 and 20 min are due to the presence of IgG dimers and multimers, respectively.

The effective size of the different IgG species was estimated based on the SEC retention time using a calibration curve constructed with narrow molecular weight dextran standards ranging from 60 to 500 kDa:

$$\log M_p = a\, V_R + b \tag{6.1}$$

where M_p is the peak average molecular weight, V_R is the retention volume, and a and b are constants fit to the data by linear regression. The molecular weight of each IgG species was evaluated directly from Eq. 6.1 using the location of the peak maximum, with the hydrodynamic radius estimated from the following empirical equation for the dextran radius [14]:

$$R_h = 3.1 \times 10^{-11}\ {M_w}^{0.47752} \tag{6.2}$$

where M_w is the molecular weight in Da and R_h is in m. Table 6.1 summarizes the results. The IgG monomer is 4.6 nm, consistent with previous estimates of the size of immunoglobulins. The size of the higher order IgG oligomer is 11.8 nm, which is larger than the 10 nm radius of the pores in the skin layer of the Viresolve® Pro membrane. Thus, the significant flux decline observed during the filtration of IgG may well be due to the capture of these high molecular weight oligomers in the small pores of the virus filter.

In order to examine this hypothesis in more detail, an IgG solution was prepared that was highly enriched in the monomer fraction of the IgG using preparative size exclusion chromatography. The solid red curve in Figure 6.4 shows the chromatogram of this “monomeric IgG”. The dimer concentration in this sample was only 1.4%, with no

detectable concentration of the higher order IgG oligomer (Table 6.2). This monomeric IgG was then filtered through Viresolve® Pro membranes at transmembrane pressures of 15 and 45 psi, with results for the normalized filtrate flux shown in Figure 6.5. In contrast to the results with the stock IgG, the filtrate flux prolife for the monomeric IgG was nearly constant and independent of the transmembrane pressure, with only around a 10% flux decline after 30 L/m^2 of filtration. These results demonstrate that the major fouling component in the IgG solution was associated with IgG oligomers that could be removed by SEC.

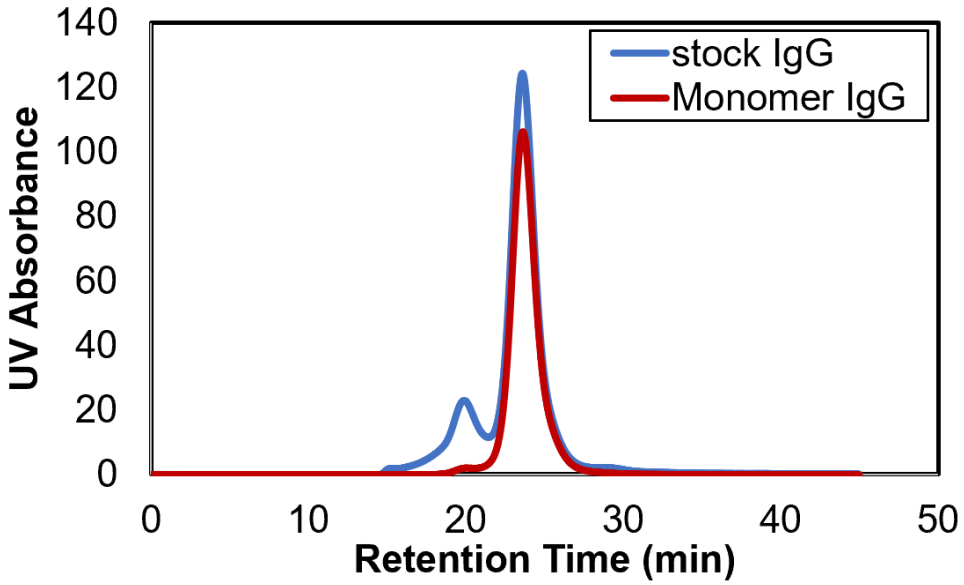

Figure 6.4 Size exclusion chromatograms for stock IgG solution (blue curve) and purified IgG monomer (red curve).

Table 6.1 Hydrodynamic radius of IgG fractions

Stock IgG	1st Peak	2nd Peak	3rd Peak
Retention Time (min)	15	20	24
Hydrodynamic Radius (nm)	11.8	6.9	4.6

Table 6.2 Concentration of IgG fractions in stock and monomer IgG solutions

	Stock IgG	Purified IgG
Monomer (%)	83	98.6
Dimer (%)	16.3	1.4
Multimer (%)	0.7	0

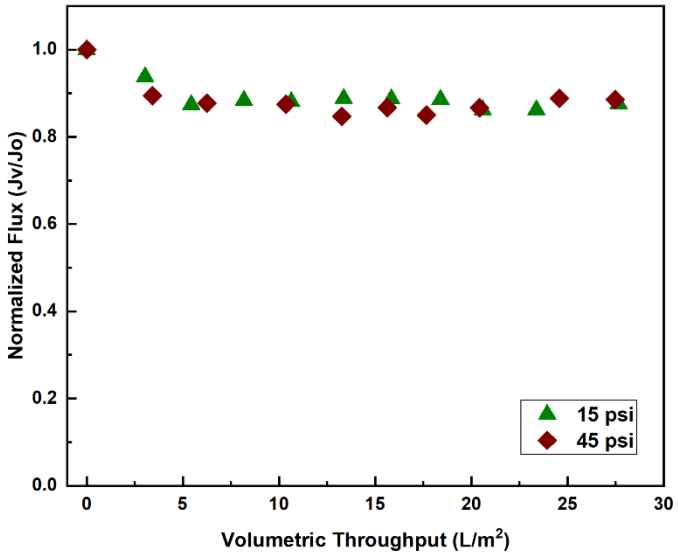

Figure 6.5 Normalized filtrate flux as a function of volumetric throughput for filtration of 1 g/L solutions of monomeric IgG through the Viresolve® Pro membranes at constant transmembrane pressures of 15 and 45 psi.

6.3.1.3 BSA Filtration

Additional filtration experiments were performed using BSA with a molecular weight of 66 kDa. Figure 6.6 shows data for the normalized filtrate flux as function of protein volumetric throughput during filtration of 4 g/L BSA solutions through the Viresolve® Pro membranes at constant transmembrane pressures of 15, 30, and 45 psi. The data at all 3 pressures collapse to a single curve, with a small initial drop in flux after which the filtrate flux remained essentially constant at a value approximately 95% of the initial flux.

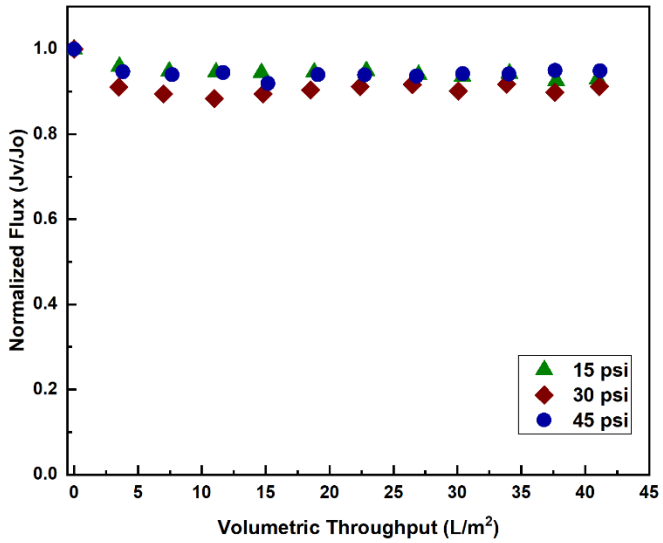

Figure 6.6 Normalized filtrate flux as a function of protein volumetric throughput for filtration of 4 g/L BSA solutions through the Viresolve® Pro membranes at constant transmembrane pressures of 15, 30, and 45 psi.

Figure 6.7 shows the SEC chromatogram obtained for 4 g/L solutions of the BSA. Three peaks were apparent at elution times of 21, 23, and 27 min with concentration of 1%, 9%, and 90%, respectively. The size corresponding to the largest BSA peak was 12 nm,

which is less than the 10 nm pore radius of the Viresolve® Pro membrane. The absence of any large molecular weight species is consistent with the very low degree of fouling seen with the BSA.

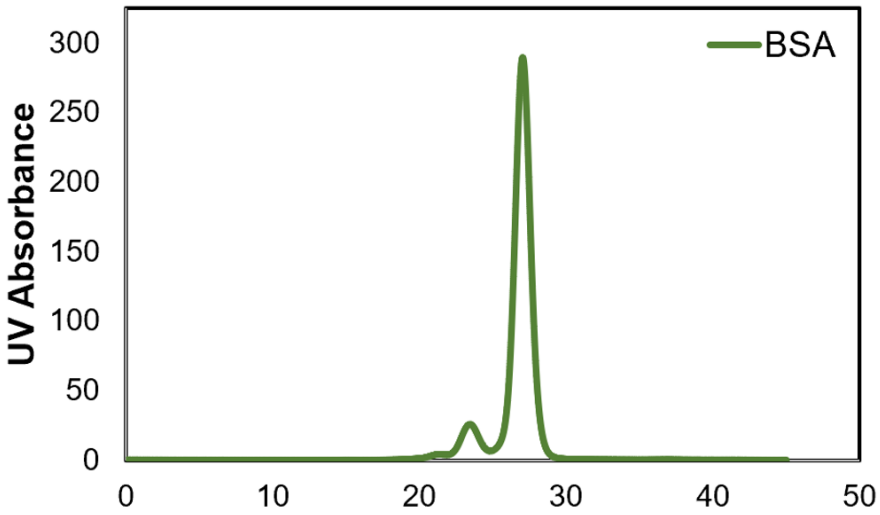

Figure 6.7 Size exclusion chromatogram for 4 g/L BSA solution. Major peaks were observed at retention times of 27, 23, and 21 min, which correspond to BSA monomer, dimer and trimer, respectively.

6.3.1.4 Nanoparticle Filtration and SEM Imaging

Additional insights into the fouling behavior of the Viresolve® Pro membrane were obtained by filtration of a suspension of 20 nm gold nanoparticles with concentration of 10^{10} particles / mL at constant transmembrane pressures of 15 and 45 psi. The normalized flux was independent of the applied transmembrane pressure, with the flux declining by around 40% after 40 L/m^2 at both 15 and 45 psi (Figure 6.8).

The membranes used in Figure 6.8 were removed from the stainless steel holder and prepared for SEM analysis as described previously. The 20 nm particles were transported all the way through the membrane and were retained in a band located immediately upstream of the filter exit (Figure 6.9). The capture profiles were similar at both 15 and 45 psi, although the band at 45 psi (right panel) does appear to be somewhat thicker (more diffuse). However, this may simply reflect the inherent variability in nanoparticle capture between membrane samples or at different locations within a single membrane.

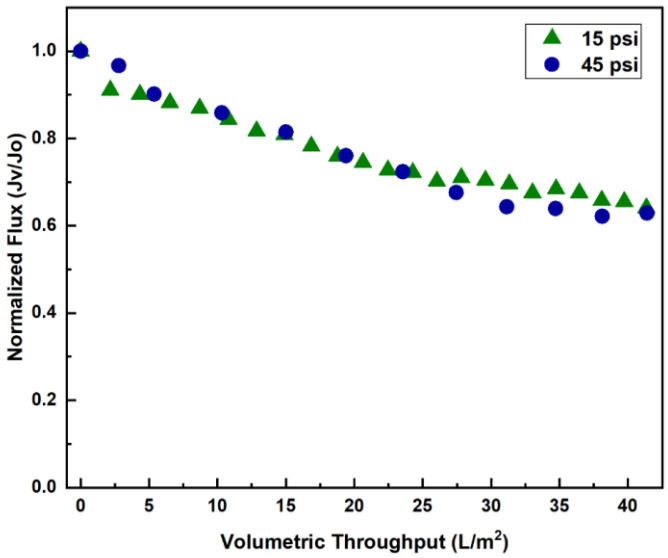

Figure 6.8 Normalized filtrate flux as a function of volumetric throughput for filtration of a suspension of 20 nm gold nanoparticles through the Viresolve® Pro membranes at constant transmembrane pressures of 15 and 45 psi.

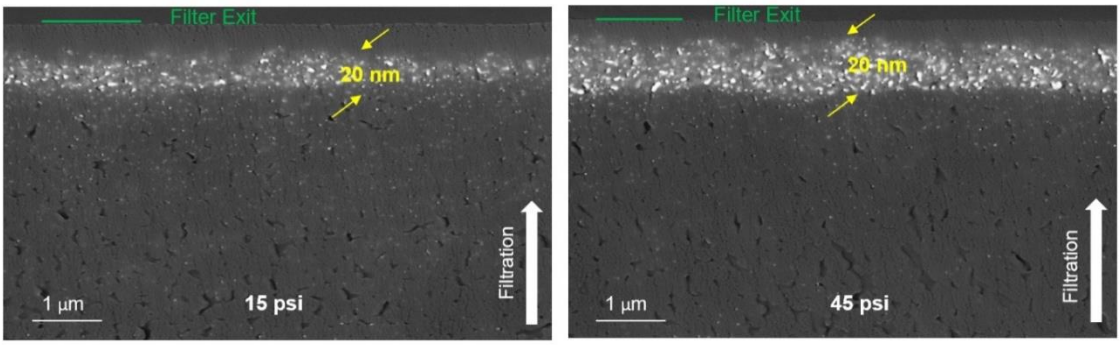

Figure 6.9 SEM images of Viresolve® Pro membranes challenged with 40 L/m^2 of a suspension containing 20 nm gold nanoparticles at constant pressures of 15 psi (left panel) and 45 psi (right panel).

6.3.2 Viresolve® NFP Membrane

6.3.2.1 IgG Filtration

Figure 6.10 shows the normalized filtrate flux versus volumetric throughput data for filtration of 1 g/L solutions of the stock IgG through Viresolve® NFP membranes at 15, 30, and 45 psi. In contrast to the results with the Viresolve® Pro, IgG fouling of the Viresolve® NFP was essentially independent of the operating pressure, with the flux declining very rapidly to less than 10% of the initial flux after filtration of only 10 L/m^2 of the IgG solution (compared to more than 40 L/m^2 for the Viresolve® Pro). The corresponding data for the protein concentration in the filtrate are shown in Figure 6.11. The IgG concentrations were essentially constant throughout the filtration (except for a small dilution effect with the early samples) with values of 0.94±0.03 g/L at all three pressures.

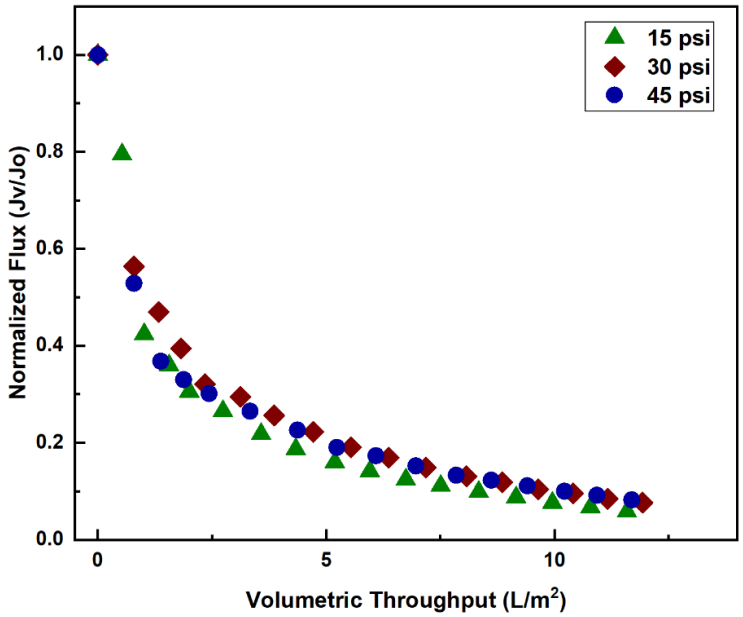

Figure 6.10 Normalized filtrate flux as a function of protein volumetric throughput for filtration of 1 g/L IgG solutions through the Viresolve® NFP membranes at constant transmembrane pressures of 15, 30, and 45 psi.

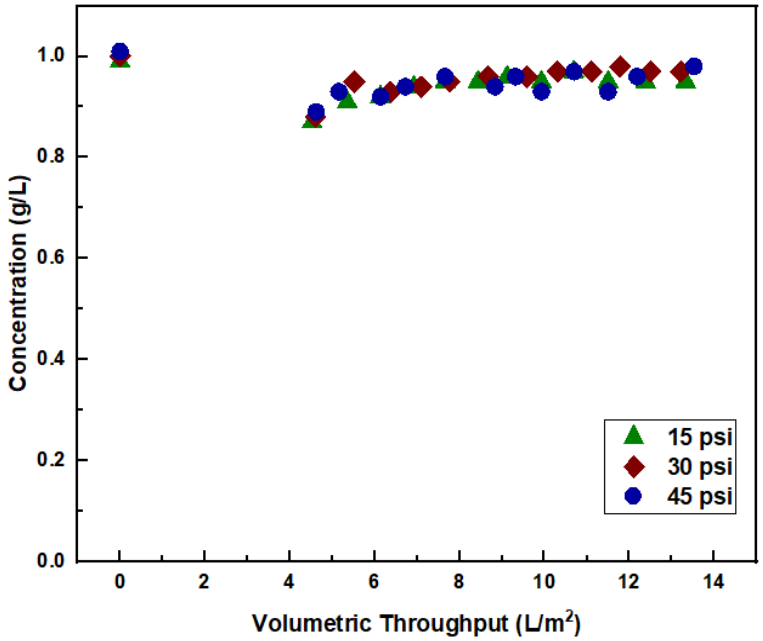

Figure 6.11 IgG concentration in filtrate as a function of protein volumetric throughput for filtration of 1 g/L IgG solutions through Viresolve® NFP membranes at constant transmembrane pressures of 15, 30, and 45 psi.

6.3.2.2 BSA Filtration

Figure 6.12 shows data for fouling of the Viresolve® NFP membranes using 4 g/L solutions of BSA. BSA fouling was independent of the transmembrane pressure, with minimal flux decline over the 20 L/m^2 protein filtration, similar to the results with BSA filtration through the Viresolve® Pro (shown in Figure 6.6).

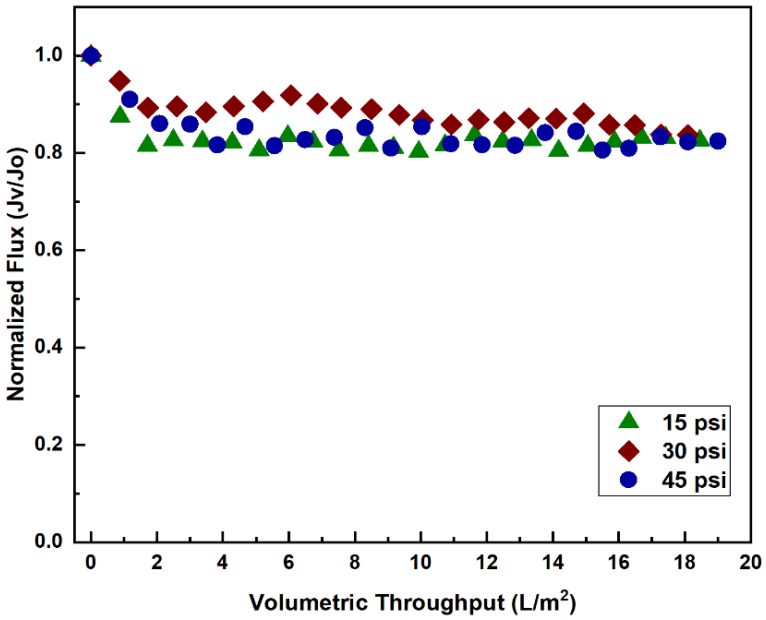

Figure 6.12 Normalized filtrate flux as a function of protein volumetric throughput for filtration of 4 g/L BSA solutions through the Viresolve® NFP membranes at constant transmembrane pressures of 15, 30 and 45 psi.

6.4 Conclusions

The experimental data presented in this Chapter provide important insights into the factors controlling IgG and BSA fouling of the Viresolve® Pro and NFP virus filters. Experiments with the Viresolve® Pro membrane showed that the flux and capacity during

IgG filtration are highly dependent on the operating pressure, with the capacity increasing from 20 L/m^2 at 15 psi to 40 L/m^2 at 45 psi. Confocal images of the Viresolve® Pro membranes challenged with fluorescently-labeled IgG showed that the IgG was retained in a very thin region upstream of the filter exit with greater fluorescent intensity detected at lower transmembrane pressure, consistent with larger degree of fouling at low pressure.

The large flux decline observed during IgG filtration was due to the capture of oligomeric IgG foulants that could be removed by size exclusion chromatography. Removal of these high molecular weight IgG aggregates gave a monomeric IgG that showed almost no fouling of the Viresolve® Pro membrane. A similar lack of fouling was seen with 4 g/L solutions of BSA (which showed no significant high MW species in SEC).

Experimental data obtained with the Viresolve® NFP membranes showed very rapid fouling with IgG, but the rate of flux decline was independent of the transmembrane pressure. The very different fouling behavior seen with the Viresolve® Pro and NFP filters is likely related to the very different internal pore structures of these two membranes as discussed previously in this thesis.

There are several possible physical mechanisms that could lead to the increased fouling at low transmembrane pressure seen with IgG in the Viresolve® Pro virus filter. Bolton et al. [15] hypothesized that this behavior was due to adsorptive fouling, with the greater rate of adsorption at low pressure arising from the greater residence time within the membrane pores due to the lower filtrate flux. Data obtained with IgG filtration through the Viresolve® 180 membrane were best fit to a model combining internal adsorptive fouling with external cake formation, although the authors provided no independent

evidence for this physical picture of protein fouling. In addition, it is surprising that adsorptive fouling would be more important with the Viresolve® Pro (which shows greater fouling at low pressure) than with the Viresolve® NFP (which shows fouling that is independent of pressure) since the Viresolve® NFP is made from a more hydrophobic polymer (PVDF versus PES).

An alternative explanation for the lower flux decline at high pressures is that the protein fouling occurs over a larger volume of the membrane under these conditions, with the more dispersed protein deposit causing a lower resistance to flow. This more diffuse deposition at high filtrate flux (i.e., high pressure) could be due to greater inertial deposition within the filter, changes in the flow distribution, etc. The effect of a more diffuse protein deposit would likely be greater in the Viresolve® Pro membrane (compared to the Viresolve® NFP) since the Viresolve® Pro has a more gradual pore size gradient (see Figure 4.1 in Chapter 4). In addition, the pores in the Viresolve® Pro membrane are more highly interconnected (see Chapter 5); thus, a protein deposit within the depth of the Viresolve® Pro would be expected to cause less disturbance to the overall flow as the fluid simply passes around that region of the membrane. Additional studies would clearly be required to substantiate this physical picture of fouling in the Viresolve® Pro versus NFP membranes.

6.5 Literature Cited

[1] T. Ireland, H. Lutz, M. Siwak, G. Bolton, Viral filtration of plasma-derived human IgG, Pharm. Technol. Eur. 18 (2006) 43–49.

[2] G. Miesegaes, S. Lute, K. Brorson, Analysis of viral clearance unit operations for monoclonal antibodies, Biotechnol. Bioeng. 106 (2010) 238–246. doi:10.1002/bit.22662.

[3] G. Sofer, J. Carter, Viral Clearance: A strategy for quality by design and the design space, in: A. Rathore, R. Mhatre (Eds.), Qual. by Des. Biopharm., John Wiley & Sons, Inc., Hoboken, NJ, USA, 2008: pp. 143–159. doi:10.1002/9780470466315.ch8.

[4] M. Krishnan, G. Kern, Virus removal by filtration: Points to consider, BioPharm Int. 19 (2006).

[5] M. Burnouf, T; Radosevich, Nanofiltration of plasma-derived biopharmaceutical products, Haemophilia. 9 (2003) 24–37.

[6] R. Van Reis, A. Zydney, Membrane separations in biotechnology, Curr. Opin. Biotechnol. 12 (2001) 208–211.

[7] Z.H. Syedain, D.M. Bohonak, A.L. Zydney, Protein fouling of virus filtration membranes: Effects of membrane orientation and operating conditions, Biotechnol. Prog. 22 (2006) 1163–1169. doi:10.1021/bp050350v.

[8] M. Bakhshayeshirad, Performance Characteristics of Virus Filtration Membranes: Protien Fouling and Virus Retention, The Pennsylvania State University, 2011.

[9] G.R. Bolton, J. Basha, D.P. LaCasse, Achieving high mass-throughput of therapeutic proteins through parvovirus retentive filters, Biotechnol. Prog. 26 (2010) 1671–1677. doi:10.1002/btpr.494.

[10] A. Brown, C. Bechtel, J. Bill, H. Liu, J. Liu, D. McDonald, S. Pai, A. Radhamohan, R. Renslow, B. Thayer, S. Yohe, C. Dowd, Increasing parvovirus filter throughput of monoclonal antibodies using ion exchange membrane adsorptive pre-filtration, Biotechnol. Bioeng. 106 (2010) 627–637. doi:10.1002/bit.22729.

[11] J.G. Barnard, D. Kahn, D. Cetlin, T.W. Randolph, J.F. Carpenter, Investigations into the fouling mechanism of parvovirus filters during filtration of freeze-thawed mAb drug substance solutions, J. Pharm. Sci. 103 (2014) 890–899. doi:10.1002/jps.23881.

[12] G.R. Bolton, S. Spector, D. Lacasse, Increasing the capacity of parvovirus-retentive membranes: performance of the Viresolve™ Prefilter, Biotechnol. Appl. Biochem. 43 (2006) 55–63. doi:10.1042/BA20050108.

[13] R. Hamamoto, H. Ito, M. Hirohara, R. Chang, T. Hongo-Hirasaki, T. Hayashi, Interactions between protein molecules and the virus removal membrane surface: Effects of immunoglobulin G adsorption and conformational changes on filter performance, Biotechnol. Prog. 34 (2018) 379–386. doi:10.1002/btpr.2586.

[14] K.A. Granath, Solution properties of branched dextrans, J. Colloid Sci. 13 (1958) 308–328. doi:10.1016/0095-8522(58)90041-2.

[15] G.R. Bolton, A.W. Boesch, M.J. Lazzara, The effects of flow rate on membrane capacity: Development and application of adsorptive membrane fouling models, J. Memb. Sci. 279 (2006) 625–634. doi: 10.1016/j.memsci.2005.12.057.

Chapter 7
Conclusion and Recommendations

7.1 Introduction

Monoclonal antibodies (mAbs) used for the treatment of cancer and immunological disorders are currently produced in mammalian cell lines that can harbor endogenous viruses. Therefore, the downstream purification process must provide high levels of viral clearance to ensure the safety of these biotherapeutics. Virus filtration membranes are now widely accepted as a critical part of the overall strategy for virus clearance in the biopharmaceutical industry. However, there is still a lack of fundamental understanding regarding the role of the membrane pore size and morphology on the performance characteristics of these virus filters.

The overall goal of this dissertation was to obtain more fundamental insights into the retention properties and the fouling behavior of virus filtration membranes and their relationship to the underlying membrane structural properties. This included the development of several new approaches for the characterization of virus capture within the depth of the virus filter. The following sections summarize the key findings from these studies and provide recommendations for future direction for research in this general area of bioprocessing and membrane technology.

7.2 Nanoparticles as Model Virus

Previous work in the Zydney lab demonstrated that fluorescently labeled bacteriophage could be used to study virus capture phenomena using confocal microscopy. However, the residual proteins and cell debris from the phage propagation could generate artifacts during both filtration and subsequent imaging. In addition, bacteriophages are only available in a relatively limited range of size. In Chapter 2 of this thesis, we demonstrated that one can use fluorescent nanoparticles as virus surrogates to study the performance characteristics of virus filtration membranes. In contrast to bacteriophage, these nanoparticles are available in different size, material, and surface properties, with a monodisperse size distribution, making them ideal for visualizing the capture behavior of virus filters with different pore structures using confocal microscopy. Confocal images obtained after filtration of 20 nm fluorescent nanoparticles through the Ultipor® DV20 filter showed a very similar capture pattern to that obtained with fluorescently labeled PP7 bacteriophage (25 nm in size), demonstrating the validity of this approach.

7.3 Membrane Pore Structure Characterization

7.3.1 Confocal Microscopy Imaging

A unique advantage of using fluorescently-labeled nanoparticles is the ability to challenge the virus filter with particles having different size, each with its own fluorescent dye so that the nanoparticles can be separately visualized by confocal microscopy. Images of the Viresolve® Pro filter obtained after filtration of mixtures of 20, 40, and 100 nm

nanospheres showed that the different size nanoparticles were captured near the exit of the filter, with the larger nanoparticles captured slightly further upstream. This profile is consistent with the graded pore size within this highly asymmetric membrane. In contrast, nanoparticles were captured within the DV20 membrane in a narrow band located just a few microns into depth of this nearly homogeneous membrane, with the 20 nm nanoparticles penetrating slightly deeper into the membrane, consistent with the presence of a slight asymmetry in the membrane pore size.

Experiments performed in which the virus filtration was disrupted part way through the experiment showed multiple capture zones for the 20 nm particles within the Ultipor® DV20 membrane, consistent with the migration of previously captured particles within the filter when the pressure is released. This type of migration was not seen with the Viresolve® Pro, which also provided highly robust virus retention even in response to a pressure disruption.

7.3.2 Electron Microscopy Imaging

Although confocal microscopy can provide significant insights into nanoparticle capture within virus filters, it is unable to resolve the location of individual nanoparticles. In Chapter 3, a new method was developed for studying virus filtration membranes using scanning electron microscopy of previously captured gold nanoparticles captured gold nanoparticles that led to measure the membrane pore size.

SEM images obtained of the cross-section of the Viresolve® Pro virus filtration membranes after filtration of a suspension of 20, 40, and 100 nm gold nanoparticles showed

that the majority of the 20 nm particles were captured within a region only 1 μm thick just upstream of the filter exit. The 40 and 100 nm particles were caught further upstream in distinct bands, with the location of these bands defining the gradient in pore size through the depth of the Viresolve® Pro membrane. Similar results were obtained with the Viresolve® NFP membrane, although the pore size gradient was much steeper and the 20 nm particles were captured within the last 500 nm of the filter. In contrast, the DV20 membrane was able to exclude nearly all of the 100 nm particles while the 20 nm particles were captured in a more diffuse band relatively close to the filter inlet.

This approach could also be used to study nanoparticle capture within hollow fiber virus filters. These filters were relatively homogeneous, although there was evidence of some nanoparticle capture throughout the entire depth of the hollow fiber membrane.

7.3.3 Internal Flow Distribution

Chapter 5 discussed a new technique developed to evaluate the pore interconnectivity of virus filtration membranes using scanning electron microscopy images of previously captured gold nanoparticles after filtration through the membrane with the exit (skin side) partially blocked by a stainless steel spacer. The capture pattern of the gold nanoparticles provides a "map" of the flow streamlines within the interior of the membrane.

SEM images obtained of the highly asymmetric Viresolve® Pro membrane showed a significant spreading of the nanoparticles over the blocked regions as one moves further into the depth of the membrane (away from the exit). The magnitude of pore interconnectivity was calculated by comparing this capture profile with the calculated flow

streamlines determined using a numerical analysis of the flow. Results for the Viresolve® Pro and Viresolve® NFP membranes gave pore interconnectivity values of K = 1 and 0.01, respectively, consistent with a much higher degree of lateral flow in the Vireslove® Pro compared to that in Viresolve® NFP membrane. Results with the Ultipor® DV20 membrane showed nanoparticle capture only on the regions of the inlet that were located directly over the open regions on the membrane exit, indicating that the flow streamlines must go almost straight through the membrane with very little pore interconnectivity.

These results provide the first quantitative measurements of the extent of pore interconnectivity within virus filtration membranes, including membranes with highly asymmetric pore structures.

7.4 Membrane Fouling

7.4.1 Effect of Protein Fouling on Nanoparticles Capture

Chapter 3 provided the first results for the effects of protein fouling on the location of nanoparticle capture within virus filtration membranes. IgG filtration in the Viresolve® Pro membrane caused a distinct shift in the capture location for the 20 nm gold nanoparticles, with the particle band moving further upstream (away from the skin layer and into the depth of the membrane) as the extent of fouling increased. This type of shift was not seen with the 40 nm and 100 nm particles, suggesting that fouling occurs primarily in the narrow pores near the exit of the filter.

In contrast to the results with the Viresolve® Pro, nanoparticle capture in the Viresolve® NFP membrane was largely unaffected by IgG fouling for any of the different size nanoparticles due to the differences observed in the underlying pore structure / properties of the membrane. These results provide unique insights into the fouling phenomena in virus filtration membranes.

7.4.2 Effect of Operating Conditions on Membrane Fouling

Chapter 6 provides a detailed study examining the effects of operating pressure and protein aggregate levels on the fouling characteristics of different virus filters. IgG filtration through the Viresolve® Pro led to a significant decline in flux, with the extent of fouling being greatest at low transmembrane pressures. In contrast, the flux profiles during BSA filtration through the Virsolve® Pro membranes collapsed to a single curve at all transmembrane pressures. The fouling characteristics of the Viresolve® NFP were independent of operating pressure when using both BSA and IgG as protein foulants.

The dramatic decline in filtrate flux during filtration of IgG was directly associated with the presence of large protein aggregates; the fouling could be nearly eliminated by removing these aggregates using size exclusion chromatography, with no significant change in the overall IgG concentration. These results provide important insights into the factors controlling the performance of these widely-used virus filtration membranes and the mechanisms governing protein fouling.

7.5 Recommendations

The results presented in this thesis provide significant insights into the key physical phenomena governing the performance characteristics, protein fouling behavior, and virus retention properties of virus filtration membranes. However, there are a number of important areas that would benefit from additional experimental and theoretical investigation.

The filtration experiments in this dissertation were focused on using a single layer membrane to facilitate imaging by confocal or scanning electron microscopy. Commercially available virus filtration modules employ multilayer membranes to provide the high degree of virus retention required in bioprocessing applications. Small-scale filters use these membranes in a simple stacked structure, while large-scale filters use these membranes as pleated sheets. Future experimental studies should examine the flow, fouling, and virus capture behavior of these multi-layer membranes, including the effects of non-uniform flow distribution in the large pleated cartridges used for large scale applications.

Confocal scanning laser microscopy using fluorescently labeled nanoparticles provides a unique opportunity to directly visualize virus capture within the membrane, including the degree of pore asymmetry. All of the experiments conducted in Chapter 2 were performed with carboxylate-modified nanospheres with a negative surface charge, It would be very interesting to extend these experiments to evaluate the retention characteristics of nanoparticles with different surface charge / chemistry (e.g.,

hydrophobicity) to determine the potential effect of these properties on the overall degree of virus removal.

It might also be possible to use the fluorescently labeled nanoparticles to directly measure the degree of virus retention by evaluating the nanoparticle concentration in both the feed and permeate solutions. Although this was relatively straightforward for the feed solution, the fluorescence intensity in the collected filtrate samples was below the level of detection of the fluorometer used in these studies. It would be very worthwhile to consider alternative approaches to measuring the concentration of the fluorescent nanoparticles, e.g., by flow cytometry which has a much lower detection limit. It might also be possible to use a higher density of fluorescent labeling or labels with a stronger intensity, e.g., quantum dots.

Direct measurements of the retention characteristics (LRV) could also be obtained using bacteriophage for which the concentration is determined by a plaque forming unit (PFU) assay. Another approach would be to use non-infectious Mock Virus Particles (MVPs) that have recently been developed. These are multiprotein structures produced recombinantly with similar physicochemical characteristics and conformation to actual mammalian viruses; the concentration of the MVP can be quantified by Immuno-QPCR analysis with very high sensitivity.

Although we were able to determine the presence of protein within the fouled virus membrane by confocal microscopy using fluorescently labeled protein, the resolution of the confocal microscope is not sufficient to detect the exact location of the trapped protein / aggregates at the scale of individual pores. It would be interesting to try to study the fouled

membrane using “Time-of-Flight Secondary Ion Mass Spectrometry” that can provide elemental analysis of a thin film with spatial resolution of less 100 nm. In this case, the nitrogen content of the protein would be distinguishable in the scanning since the polymeric membranes used for virus filtration do not contain this element.

The majority of experimental data presented in this thesis were obtained using serum Immunoglobulin G (IgG) as a model protein. It would be very appropriate to extend these studies to examine the behavior of more commercially-relevant process streams, e.g., concentrated solutions of monoclonal antibody products currently of interest in bioprocessing. These studies could also examine antibodies with different surface charge and hydrophobicity to provide a more complete understanding of how these biophysical properties control the rate and extent of fouling during virus filtration. Experiments could also be performed with antibody solutions containing different amounts of protein aggregates with different size and size distribution given the important role of protein aggregates identified in this thesis.

The numerical simulations presented in this thesis were developed using a number of significant simplifying assumptions. Future work in this area could specifically consider the effects of the membrane tortuosity, porosity, permeability, and pore size distribution as a function of position within the membrane, including the possibility that the pore interconnectivity varies with depth through the filter. These simulations may provide a better understanding of flow and nanoparticle capture in the complex pore structure of these membranes.

The primary mechanism of virus filtration is thought to be size exclusion. However, there are a number of other factors that could potentially control the performance characteristics of virus filtration processes. In particular, future studies should examine how membrane fouling and virus retention are influenced by electrostatic and / or hydrophobic interactions, both of which are known to be important in other membrane systems.

VITA

Fatemeh Fallahianbijan

EDUCATION

Doctor of Philosophy, Chemical Engineering — Aug. 2019
The Pennsylvania State University, University Park, PA — GPA: 3.92/4
Bachelor of Science (honors), Chemical Engineering — Jan. 2013
Sharif University of Technology, Tehran, Iran — GPA: 17.95/20

PROFESSIONAL EXPERIENCE

Graduate Research Assistant — Aug. 2013-Aug. 2019
Dept. of Chemical Engineering, The Pennsylvania State University

Graduate Teaching Assistant
Dept. of Chemical Engineering, The Pennsylvania State University — Aug. 2015-Dec. 2015
Dept. of Chemical Engineering, The Pennsylvania State University — Jan. 2016-May 2016

JOURNAL PUBLICATIONS

- **Fallahianbijan, F.**, Giglia, S., Carbrello, C., Zydney A. L., Journal of Membrane Science, 536:52-58 (2017)
- Nazem-Bokaee, H., **Fallahianbijan, F.**, Chen, D., O'Donnell, S. M., Carbrello, C., Giglia, S., Bell, B., Zydney, A. L., Journal of Membrane Science, 552:144-152 (2018)
- **Fallahianbijan, F.**, Giglia, S., Carbrello, C., Bell, D., Zydney A. L., Biotechnology and Bioengineering, (In Press)
- **Fallahianbijan, F.**, Giglia, S., Carbrello, C., Zydney A. L., Journal of Membrane Science, (In Preparation)
- Antensteiner, M., Khorrami, M., **Fallahianbijan, F.**, Borhan, A., Abidian, M. R., Advanced Materials, 29(39):1702576 (2017)

CONFERENCE PRESENTATIONS

- **Fallahianbijan, F.**, Giglia, S., Carbrello, C., Zydney A. L., ACS BIOT Meeting, April 2019, Orlando, FL
- **Fallahianbijan, F.**, Giglia, S., Carbrello, C., Zydney A. L., AIChE Annual Meeting, October 2018, Pittsburgh, PA
- **Fallahianbijan, F.**, Giglia, S., Carbrello, C., Zydney A. L., Gordon Research Conference, August 2018, New London, NH
- **Fallahianbijan, F.**, Giglia, S., Carbrello, C., Zydney A. L., ICOM Meeting, August 2017, San Francisco, CA
- **Fallahianbijan, F.**, Giglia, S., Carbrello, C., Zydney A. L., AIChE Annual Meeting, November 2016, San Francisco, CA
- **Fallahianbijan, F.**, Borhan, A., Abidian, M. R., MRS Fall Meeting & Exhibit, November 2015, Boston, MA

HONORS AND AWARDS

- The John D. and Jeanette McWhirter Graduate Fellowship Award — Aug. 2013
- Singapore International Pre-Graduate Award (SIPGA) from Agency for Science, Technology and Research (A*STAR) — Jun. 2011
- Recognized as an Exceptionally Talented Undergraduate Student — Feb. 2009